Oil & Natural Gas Technology

DOE Award No.: DE-FC26-04NT15507

Final Report

Combined Borehole Seismic and Electromagnetic Inversion For High-Resolution Petrophysical Assessment Of Hydrocarbon Reservoirs

Submitted by:

Carlos Torres-Verdín
The University of Texas at Austin
Phone: (512) 471-4216
e-mail: cverdin@mail.utexas.edu

and

G. Michael Hoversten, Ki Ha Lee, Gregory Newman, and Kurt Nihei
Lawrence Berkeley National Laboratory
Phone: (510) 486-5085
e-mail: gmhoversten@lbl.gov

Prepared for:
United States Department of Energy
National Energy Technology Laboratory

January 1, 2008

Office of Fossil Energy

DISCLAIMER

TABLE OF CONTENTS

List of Figures

List of Tables

CHAPTER 1

ABSTRACT

This report summarizes the work performed between January 2005 and December 2007, under DOE research contract DE-FC26-04NT15507. The project is was performed by the Center for Petroleum and Geosystems Engineering of The University of Texas at Austin and Lawrence Berkeley National Laboratory under the auspices of the National Energy Technology Office (NETL) and the Strategic Center for Natural Gas and Oil (SCNGO).

During the three-year project, we developed new methods to combine borehole sonic and electromagnetic (EM) measurements for the improved assessment of elastic and petrophysical properties of rock formations penetrated by a well. Sonic measurements consisted of full waveform acoustic amplitudes acquired with monopole and dipole sources, whereas EM measurements consisted of frequency-domain voltages acquired with multi-coil induction systems. The combination of sonic and EM measurements permitted the joint estimation of elastic and petrophysical properties in the presence of mud-filtrate invasion. It was conclusively shown that the combined interpretation of sonic and EM measurements reduced non-uniqueness in the estimation of elastic and petrophysical properties and improved the spatial resolution of the estimations compared to estimations yielded separately from the two types of measurements. Moreover, this approach enabled the assessment of dynamic petrophysical properties such as permeability, as it incorporated the physics of mud-filtrate invasion in the interpretation of the measurements.

The first part of the project considered the development of fast and reliable numerical algorithms to simulate borehole sonic waveforms in 2D, 3D, and radial 1D media. Such algorithms were subsequently used in the quantitative estimation of elastic properties jointly from borehole sonic and EM measurements.

In the second part of the project we developed a new algorithm to estimate water saturation, porosity, and dry-rock elastic moduli jointly from borehole sonic and EM measurements. This algorithm assumed radial 1D variations of fluid saturation due to mud-filtrate invasion. Subsequently, we adapted the estimation method to interpret borehole field measurements acquired in both a shaly-sand sedimentary sequence and a tight-gas sandstone formation. In the two cases, we simulated the process of mud-filtrate invasion and concomitantly

honored sonic and EM measurements. We produced reliable estimates of permeability and dry-rock moduli that were successfully validated with rock-core measurements.

Finally, we introduced a new stochastic inversion procedure to estimate elastic, electrical, and petrophysical properties of layered media jointly from waveform sonic and frequency-domain EM measurements. The procedure was based on Bayesian statistical inversion and delivered estimates of uncertainty under various forms of a-priori information about the unknown properties. Tests on realistic synthetic models confirmed the reliability of this procedure to estimate elastic and petrophysical properties jointly from sonic and EM measurements.

Several extended abstracts and conference presentations stemmed from this project, including 2 SEG extended abstracts, 1 SPE extended abstract, and 2 SPWLA extended abstracts. Some of these extended abstracts have been submitted for publication in peer-reviewed journals.

CHAPTER 2
EXECUTIVE SUMMARY

This report describes the work performed by the Center of Petroleum and Geosystems Engineering of the University of Texas at Austin (UT Austin), and Lawrence Berkeley National Laboratory (LBNL), between January 2005 and December 2007, under DOE research contract DE-FC26-04NT15507, as part of the National Energy Technology Office (NETL) and the Strategic Center for Natural Gas and Oil (SCNGO).

Interpretation of sonic and electromagnetic measurements is invariably performed separately even though the two sets of measurements usually probe the same volume of rock. The overall objective of the project was to demonstrate the compatibility of sonic and electromagnetic measurements for the joint estimation of in-situ elastic and petrophysical properties. We conclusively show that estimation of elastic and petrophysical rock properties jointly from borehole sonic and electromagnetic measurements improves the resolution of the estimated properties and reduces their non-uniqueness (uncertainty) compared to estimations performed separately from the two sets of measurements. Moreover, we show that the effective combination of the two sets of measurements permits the accurate and reliable estimation of porosity, fluid saturation, and hydraulic permeability of the probed rock formations. The recommended measurement and interpretation practice in boreholes is to include the physics of mud-filtrate invasion as the driving mechanism to assess dynamic space-time variations of fluid saturation. This approach enables the in-situ estimation of both hydraulic permeability and dry-rock elastic moduli of rock formations jointly from sonic and electromagnetic measurements.

Worked performed by UT Austin included (a) the development of numerical algorithms and computer codes to simulate time-domain full-wave sonic measurements, (b) the development of inversion algorithms to estimate elastic and petrophysical properties jointly from borehole sonic and EM measurements, and (c) the successful testing of inversion algorithms on realistic synthetic and field measurements. Work performed by LBNL focused on the development and testing of a Bayesian inversion algorithm to estimate elastic, electrical, and petrophysical properties of layered media jointly from EM and full-waveform, time-domain sonic measurements. The latter inversion algorithm was specifically designed to yield estimates of uncertainty of the unknown layer-by-layer properties. Both teams (UT Austin and LBNL) collaborated on the development, application, and validation of the inversion algorithms.

The following is a list of accomplishments stemming from this project:

(1) Developed fast and reliable algorithms for the numerical simulation of time-domain sonic waveforms in the presence of radial 1D elastic and poro-elastic media. The algorithms allow the simulation of sonic waveforms for both monopole and dipole sources.

(2) Developed a fast and reliable algorithm for the numerical simulation of time-domain sonic waveforms in the presence of 2D (radial and vertical directions) elastic transversely isotropic (TI) and poro-elastic media. The algorithm is based on a finite-different time-marching discretization method that incorporates absorbing boundary conditions. It simulates time-domain waveforms for both monopole and dipole sources.

(3) Developed a fast and reliable algorithm for the numerical simulation of time-domain sonic waveforms in the presence of 3D (Cartesian coordinates) elastic transversely isotropic (TI) media. The algorithm is based on a finite-different time-marching discretization method that incorporates absorbing boundary conditions. It simulates time-domain waveforms for both monopole and dipole sources.

(4) Developed an inversion algorithm to jointly invert sonic time-domain waveforms and frequency-domain EM measurements into radial profiles of fluid saturation. In addition, the joint inversion algorithm delivers estimates of porosity and dry-rock moduli.

(5) Adapted the above joint inversion algorithm to the estimation of permeability and dry-rock elastic moduli of rocks by incorporating the physical process of mud-filtrate invasion in the estimation method. The joint inversion method was tested on on one synthetic and two field data sets; results were successfully validated with available rock-core measurements.

(6) Developed a Bayesian stochastic inversion method to jointly invert sonic and EM measurements into layer-by-layer estimates of elastic, electrical, and petrophysical properties. The inversion algorithm is based on a Bayesian statistical approach and quantifies the uncertainty of the estimated properties. Tests on realistic synthetic models confirmed the reliability of this inversion method.

Accomplishments listed above are consistent with the conceptual and development phases outlined in the Statement of Work of the original proposal. Moreover, they complete to satisfaction the various documented tasks of the research project and successfully include all the project deliverables included in the Statement of Work.

The report details and results and discussions are included across various subsequent chapters as follows: **Chapter 3** describes the development of radial 1D algorithms for the numerical simulation of time-domain sonic waveforms in both elastic and poro-elastic media. **Chapter 4** describes the development of an algorithm to simulate time-domain sonic waveforms in 2D transversely-isotropic elastic and poro-elastic media. **Chapter 5** describes the development of an algorithm to simulate time-domain sonic waveforms in 3D transversely-isotropic elastic media, which is suitable for the simulation of sonic waveforms acquired in deviated wells with both monopole and dipole sources. **Chapter 6** describes a new inversion algorithm to jointly honor borehole sonic and EM measurements in the presence of 1D radial media. The joint inversion algorithm is successfully tested on realistic models that include presence of invasion. Inversion products are water saturation, porosity, and dry-rock elastic moduli. In **Chapter 7**, we describe the application of the joint sonic-EM inversion algorithm to the interpretation of two borehole data sets. The interpretation includes the simulation of the process of mud-filtrate invasion and permits the estimation of permeability and dry-rock elastic noduli. **Chapter 8** describes a new Bayesian stochastic inversion method to jointly honor sonic and EM measurements. This algorithm is successfully tested on realistic synthetic models and quantifies the uncertainty of inverted properties. **Chapter 9** contains the description of Experimental Methods. Finally, **Chapter 10** summarizes the conclusions and best recommended practices stemming from the research project.

CHAPTER 3

PORO-ELASTIC 1D (RADIAL) SIMULATION OF SONIC WAVEFORMS

We simulate multi-pole acoustic logging measurements using the generalized Reflection/Transmission matrices method for the case of poro-elastic 1D (radially layered) media. Validation of the code is performed by comparing simulations to analytical synthetic solutions such as Thomson-Haskell's approach. We describe simulation results for cases of Biot's two-phase media models assuming Johnson's and Biot's dynamic permeability paradigms. Simulation results consider monopole and multi-pole sources.

3.1 INTRODUCTION

Traditional full waveform sonic logging is designed for borehole models in radially layered formations. Cased borehole, mudcake or invaded zones can be modeled as a radially layered medium. Tubman et al. (1984) used the Thomson-Haskell (T-H) method to study this problem. Chen et al. (1996) proposed the generalized reflection and transmission (GR/T) coefficient method to approach the same problem for the case of monopole sonic logging in single-phase elastic media. Chi and Torres-Verdín (2004) developed the method and applied it for the case of multi-pole sonic tools; Wu and Harris (1998) applied the method for seismic wave modeling in poroelastic media. The GR/T method is more stable and efficient method than the T-H method in the synthesis of wave propagation in multilayered media. In this study, the generalized R/T coefficients method for radial layered media (1D) sonic logging is extended to poro-elastic media. In addition, we apply the method to synthesize sonic waveforms in a realistic carbonate reservoir described by Biot's two-phase model with dynamic permeability.

3.2 BIOT'S TWO-PHASE MODEL WITH TWO TYPES OF DYNAMIC PERMEABILITY

Figure 3.1 shows the model geometry of a radially layered medium. The most inner layer is liquid, which is viscoelastic water. Each outer layer is a poro-elastic medium described by Biot's theory (Biot, 1962a) with Gassmann's model. It consists of a solid phase and the liquid phase which includes water and hydrocarbon, i.e., two-phase media. The multi-pole (including monopole) sonic logging tool is located along the axis of symmetry.

The solid matrix is viscoelastic, locally homogeneous, and isotropic, fully filled with the viscoelastic liquid. Parameters describing the physical properties of the Biot medium are explained as follows: ϕ is porosity, E is tortuosity, η is viscosity, k is permeability, S_w is water saturation of pore fluid, ρ_s is density of solid matrix, ρ_f is density of pore fluid, ρ_w is density of pore water, ρ_h is density of pore hydrocarbon, ρ is density of saturated rock, ρ_c is coupling density of pore fluid and matrix solid, λ_c is Lame's constant of the fluid-saturated matrix, λ_b is Lame's constant of the drained frame, μ_b is the shear modulus of the drained frame, K_b is the bulk modulus of the drained frame, K_s is the bulk modulus of the solid matrix, K_f is the bulk modulus of the pore fluid, K_w is the bulk modulus of pore water, K_h is the bulk modulus of pore hydrocarbon, M is the modulus of fluid-saturated rock. According to Biot's theory, the governing equations of poro-elastic media are given by

$$\begin{cases} \mathbf{T} = \left(\lambda_c \nabla \cdot \mathbf{u} + \alpha M \nabla \cdot \mathbf{w}\right)\mathbf{I} + \mu_b\left[\nabla \mathbf{u} + (\nabla \mathbf{u})^T\right]; \\ P_f = -\alpha M \nabla \cdot \mathbf{u} - M \nabla \cdot \mathbf{w}, \end{cases} \tag{3.2.1}$$

where $\rho = (1-\phi)\rho_s + \phi\rho_f$, $\rho_c = E\rho_f/\phi$, $\lambda_c = \lambda_b + \alpha^2 M$, $K_b = \lambda_b + 2\mu_b/3$, $\alpha = 1 - K_b/K_s$, and $M = \left((\alpha-\phi)/K_s + \phi/K_f\right)^{-1}$, in which, Gregory(1977) gave the relation formula $\rho_f = (1-S_w)\rho_h + S_w\rho_w$ and $K_f = \left[(1-S_w)/K_h + S_w/K_w\right]^{-1}$. In equation (3.2.1), $\mathbf{u}$ is the displacement vector of a solid particle and $\mathbf{w} = \phi(\mathbf{U} - \mathbf{u})$ is the relative seepage displacement vector between fluid and solid. $\mathbf{U}$ is the displacement vector of liquid particle. $\mathbf{T}$ is the total stress tensor, P_f is the fluid pressure, and $\mathbf{I}$ is the second-order identity tensor. Generalized coordinates are chosen for $\mathbf{u}$ and $\mathbf{w}$. The solid or liquid is assumed as Kelvin-Voit media, and the basic modules can be expressed as shown below:

$$\begin{cases} \mu_b = \rho_s \phi C V_{sb}^2 \equiv \rho_s \phi\left[V_{sb}(1 - i/2Q_{sb})\right]^2 \\ \lambda_b = \rho_s \phi\left(CV_{pb}^2 - 2CV_{sb}^2\right) \equiv \rho_s \phi\left\{\left[V_{pb}(1 - i/2Q_{pb})\right]^2 - 2\left[V_{sb}(1 - i/2Q_{sb})\right]^2\right\} \\ \mu_s = \rho_s CV_{ss}^2 \equiv \rho_s\left[V_{ss}(1 - i/2Q_{ss})\right]^2 \;;\; \lambda_s = \rho_s\left(CV_{ps}^2 - 2CV_{ss}^2\right) \equiv \rho_s\left\{\left[V_{ps}(1 - i/2Q_{ps})\right]^2 - 2\left[V_{ss}(1 - i/2Q_{ss})\right]^2\right\} \\ K_x = \lambda_x + \tfrac{2}{3}\mu_x, \quad x = s, b \;;\; K_x = \rho_x CV_x^2 \equiv \rho_x\left[V_x(1 - i/2Q_x)\right]^2 \quad, x = w, h, F \end{cases}, \tag{3.2.2}$$

where V_{xy} and Q_{xy} are wave velocity and quality coefficient, respectively, *x=p, s* represent compressional wave and shear wave, respectively, *y=b, s* represents drained bone frame and solid

matrix, respectively, where V_x and Q_x are wave velocity and quality coefficient of fluid, respectively, x=w, h and F represent pore water, pore hydrocarbon and borehole fluid, respectively, ρ_F is density of borehole fluid. The motion equations for poro-elastic media in the frequency-space domain can be written as

$$\begin{cases} \mu_b \nabla^2 \mathbf{u} + [H - \mu_b] \nabla e - \alpha M \nabla \xi = -\rho \omega^2 \mathbf{u} - \rho_f \omega^2 \mathbf{w} \; ; \quad \alpha M \nabla e - M \nabla \xi + i\omega \dfrac{\eta}{k} \mathbf{w} = -\rho_f \omega^2 \mathbf{u} - \rho_c \omega^2 \mathbf{w} , \end{cases} \tag{3.2.3}$$

where, $e = \nabla \cdot \mathbf{u}$, $\xi = -\nabla \cdot \mathbf{w}$, $H = \lambda_b + 2\mu_b + \alpha^2 M$, ω is angular frequency. At higher values of frequency, when frequency is higher than Biot's critical frequency, which is defined as $\omega_c = \eta\phi / (E\rho_f k)$, the dynamic permeability should be introduced into Darcy's law. What we need to do is to replace the permeability k in equation (3.2.3) with the dynamic permeability k_D according to Biot (1956b), Auriault et al. (1985), and Hu et al. (2001), and is defined by

$$k_D = k[F_B(\omega) - i\omega / \omega_c]^{-1}, \tag{3.2.4}$$

where, $F_B(\omega) = 0.25 x J_1(x) [J_2(x)]^{-1}$, $J_n(x)$ is the n-th order Bessel function, $x = \sqrt{\beta} \sqrt{i\omega k \rho_f / (\eta\phi)}$ and $\beta = sE$, s is determined by the shape of the pore, which is 8 for a spherical pore and 16/3 for a fracture. This is called Biot's dynamic permeability. Another dynamic permeability model was put forth by Johnson et al. (1987), in which the same form of motion equation is used but the coupling between density of pore fluid and solid matrix ρ_c is zero, and in (3.2.4) $F_B(\omega)$ is replaced by $F_J(\omega)$, $F_J(\omega) = \sqrt{1 - 4iE^2 k^2 \rho_f \omega / (\Lambda^2 \phi^2 \eta)}$, Λ describes pore size, $\Lambda = \sqrt{mEk/\phi}$, and m is a constant, which is 12 for a fracture and 8 for a spherical pore.

3.3 SOLUTION FOR THE MULTI-POLE ACOUSTIC WAVEFIELD IN AND OUT OF THE BOREHOLE

There are reflected and direct wave fields at the interface of the well. In the frequency-space domain, the generalized F_n pressure measured on the axis of the well in the borehole fluid can be written as

$$F_n(\theta,z,\omega)=F_D^n(\theta,z,\omega)+\tfrac{1}{2\pi}\int_{-\infty}^{\infty}\tfrac{F(\omega)}{n!}(\tfrac{r_0}{4})^n f^{2n}A_n(k_z,\omega)e^{ik_z z}dk_z\cos n(\theta-\theta_0)\,, \tag{3.3.1}$$

where $f=ik_f^r\equiv i\sqrt{k_f^2-k_z^2}$, $k_f=\omega/CV_F$, $\boldsymbol{A}_{\mathrm{n}}$ is referred to as the generalized reflection coefficient, and the direct radiation field is given by a simple expression (omitted in this chapter).

The motion equations for Biot's media can be solved with the method advanced by Schmitt (1988). The solution of the displacement potentials in frequency-wavenumber domain in the case of cylindrical coordinates are given by

$$\begin{cases}\varphi_{ni}=\frac{1}{n!}(\frac{fr_0}{2})^n\left[B_{ni}K_n(\nu_{pi}r)+C_{ni}I_n(\nu_{pi}r)\right]\cos n(\theta-\theta_0) \quad i=1,2\\ \psi_n=\frac{1}{n!}(\frac{fr_0}{2})^n\left[D_nK_n(\nu_s r)+E_nI_n(\nu_s r)\right]\sin n(\theta-\theta_0) \;\; ; \;\; \Gamma_n=\frac{1}{n!}(\frac{fr_0}{2})^n\left[F_nK_n(\nu_s r)+G_nI_n(\nu_s r)\right]\cos n(\theta-\theta_0)\\ \varphi_{ni}'=-m_1\varphi_{ni} \;\; ; \;\; \psi_n'=-m_3\psi_n \;\; ; \;\; \Gamma_n'=-m_3\Gamma_n\end{cases}, \tag{3.3.2}$$

where $\nu_s=\sqrt{k_z^2-k_s^2}$, $k_s^r=i\nu_s$ $k_s^2=\left(\omega^2/C_s^2\right)\left(1-\gamma_f m_3\right)$, $C_s^2=\mu_b/\rho$, $m_i=h_i/g_i=\left(X_i-1\right)\left(X_i\sigma_L-\gamma_f\right)^{-1}$, $i=1,2$,

$m_3=\gamma_f/\left(\gamma_c+i\frac{\eta}{k\rho}\right)$, $\gamma_f=\rho_f/\rho$, $\gamma_c=\rho_c/\rho$. $C_P^2=H/\rho$, $\sigma_L=L/H$, $\sigma_M=M/H, L=\alpha M$, $\nu_{pi}=\sqrt{k_z^2-k_{pi}^2}$,

$k_{pi}^r=i\nu_{pi}$, $i=1,2$, It is not difficult to obtain the solution of ν_{pi} from the characteristic equations (Schmitt 1988).

To adopt the generalized reflection/transmission matrices method, the Bessel functions with image variants should be changed to Hankel functions, and the normalized Hankel function should be chosen, which is expressed by adding the upper bar, namely, $\overline{H}_n^{(1)}(xr)=H_n^{(1)}(xr)e^{-ixr}$, $\overline{H}_n^{(2)}(xr)=H_n^{(2)}(xr)e^{ixr}$. Thus, the equation for the elastic wavefield out of the borehole can be written as

$$\mathbf{S}_j^{\,T}\equiv\left[u_r\;u_\theta\;u_z\;w_r\;T_{rr}\;T_{r\theta}\;T_{rz}\;P_f\right]_j^{\,T}=\frac{F(\omega)}{n!}\left(\frac{fr_0}{2}\right)^n\mathbf{M}_j\mathbf{Y}_j^{\,T}\,, \tag{3.3.3}$$

$$\text{where}\;\mathbf{Y}_j=\left[C_{P1-}^j\;\;C_{P2-}^j\;\;C_{SH-}^j\;\;C_{SV-}^j\;\;C_{P1+}^j\;\;C_{P2+}^j\;\;C_{SH+}^j\;\;C_{SV+}^j\right], \tag{3.3.4}$$

$\mathbf{M}_j$ is an 8×8 matrix, j=2,3,4,…N, and N is the sequence number of the outermost layer

(expressions for the entries of this matrix are given in Appendix A). The acoustic field in the borehole can also be written as

$$\mathbf{S}_1^T \equiv \left[u_r\ u_\theta\ u_z\ w_r\ T_{rr}\ T_{r\theta}\ T_{rz}\ P_f\right]^T = \frac{F(\omega)}{n!}\left(\frac{fr_0}{2}\right)^n \begin{bmatrix} \mathrm{m}_{11}^1\ \mathrm{m}_{21}^1\ \mathrm{m}_{31}^1\ \mathrm{m}_{41}^1\ \mathrm{m}_{51}^1\ \mathrm{m}_{61}^1\ \mathrm{m}_{71}^1\ \mathrm{m}_{81}^1 \\ \mathrm{m}_{12}^1\ \mathrm{m}_{22}^1\ \mathrm{m}_{32}^1\ \mathrm{m}_{42}^1\ \mathrm{m}_{52}^1\ \mathrm{m}_{62}^1\ \mathrm{m}_{72}^1\ \mathrm{m}_{82}^1 \end{bmatrix}^T \begin{bmatrix} C_{f-}^1 \\ C_{f+}^1 \end{bmatrix}. \tag{3.3.5}$$

In the above equation, subscripts '+' and '-' designate the outgoing and incoming waves, respectively.

3.4 BOUNDARY-CONDITION EQUATION GROUP

On the interface of two poro-elastic media, the boundary condition can be described as the continuity of displacement $\mathbf{u}$, w_r, the stress components along the radial direction and pressure. Assume that the interface of the *j*-th layer poro-elastic medium and the (*j*+1)-th layer poroelastic media is at r_j. The boundary condition can be written as

$$\mathbf{S}_j^{\ T}\left(r_j\right) = \mathbf{S}_{j+1}^{\ T}\left(r_j\right). \tag{3.4.1}$$

The boundary condition at borehole wall, where $r = r_1$ and the pore is open, can be described as

$$\left\{\begin{array}{l} (1)\text{The radial effective displacement of fluid contines} \quad u_r^{(1)} = u_r^{(2)} + w_r^{(2)} \\ (2)\text{The radial stress } T_{rr} \text{ contines } T_{rr}^{\ (1)} = T_{rr}^{\ (2)} \quad ; \quad (3)\text{The pressure } P_f \text{ contines } -P_f^{(1)} = -P_f^{(2)} \\ (4)\text{The shear stress } T_{rz} \text{ continues} \quad 0 = T_{rz}^{(2)} \quad ; \quad (5)\text{The shear stress } T_{r\theta} \text{ continues} \quad 0 = T_{r\theta}^{(2)} \end{array}\right\}. \tag{3.4.2}$$

3.5 FORMULATION OF THE GENERALIZED REFLECTION/TRANSMISSION MATRICES METHOD FOR MULTI-POLE SOURCE SONIC LOGGING IN PORO-ELASTIC RADIALLY LAYERED MEDIA

The modified R/T matrices, $\mathbf{R}_{+-}^j, \mathbf{T}_-^j, \mathbf{T}_+^j$ and $\mathbf{R}_{-+}^j$ for poroelastic solid-poroelastic solid interfaces are given by

$$\left\{\mathbf{C}_{-}^{j}=\mathbf{R}_{+-}^{j}\mathbf{C}_{+}^{j}+\mathbf{T}_{-}^{j}\mathbf{C}_{-}^{j+1} \quad ; \quad \mathbf{C}_{+}^{j+1}=\mathbf{T}_{+}^{j}\mathbf{C}_{+}^{j}+\mathbf{R}_{-+}^{j}\mathbf{C}_{-}^{j+1}\right., \text{ for } j = 2, 3, \ldots, \text{N-1}., \tag{3.5.1}$$

where $\mathbf{C}_{\pm}^{j}=\left[C_{P1\pm}^{j}\ C_{P2\pm}^{j}\ C_{SH\pm}^{j}\ C_{SV\pm}^{j}\right]^{T}$, The modified R/T matrices are 4 x4 matrices. For the first interface (fluid-poroelastic solid), the modified R/T matrices, R_{+-}^{1} (scalar), $\mathbf{T}_{-}^{1},\mathbf{T}_{+}^{1}$ and $\mathbf{R}_{-+}^{1}$ are defined by the relation

$$\left\{C_{f-}^{1}=\mathrm{R}_{+-}^{1}C_{f+}^{1}+\mathbf{T}_{-}^{1}\mathbf{C}_{-}^{2} \ ; \ \mathbf{C}_{+}^{2}=\mathbf{T}_{+}^{1}C_{f+}^{1}+\mathbf{R}_{-+}^{1}\mathbf{C}_{-}^{2}\right., \tag{3.5.2}$$

where, R_{+-}^{1} is a scalar, and $\mathbf{T}_{-}^{1},\mathbf{T}_{+}^{1}$ and $\mathbf{R}_{-+}^{1}$ are 1 x 4, 4 x 1, and 4 x 4 matrices, respectively. From equations (3.4.1), (3.4.2), (3.5.1) and (3.5.2), the modified R/T matrices yield

$$\begin{bmatrix}\mathbf{R}_{+-}^{j} & \mathbf{T}_{-}^{j}\\ \mathbf{T}_{+}^{j} & \mathbf{R}_{-+}^{j}\end{bmatrix}=\left\{\begin{matrix}\left[M_{:,1}^{j}\ M_{:,2}^{j}\ M_{:,3}^{j}\ M_{:,4}^{j}\ -M_{:,5}^{j+1}\ -M_{:,6}^{j+1}\ -M_{:,7}^{j+1}\ -M_{:,8}^{j+1}\right]^{-1}\\ \times\left[-M_{:,5}^{j}\ -M_{:,6}^{j}\ -M_{:,7}^{j}\ -M_{:,8}^{j}\ M_{:,1}^{j+1}\ M_{:,2}^{j+1}\ M_{:,3}^{j+1}\ M_{:,4}^{j+1}\right]\end{matrix}\right\}, \tag{3.5.3}$$

where $M_{:,i}^{j}=\left[\mathrm{m}_{1i}^{j}\ \mathrm{m}_{2i}^{j}\ \mathrm{m}_{3i}^{j}\ \mathrm{m}_{4i}^{j}\ \mathrm{m}_{5i}^{j}\ \mathrm{m}_{6i}^{j}\ \mathrm{m}_{7i}^{j}\ \mathrm{m}_{8i}^{j}\right]^{T}$ are column vectors whose 8 entries are the corresponding entries of matrix $\mathbf{M}_{j}$, j=2, 3, …, N-1, i=1, 2, …, 8. Similarly, for the fluid-poroelastic solid interface, one has the equation (expressions for $\mathbf{M}_{mL}^{1}$ and $\mathbf{M}_{mR}^{1}$ in (3.5.4) are given in appendix A):

$$\begin{bmatrix}\mathrm{R}_{+-}^{1} & \mathbf{T}_{-}^{1}\\ \mathbf{T}_{+}^{1} & \mathbf{R}_{-+}^{1}\end{bmatrix}=\left(\mathbf{M}_{mL}^{1}\right)^{-1}\mathbf{M}_{mR}^{1} \ . \tag{3.5.4}$$

The generalized R/T matrices $\hat{\mathbf{R}}_{+-}^{j}$ and $\hat{\mathbf{T}}_{+}^{j}$ for poro-elastic solid-poro-elastic solid interfaces are defined by

$$\left\{\mathbf{C}_{+}^{j+1}=\hat{\mathbf{T}}_{+}^{j}\mathbf{C}_{+}^{j} \ ; \ \mathbf{C}_{-}^{j}=\hat{\mathbf{R}}_{+-}^{j}\mathbf{C}_{+}^{j}\right., \text{ for } j=2, 3, \ldots, \text{N-1}. \tag{3.5.5}$$

The generalized R/T matrices $\hat{\mathbf{R}}_{+-}^{1}$ and $\hat{\mathbf{T}}_{+}^{1}$ for fluid-poro-elastic solid interface is defined by

$$\left\{\mathbf{C}_{+}^{2}=\hat{\mathbf{T}}_{+}^{1}\mathbf{C}_{f+}^{1}\ \ ;\ \ \mathrm{C}_{f-}^{1}=\hat{\mathrm{R}}_{+-}^{1}\mathbf{C}_{f+}^{1}\right.. \tag{3.5.6}$$

By substituting equations (3.5.1) and (3.5.2) into equations (3.5.5) and (3.5.6), respectively, and by rearranging terms, one obtains the recursive relationship

$$\left\{\hat{\mathbf{T}}_{+}^{j}=\left[\mathbf{I}-\mathbf{R}_{-+}^{j}\hat{\mathbf{R}}_{+-}^{j+1}\right]^{-1}\mathbf{T}_{+}^{j}\ \ ;\ \ \hat{\mathbf{R}}_{+-}^{j}=\mathbf{R}_{+-}^{j}+\mathbf{T}_{-}^{j}\hat{\mathbf{R}}_{+-}^{j+1}\hat{\mathbf{T}}_{+}^{j}\right., \text{ for j = N-1, N-2, …, 2, 1,} \tag{3.5.7}$$

where $\mathbf{I}$ is the identity matrix, $\hat{\mathbf{R}}_{+-}^{j}$ and $\hat{\mathbf{T}}_{+}^{j}$ are 4 x 4 matrices for j >1, $\hat{\mathbf{T}}_{+}^{1}$ is a 4 x 1 matrix, and $\hat{\mathbf{R}}_{+-}^{1}=\hat{\mathrm{R}}_{+-}^{1}$ is a scalar. In the outer-most layer, N, only outward-directed waves exist and the medium extends to infinity. Therefore, the generalized reflection matrix takes on the form $\hat{\mathbf{R}}_{+-}^{\mathrm{N}}=0$. For the case of a monopole source, $n=0$, and no SH wave exists, whereupon all coefficients and equations associated with the amplitude of the SH wave disappear. In similar fashion to the above derivation, from equation (3.5.1) to (3.5.7), the matrices $\hat{\mathbf{R}}_{+-}^{j}$ and $\hat{\mathbf{T}}_{+}^{j}$ can be obtained, which are 3 x 3 matrices for j >1, $\hat{\mathbf{T}}_{+}^{1}$ is a 3 x 1 matrix, and $\hat{\mathbf{R}}_{+-}^{1}=\hat{\mathrm{R}}_{+-}^{1}$ is a scalar. Most of the formulations maintain the same form as that of multi-pole. Formulations with differences are as follows:

$$\mathbf{C}_{\pm}^{j}=\left[C_{P1\pm}^{j}\ \ C_{P2\pm}^{j}\ \ C_{SV\pm}^{j}\right]^{T}, \tag{3.5.8}$$

$$\begin{bmatrix}\mathbf{R}_{+-}^{j} & \mathbf{T}_{-}^{j}\\ \mathbf{T}_{+}^{j} & \mathbf{R}_{-+}^{j}\end{bmatrix}=\left\{\begin{matrix}\left[M_{:,1}^{j}\ \ M_{:,2}^{j}\ \ M_{:,4}^{j}\ -M_{:,5}^{j+1}\ -M_{:,6}^{j+1}\ \ -M_{:,8}^{j+1}\right]^{-1}\\ \times\left[-M_{:,5}^{j}\ \ -M_{:,6}^{j}\ \ -M_{:,8}^{j}\ M_{:,1}^{j+1}\ \ M_{:,2}^{j+1}\ \ M_{:,4}^{j+1}\right]\end{matrix}\right\}, \tag{3.5.3M}$$

where $M_{:,i}^{j}=\left[\mathrm{m}_{1i}^{j}\ \ \mathrm{m}_{2i}^{j}\ \ \mathrm{m}_{4i}^{j}\ \ \mathrm{m}_{5i}^{j}\ \ \mathrm{m}_{6i}^{j}\ \ \mathrm{m}_{8i}^{j}\right]^{T}$ are column vectors whose 6 entries are the corresponding entries of matrix $\mathbf{M}_{j}$, j=2, 3, …, N-1, i=1, 3,4,5,7, 8):

$$\begin{bmatrix}\mathrm{R}_{+-}^{1} & \mathbf{T}_{-}^{1}\\ \mathbf{T}_{+}^{1} & \mathbf{R}_{-+}^{1}\end{bmatrix}=\left(\mathbf{M}_{L}^{1}\right)^{-1}\mathbf{M}_{R}^{1}\ , \tag{3.5.4M}$$

The $\mathbf{M}_{L}^{1}$ and $\mathbf{M}_{R}^{1}$ matrices in (4.4M) are described in Appendix A. The recursive scheme used to compute generalized reflection and transmission coefficients makes this algorithm more efficient than the Thomson-Haskell method.

3.6 WAVEFORM SYNTHESIS FORMULATION

Having obtained the generalized R/T matrices, the next step is to compute the unknown coefficients C^1_{f-}, C^1_{f+} and C^j_+, C^j_-, j =2, N-1 from equations (3.5.5) and (3.5.6). For the first layer, the unknown coefficients $C^1_{f-}, C^1_{f+}, C^2_+$ and A_n are given as

$$\begin{cases} \mathrm{C}^1_{f-} = \hat{\mathrm{R}}^1_{+-}\left[(\pi/2)(i)^{n+1}(-2\varepsilon_n)\right] / \left[1-\hat{\mathrm{R}}^1_{+-}e^{ik^r_f r_1}\right]; & C^1_{f+} = (\pi/2)(i)^{n+1}(-2\varepsilon_n) + C^1_f{}^{-}e^{ik^r_f r_1}; \\ A_n = (-1)^{n+1}\, 2\pi i\varepsilon_n \hat{\mathrm{R}}^1_{+-}e^{ik^r_f r_1} / \left(1-\hat{\mathrm{R}}^1_{+-}e^{ik^r_f r_1}\right); & \mathbf{C}^2_+ = \hat{\mathbf{T}}^1_+\left[\pi(i)^{n+1}(-\varepsilon_n) + (1/2)(-i)^n A_n\right] \end{cases}, \tag{3.6.1}$$

and $C^j_\pm$, j =2, N-1 are given through a recursive scheme of formulation (3.5.5):

$$\begin{cases} \mathbf{C}^{j+1}_+ = \hat{\mathbf{T}}^j_+ \mathbf{C}^j_+ = \prod_{jn=j}^{2} \hat{\mathbf{T}}^{jn}_+ \mathbf{C}^2_+ \; ; \quad \mathbf{C}^j_- = \hat{\mathbf{R}}^j_{+-}\mathbf{C}^j_+ = \hat{\mathbf{R}}^j_{+-} \prod_{jn=j-1}^{2} \hat{\mathbf{T}}^{jn}_+ \mathbf{C}^2_+ , \quad j = 2, \mathrm{N}\text{-}1 \end{cases}. \tag{3.6.2}$$

By taking A_n into formulation (3.3.1), the synthetic sonic logging data in frequency–space domain can be expressed as

$$F_n(\theta, z, \omega) = F^n_D(\theta, z, \omega) + \tfrac{1}{2\pi}\int_{-\infty}^{\infty} \tfrac{F(\omega)}{n!}\left(\tfrac{r_0}{4}\right)^n \left(k^r_f\right)^{2n}\left(-2\pi i\varepsilon_n\right) / \left[1 - 1/(\hat{\mathrm{R}}^1_{+-}e^{ik^r_f r_1})\right] e^{ik_z z} dk_z \cos n(\theta - \theta_0), \tag{3.6.3}$$

The elastic wave fields in and out of the borehole can be calculated from formulations (3.3.3) and (3.3.5), namely,

$$\begin{cases} \mathbf{S}_1{}^T \equiv \left[u_r\ u_\theta\ u_z\ w_r\ T_{rr}\ T_{r\theta}\ T_{rz}\ P_f\right]^T_1 = \dfrac{F(\omega)}{n!}\left(\dfrac{fr_0}{2}\right)^n \mathbf{M}_1 \left[\mathbf{C}^1_{f-} \quad \mathbf{C}^1_{f+}\right]^T \\ \mathbf{S}_j{}^T \equiv \left[u_r\ u_\theta\ u_z\ w_r\ T_{rr}\ T_{r\theta}\ T_{rz}\ P_f\right]^T_j = \dfrac{F(\omega)}{n!}\left(\dfrac{fr_0}{2}\right)^n \mathbf{M}_j \left[\prod_{jn=j}^{2} \hat{\mathbf{T}}^{jn}_+ \mathbf{C}^2_+ \quad \hat{\mathbf{R}}^j_{+-} \prod_{jn=j-1}^{2} \hat{\mathbf{T}}^{jn}_+ \mathbf{C}^2_+\right]^T \end{cases}. \tag{3.6.4}$$

Note that u_θ and $T_{r\theta}$ do not appear in formulation (3.6.4) for the case of a monopole source. Elastic wavefields in and out of the borehole in time–space domain are calculated with the 2D FFT method. The sonic logging tool is assumed consisting of one source and 33 traces of receivers with a uniform offset of 0.1524 meters, which can be defined as monopole, dipole,

quadrupole, etc. The pulse for the acoustic source is assumed a cosine-envelope wavelet, with its frequency spectrum given by

$$F(\omega) = 0.25t_c \left\{ \begin{bmatrix} \mathrm{F}\sin(0.5t_c\omega + 0.5t_c\omega_0) + \\ \mathrm{F}\sin(0.5t_c\omega - 0.5t_c\omega_0) \end{bmatrix} + 0.5 \begin{bmatrix} \mathrm{F}\sin(0.5t_c\omega + 0.5t_c\omega_0 + \pi) + \mathrm{F}\sin(0.5t_c\omega - 0.5t_c\omega_0 - \pi) + \\ \mathrm{F}\sin(0.5t_c\omega + 0.5t_c\omega_0 - \pi) + \mathrm{F}\sin(0.5t_c\omega - 0.5t_c\omega_0 + \pi) \end{bmatrix} \right\} e^{i0.5t_c\omega}, \quad (3.6.5)$$

where ω_0 is the central angular frequency of the source and t_c is the length of the cosine-envelope wavelet, $\mathrm{F}\sin(x)$ is a function, $\mathrm{F}\sin(x) = \sin(x)/x$.

3.7 NUMERICAL RESULTS OF WAVEFORM SYNTHESIS

Thomson-Haskell and the generalized R/T matrices methods are employed to calculate waveforms for sonic well logging. The radius of the borehole is assumed to be 0.1 meter. The fluid in the borehole is assumed to be water. All quality coefficients are assumed infinity. Numerical results for monopole, dipole and quadrupole sonic logging are considered in the simulations.

For the case of a borehole penetrating a homogeneous sandstone formation, parameters associated with the sandstone and borehole fluid are listed in Table 3.1.1, with no dynamic permeability model considered. We assume that the central frequency of the monopole, dipole and quadrupole sources is 6 kHz. Figures 3.2, 3.3, and 3.4 show the simulated results for monopole, dipole, and quadrupole sources, respectively. There are two plots in each figure, the upper one is for a receiver located at the offset z =3.048 meters, and the bottom plot is for an array of receivers. The array receivers' offsets is from z =0.3048 meters to z=5.1816 meters for monopole, and from z =2.7432 meters to z=7.62 meters for dipole and quadrupole sources, respectively. Waveforms calculated using the T-H method are marked by (T-H) and the ones calculated with the GR/T matrices method are marked by G R/T. From the comparisons, it is found that waveforms calculated using the two different methods perfectly overlay each other. To further verify the code, a 1D radial layer medium is constructed as described in Table 3.1.2, where the borehole penetrates sandstone and shale formations. Figures 3.5, 3.6, and 3.7 show the simulated results for monopole, dipole and quadrupole sources, respectively. Good agreements between the results from the T-H and from the GR/T are also shown in the figures.

For a typical 1D radial layered medium we consider the invaded zone assuming a

stepwise invasion-zone model. The configuration of the medium is described in Table 3.1.3. In this zone, medium parameters shown in Table 3.1.1 are changed linearly from shale to sandstone. In the calculation, we assume that the number of sub layers is 10. Curves for two offsets of receivers are shown in Figures 3.8, 3.9, and 3.10 for monopole, dipole and quadrupole sources, respectively. In each figure, the black solid line identifies the result with no invasion zone when the formation is sandstone; the red dashed line identifies the result with a 8 cm-thick of invasion zone, the green dashed-dotted line identifies the result with a 16 cm-thick invasion zone, and the blue dotted line identifies the result for a 22 cm-thick invasion zone. From the comparison among the different curves, it is found that the delay of arrival time due to the presence by the invasion zone.

For the case of homogenous two-phase media, we consider two types of dynamic permeability models, which are Biot's and Johnson's models. As an example, we synthesized waveforms due to a dipole source with a central frequency of 10 kHz using the generalized R/T matrices method. The formation consists of sandstone as described in Table 3.1.1 with porosity equal to 30% and permeability equal to 1000mD. Figure 3.11 shows simulated waveforms for an offset of z=4.2672 meters. There are three plots in Figure 3.11, in which the black solid line identifies the Biot-Gassmann model (marked as "No DK"), the red dashed line identifies Johnson's dynamic permeability model (marked as "J DK"), the green dashed-dotted line identifies Johnson's dynamic permeability model with $\rho_c \neq 0$ (marked as "J DK with ρ_c"), the blue dotted line identifies Biot's dynamic permeability model (marked as "B DK"). From the upper plot, we find that the result from the "J DK" almost overlaps with the result from "No DK". From the center plot, we find that the amplitude of the result from the "J DK with ρ_c" is larger than that of "No DK". From the bottom plot, the amplitude of the result from the "J DK with ρ_c" almost overlaps with that of "B DK". Results indicate that the two different dynamic permeability models are almost equivalent as the $\rho_c \neq 0$ in Johnson's dynamic permeability model, which should be understood as an additional modification besides the coupling quality between solid and liquid in two phase media.

For case of homogenous two-phase media, we consider the effect of water saturation as pore fluid. As an example, we synthesized waveform due to a dipole source with a central frequency of 10 kHz using the generalized R/T matrices method. The formation is the sandstone

model described in Table 3.1.1, with water saturation and parameters of pore fluid for gas and oil. Figure 3.12 shows the simulations results for an offset of z=4.2672 meters. There are two plots in Figure 3.12, in which the black solid line identifies the case for $S_w = 1$, the red dashed line identifies the case for $S_w = 0.5$ with the remaining pore fluid being oil, the green dashed-dotted line identifies the case for $S_w = 0.5$ with the remaining pore fluid being gas. From the upper plot, we observe that there exist two waves in each waveform for the case of half water saturation with oil and 100% water saturation; the difference is very small. From the bottom plot, we observe that there exists only one wave in the waveform for the case of half water saturation with gas. Consequently, it is easier to distinguish gas from water than oil from water in the waveforms.

3.8 CONCLUSIONS

We developed an algorithm for the synthesis of multi-pole sonic logging measurements in radially layered poro-elastic media based on the method of generalized reflection and transmission coefficients. An exact frequency-wavenumber domain solution of receiver responses associated with a multi-pole source in a fluid-filled borehole was formulated using the generalized reflection coefficient method. Validation of the algorithm was performed by comparing simulation results against those obtained with the Thomson-Haskell method for the cases of formation models consisting of a simple borehole and a borehole with two layers assuming monopole, dipole or quadrupole sonic logging tools.

The simulation algorithm was applied to study stepwise invasion-zone models. It was found that the delay of the arrival time of the mode wave was due to the presence of the invaded zone. For the case of homogenous two-phase media, we discussed two types of dynamic permeability models, namely Biot's and Johnson's models. It was shown that the two different dynamic permeability models are almost equivalent as the $\rho_c \neq 0$ in Johnson's dynamic permeability model, which should be understood as an additional modification besides the coupling quality of solid and liquid in two-phase media.

Table 3.1.1. Parameters for the poro-elastic medium (sandstone and shale) and borehole fluid.

	Porosity ϕ (%)	Permeability k (mD)		Viscosity η (kg s^{-1}m^{-1})	Tortuosity E	
Sandstone	10	10		0.001	1	
Shale	20	100		0.001	1	
	V_{ps}	V_{ss}		V_{pb}	V_{sb}	
Sandstone	5000m/s	3500m/s		3886m/s	2045m/s	
Shale	2128m/s	2000m/s		1350m/s	1228m/s	
	m	V_F		ρ_S	ρ_F	
Sandstone	12	1500m/s		2445kg/m^3	1000 kg/m^3	
Shale	12	1500m/s		2200 kg/m^3	1000 kg/m^3	
	V_w	V_h in Gas	V_h in Oil	ρ_w	ρ_h of Gas	ρ_h of Oil
Sandstone	1500m/s	449.4m/s	1155m/s	1000kg/m^3	103 kg/m^3	750 kg/m^3
Shale	1500m/s	449.4m/s	1155m/s	1000 kg/m^3	103 kg/m^3	750 kg/m^3

Table 3.1.2. Description of the configuration of the 1D layers.

Layer	Inner radius (m)	Type of media
1	0	Water
2	0.1	sandstone
3	0.5	shale

Table 3.1.3. Description of the configuration of the invaded zone

Layer	Inner radius (m)	Type of media	number of sub layers
1	0	water	0
2	0.1	shale	0
3	From 0.1 to 0.08 or 0.16 or 0.22	Invaded zone from shale to sandstone	10
4	0.08 or 0.16 or 0.22	sandstone	0

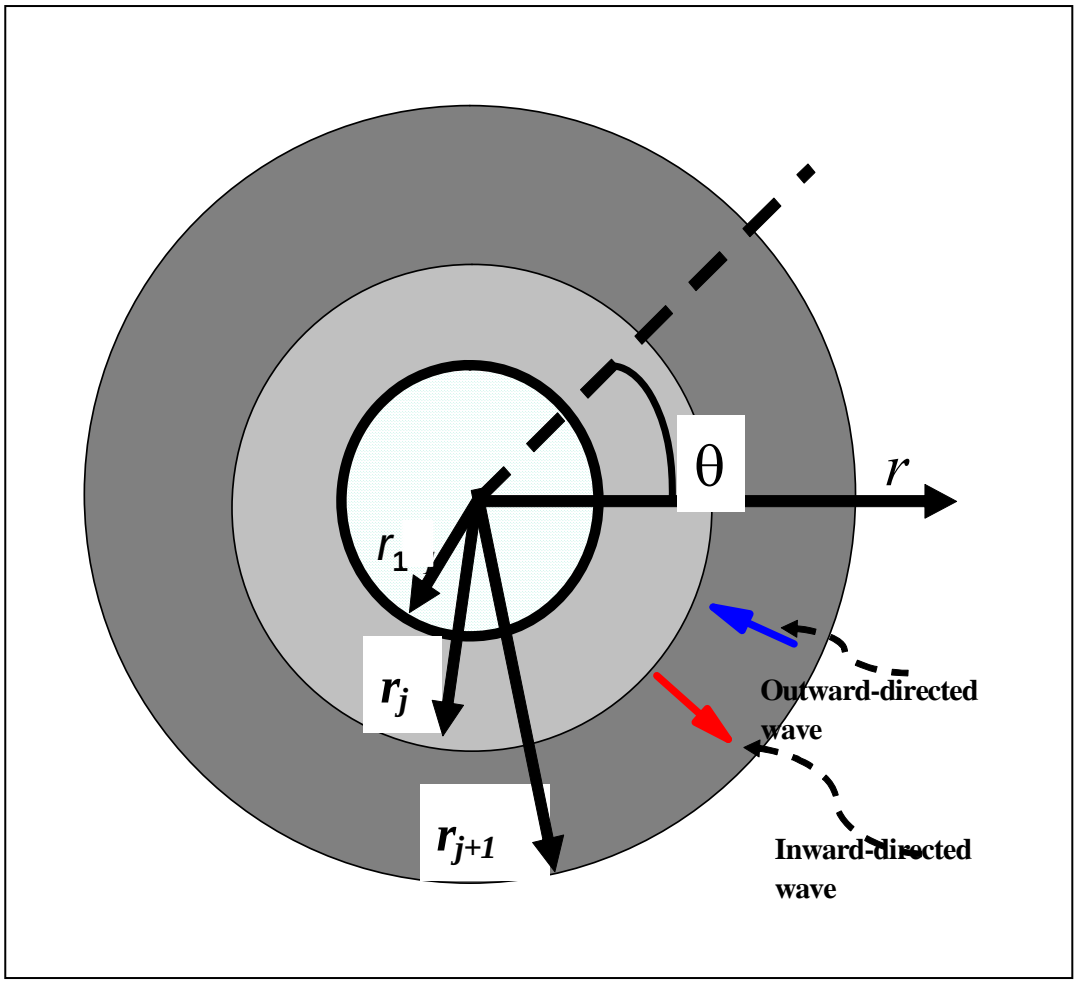

Figure 3.1. Schematic of a borehole in a radially layered formation model, with inward-directed and outward-directed waves supported within each layer except the outer-most layer, which only supports outward-directed waves.

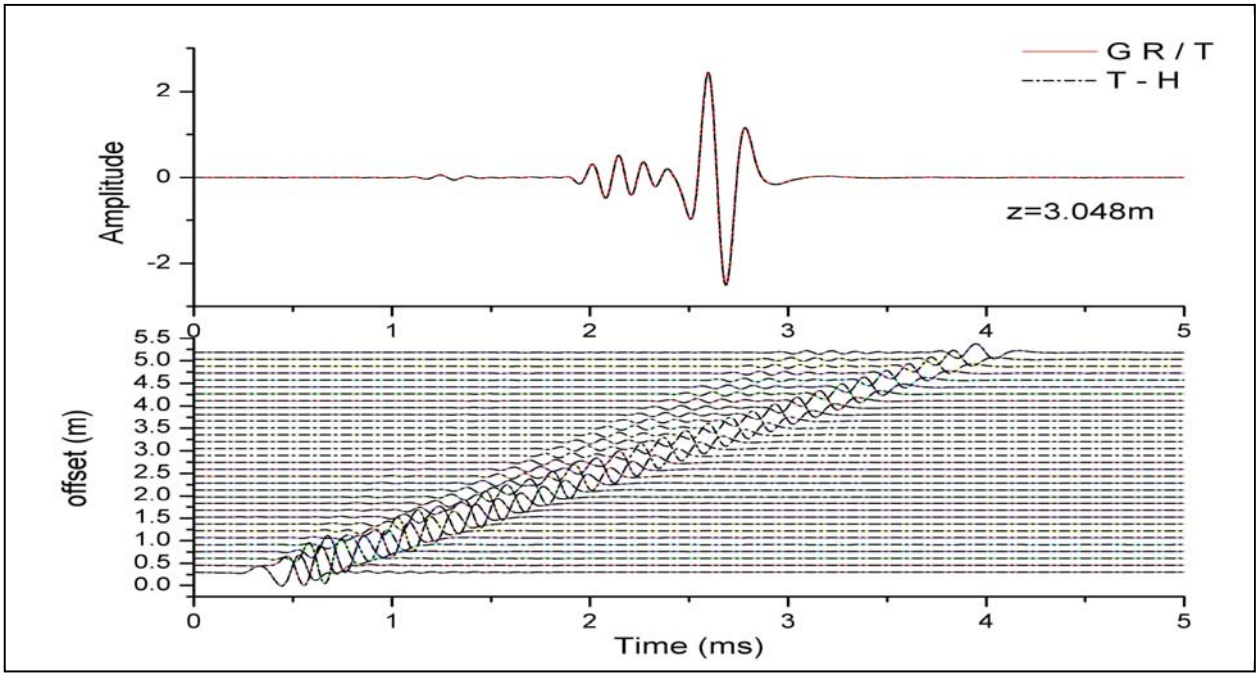

Figure 3.2. Monopole sonic logging waveforms computed with the GR/T method (solid color line) and waveforms computed with the T-H method (dashed dotted line). Formation parameters of the sandstone formation are described in Table 3.1.1.

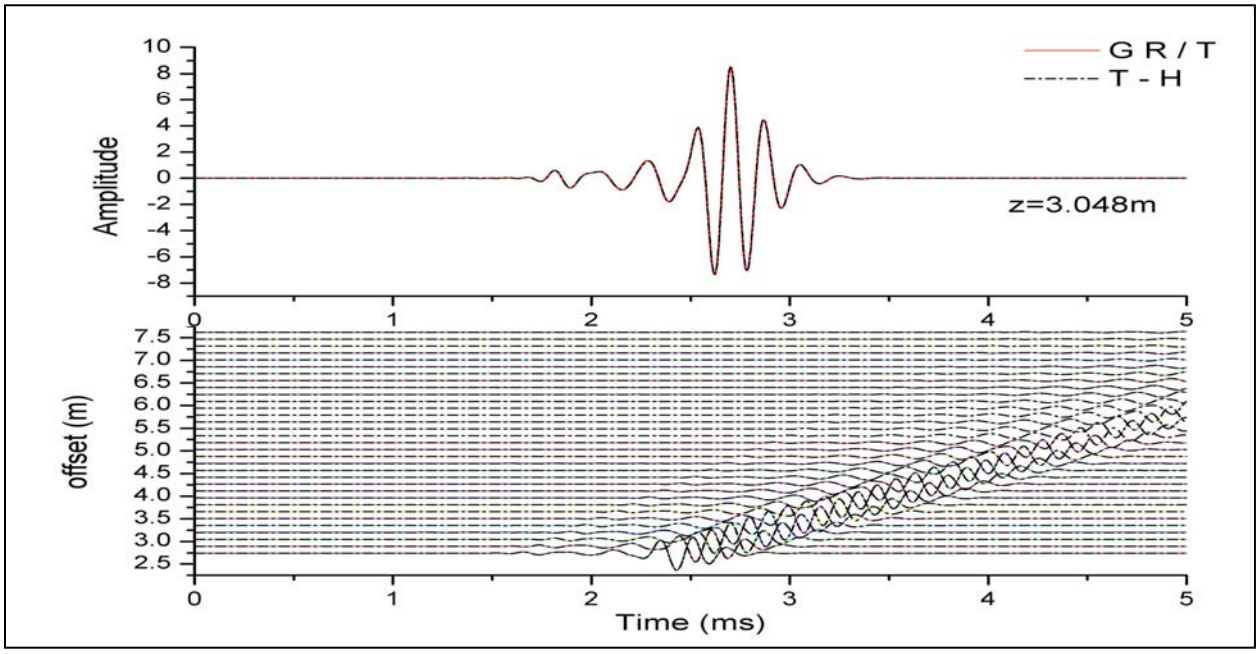

Figure 3.3. Dipole sonic logging waveforms computed with the GR/T method (solid color line) and waveforms computed with the T-H method (dashed dotted line). Parameters of the sandstone formation are described in Table 3.1.1.

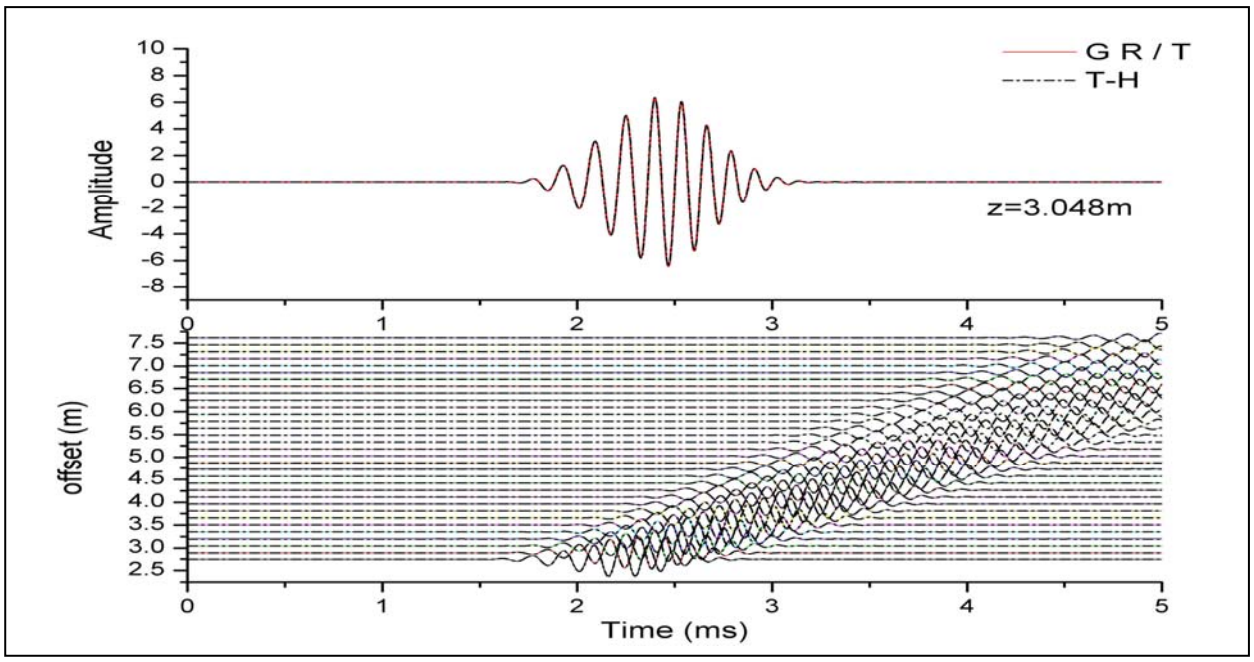

Figure 3.4. Quadrupole sonic logging waveforms computed with the GR/T method (solid color line) and waveforms computed with the T-H method (dashed dotted line). Parameters of the sandstone formation are described in Table 3.1.1. The source is a Quadrupole tool with source-receiver spacing from 2.7432 meters to 7.62 meters.

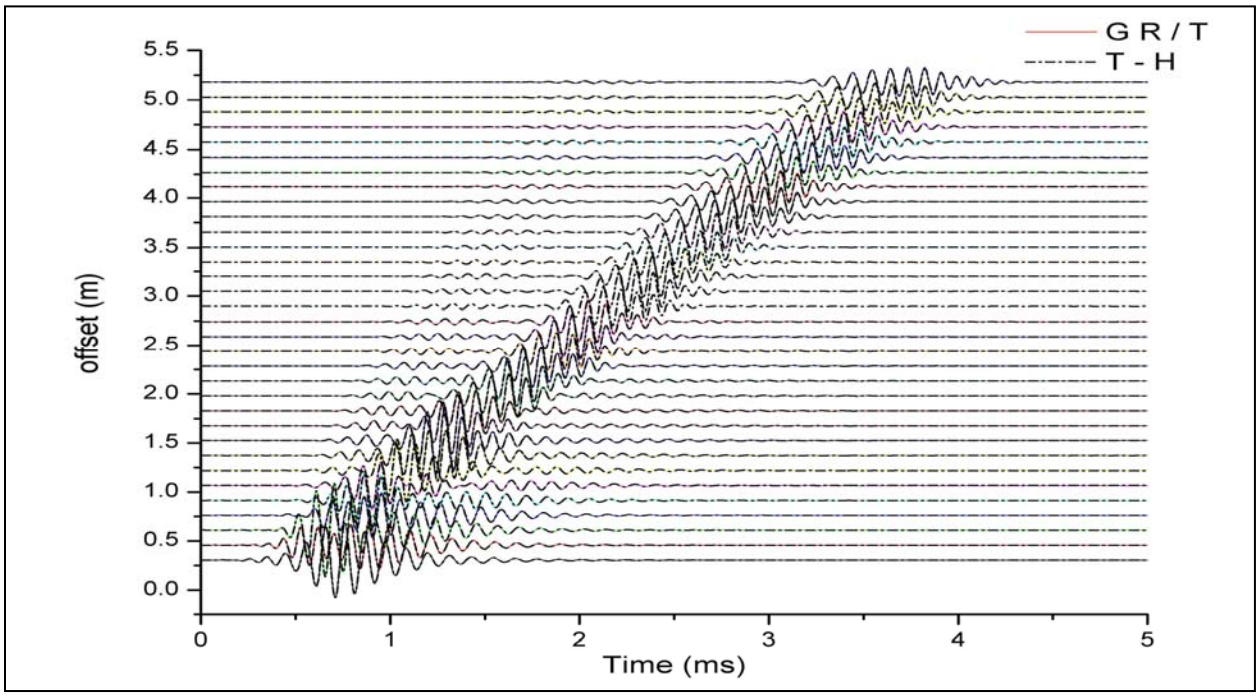

Figure 3.5. Monopole sonic logging waveforms computed with the Generalized R/T method (solid color line) and waveforms computed with the T-H method (dashed dotted line). Parameters and configurations of the formation are described in Table 3.1.2.

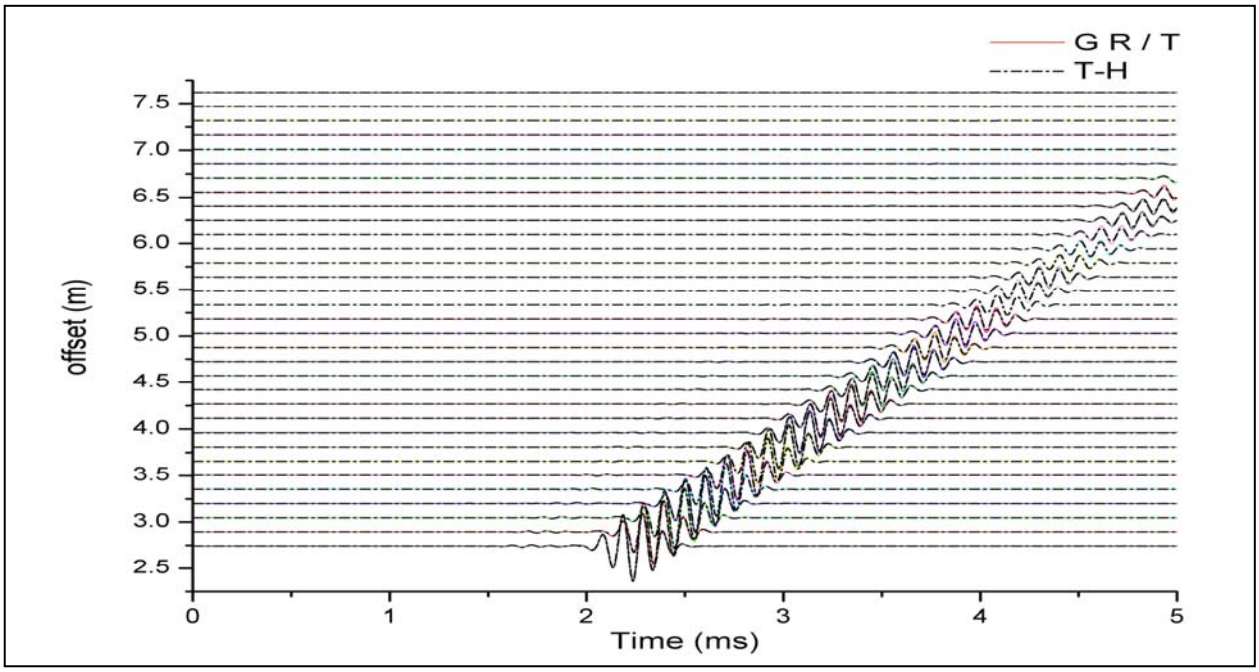

Figure 3.6. Dipole sonic logging waveforms computed with the Generalized R/T method (solid color line) and waveforms computed with the T-H method (dashed dotted line). Parameters and configuration of the formation are described in Table 3.1.2.

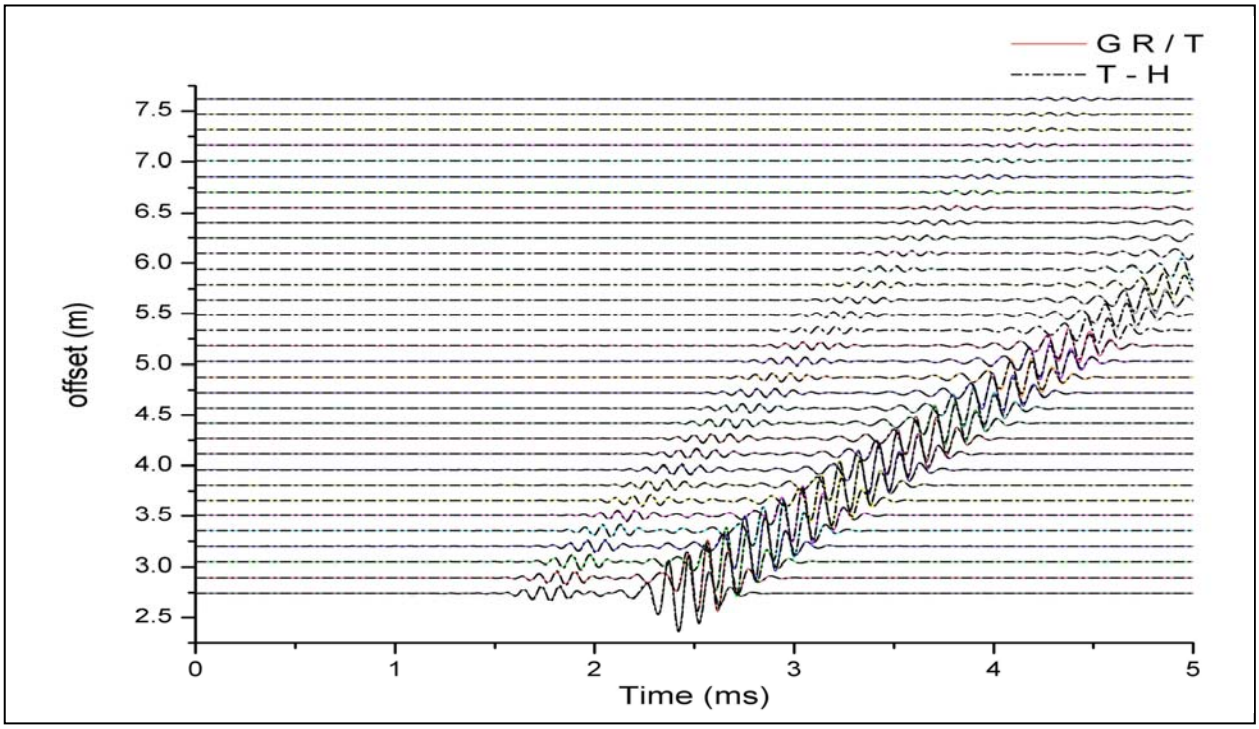

Figure 3.7. Quadrupole sonic logging waveforms computed with the Generalized R/T method (solid color line) and waveforms computed with the T-H method (dashed dotted line). Parameters and configuration of the formation are described in Table 3.1.2.

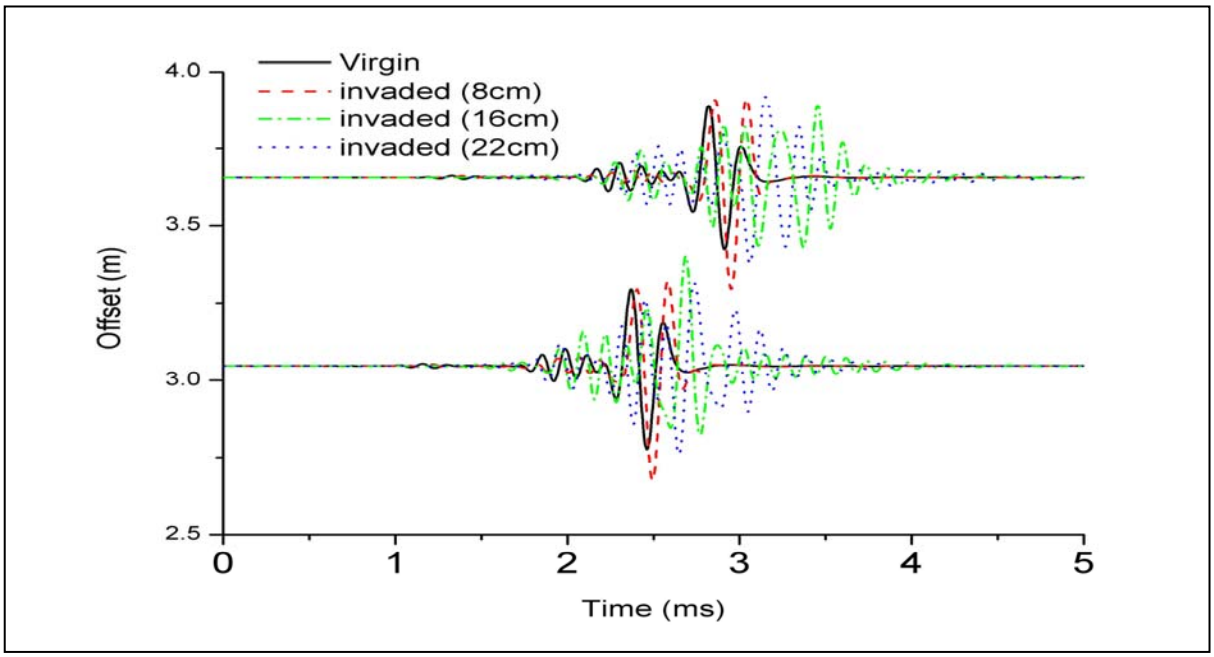

Figure 3.8. Monopole waveforms computed with the generalized R/T method assuming the borehole model described in Table 3.1.3. The source pulse is a cosine-envelope wavelet. The central frequency of the monopole source is 6kHz, and the half bandwidth is 4kHz.

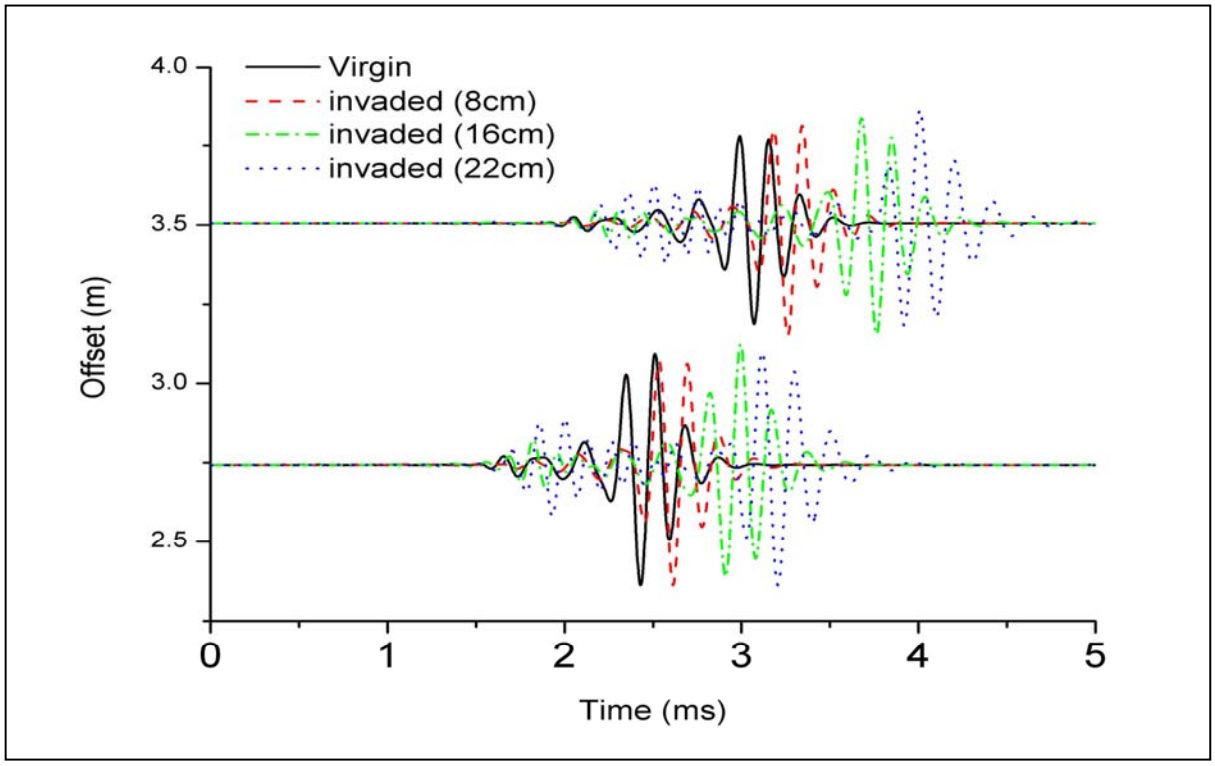

Figure 3.9. Dipole waveforms computed with the generalized R/T method assuming the borehole model described in Table 3.1.3. The source pulse is a cosine-envelope wavelet. The central frequency of the dipole source is 6kHz, and the half bandwidth is 4kHz.

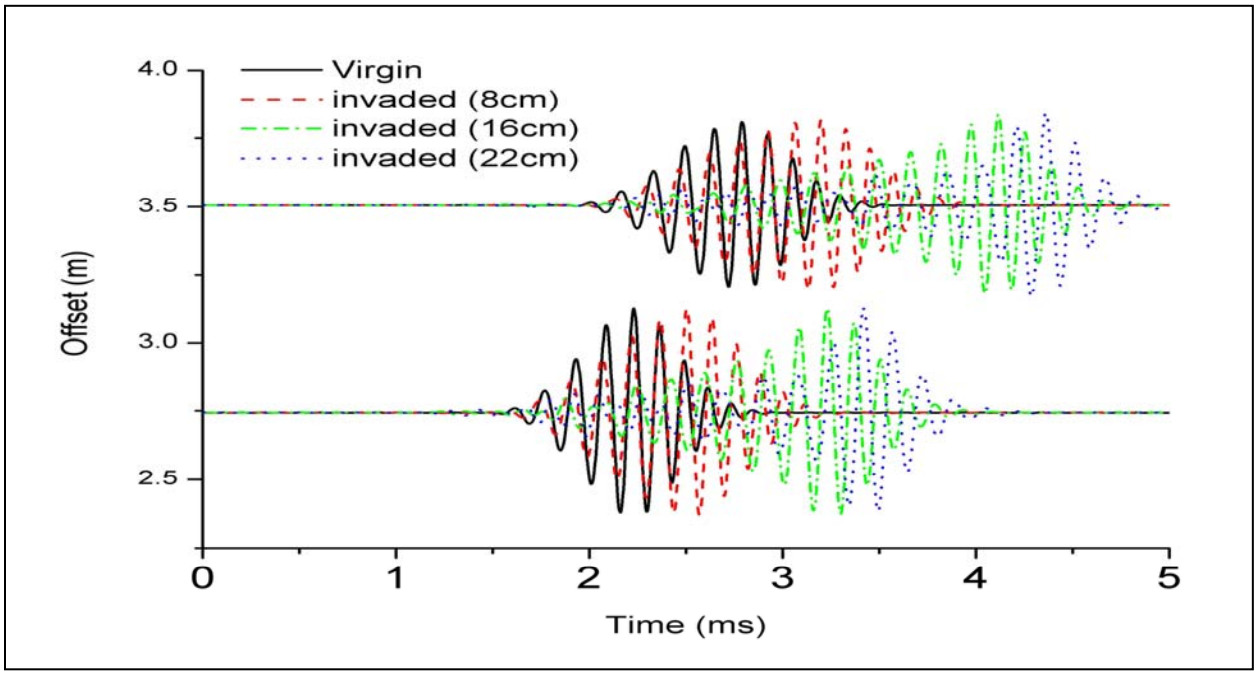

Figure 3.10. Quadrupole waveforms computed with the Generalized R/T method assuming the borehole model described in Table 3.1.3. The type of source pulse is a cosine-envelope wavelet. The central frequency of the quadrupole source is 6kHz, and the half bandwidth is 4kHz.

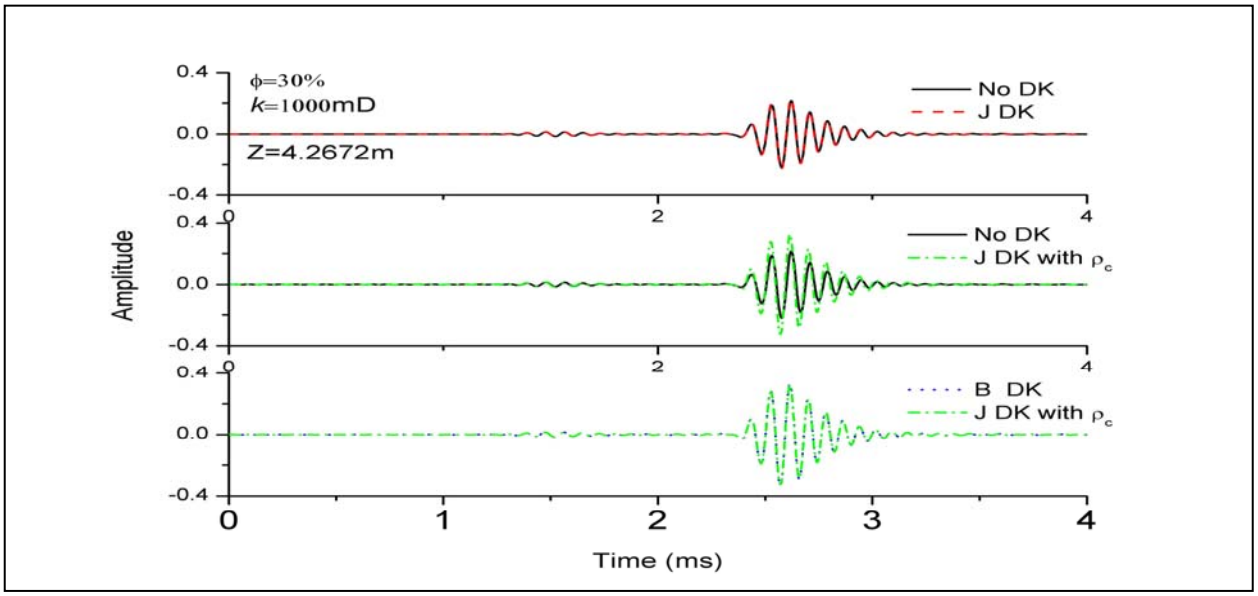

Figure 3.11. Dipole waveforms computed with the generalized R/T method assuming the borehole model described in Table 3.1.1. The source pulse is a cosine-envelope wavelet. The central frequency of the dipole source is 10 kHz, and the half bandwidth is 4 kHz. Simulations compare two types of dynamic permeability. DK stands for dynamic permeability, J stands for Johnson's model, and B stands for Biot's model.

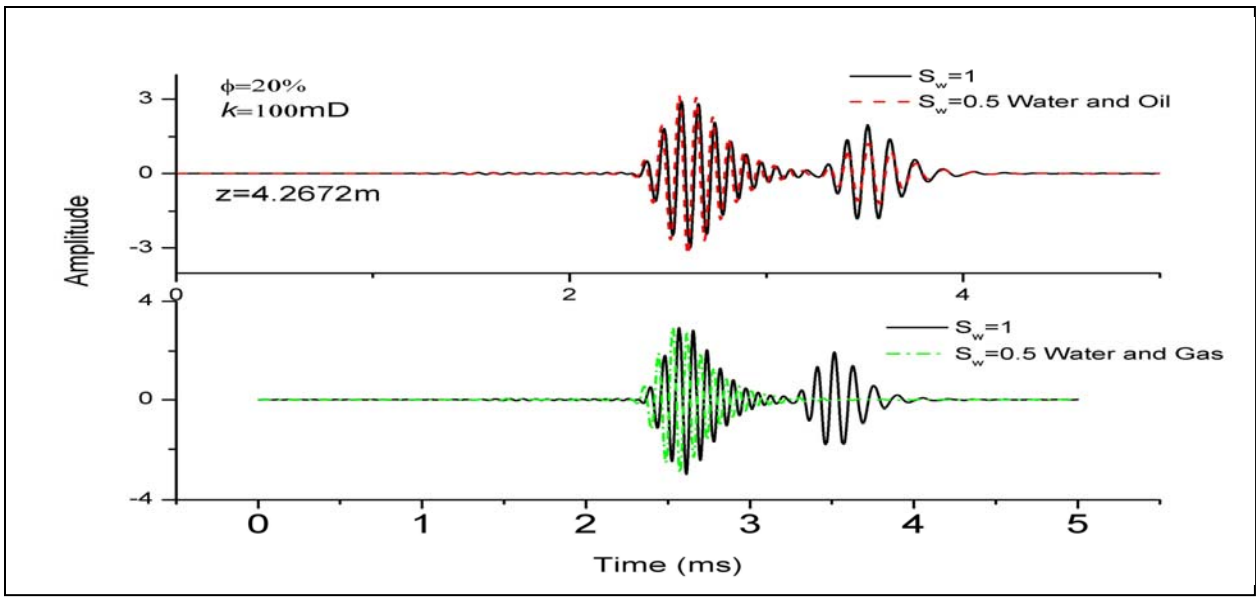

Figure 3.12. Dipole waveforms computed with the generalized R/T method assuming the borehole model described in Table 3.1.1. The source pulse is a cosine-envelope wavelet. The central frequency of the dipole source is 10 kHz, and the half bandwidth is 4 kHz. Simulations are compared for different values of water saturation of pore fluid.

CHAPTER 4

FAST AND EFFICIENT 2.5D TIME-DOMAIN SIMULATION OF MULTI-POLE SONIC LOGS: ELASTIC AND PORO-ELASTIC TRANSVERSE-ISOTROPIC FORMULATIONS

This chapter describes a new formulation for the numerical simulation of borehole sonic logs in transversely isotropic elastic media. Rock formations are assumed axisymmetric with respect to the borehole axis. The simulation model includes the presence of a borehole as well as monopole, dipole, or quadrupole sources with various types of time-domain excitation functions. Simulations are performed in the time domain using an efficient time-marching algorithm. Numerical discretization of the spatial domain is performed using finite differences and domain truncation is enforced using efficient absorbing boundary conditions. The numerical grid makes use of uniform spatial steps in the radial and vertical directions. Solutions are possible for both elastic and poro-elastic formulations. Simulations can be performed on a PC. A typical single-source, multiple-receiver simulation can be performed within a few minutes of CPU time.

4.1 INTRODUCTION

The numerical modeling of acoustic waves propagating in fluid-filled boreholes is an important procedure for the interpretation of acoustic logging measurements. For realistic reservoir formations, the elastic behavior of porous media embodies the basic phenomenology of borehole wave propagation. Acoustic wave propagation in general porous media was pioneered by Biot (1956). For borehole acoustic logging, to our knowledge, current modeling techniques are based on frequency wave-number methods (FWM) for the case of poro-elastic media. For example, based on the frequency domain solution of Biot's equations, Schmitt (1996) studied acoustic multipole logging in the skeleton and permeability assuming transversely isotropic poro-elastic rock formations.

In this study, we focus on the skeleton or the permeability of transversely isotropic poro-elastic formations. The main objective is to investigate the effects of non-isotropic elastic constants and permeability, separately, and to study the possibility of estimating the vertical- and horizontal-permeability from multipole logging responses. Numerical modeling was performed in the time domain using a velocity-stress formulations derived from Biot-homogenization

theory.

4.2 FORMULATION

Biot's linear theory (1956), (1962a), (1962b) for wave propagation in poro-elastic anisotropic media includes five basic assumptions:

(1) The word 'pore' refers to the effective pores, while the sealed pores are considered to be part of the solid. This means that the fluid phase is continuous;

(2) The pores are randomly distributed in space and are statistically isotropic, which means that the ratio of the pore occupied area to the solid occupied area is independent of the direction of the cross section;

(3) The size of pore scale is much smaller than the wavelength of the propagating waves;

(4) The solid skeleton is considered to have compressibility and shear rigidity, i.e. elastic solid matrix, and the fluid may be compressible;

(5) The deformation of a unit cube is assumed to be completely reversible.

Under these assumptions, we conducted the first-order stress-velocity equations for finite difference modeling below.

4.2.1 The Biot-Newton's dynamical equations

According Biot (1962a), the dynamical equations in cylindrical coordinate can be written as

$$\begin{cases} \rho\partial_t v_r + \rho_f \partial_t q_r = \partial_r \sigma_{rr} + r^{-1}(\sigma_{rr} - \sigma_{\theta\theta}) + r^{-1}\partial_\theta \sigma_{r\theta} + \partial_z \sigma_{rz}, \\ \rho\partial_t v_\theta + \rho_f \partial_t q_\theta = r^{-1}\partial_\theta \sigma_{\theta\theta} + \partial_r \sigma_{r\theta} + 2r^{-1}\sigma_{r\theta} + \partial_z \sigma_{\theta z}, \\ \rho\partial_t v_z + \rho_f \partial_t q_z = \partial_z \sigma_{zz} + \partial_r \sigma_{rz} + r^{-1}\sigma_{rz} + r^{-1}\partial_\theta \sigma_{\theta z}. \end{cases} \tag{4.2.1.1}$$

where,

$\rho - averaging\ material\ density,\ \rho = (1-\phi)\rho_s + \phi\rho_f,\ where\ \rho_s\ and\ \rho_f\ are$
$the\ solid\ and\ fluid\ density,\ respectively;$
$v_i, i = r,\theta,z - particle\ velocities\ of\ the\ skeleton\ along\ r-,\theta-\ and\ z-direction,$
$q_i, i = r,\theta,z - particle\ velocities\ of\ the\ fluid\ along\ r-,\theta-\ and\ z-direction,$
$\sigma_{ij}, i, j = r,\theta,z - stress\ components,$
$\partial_j, j = t,r,\theta,z - derivatives\ of\ time, r-,\theta-\ and\ z-direction.$

4.2.2 The law of relative motion of the fluid in the pores (Dynamic Darcy's law)

According to Biot (1962b), the dynamic Darcy's law in cylindrical coordinate can be written as

$$\begin{cases} -\partial_r p_f = \rho_f \partial_t v_r + m_h \partial_t q_r + b_h q_r, \\ -\partial_\theta p_f = r(\rho_f \partial_t v_\theta + m_h \partial_t q_\theta + b_h q_\theta), \\ -\partial_z p_f = \rho_f \partial_t v_z + m_v \partial_t q_z + b_v q_z. \end{cases} \tag{4.2.2.1}$$

where,

$p_f - fluid\ \ pressure\ in\ the\ pore,$
$m_i = T_i \rho_f / \phi,\ with\ T_i\ (i = h\ or\ v)\ the\ tortuosity,$
$\eta - the\ \ fluid\ \ viscosity,$
$r_i = \kappa_i^{-1}, i = h, v - flow\ resistivity\ along\ horizontal\ or\ vertical\ direction,$
$\qquad\qquad\qquad\qquad which\ is\ the\ inverse\ of\ \ the\ \ permeability,$
$b_i = \eta r_i,\ i = h, v.$

4.2.3 The constitutive equations:

According to Biot's work (1956), the stress-strain and the pore pressure relationships in cylindrical coordinates in a transversely isotropic porous media can be represented as

$$\bar{\boldsymbol{\sigma}} = \mathbf{C}\bar{\boldsymbol{\tau}} + \boldsymbol{\alpha} M \boldsymbol{\varepsilon}, \tag{4.2.3.1}$$

$$p_f = -\boldsymbol{\alpha} M \boldsymbol{\tau} - M\boldsymbol{\varepsilon} \tag{4.2.3.2}$$

where,

$$\bar{\boldsymbol{\sigma}} = \left(\sigma_{rr}, \sigma_{\theta\theta}, \sigma_{zz}, \sigma_{\theta z}, \sigma_{zr}, \sigma_{r\theta}\right)^T, \bar{\boldsymbol{\tau}} = \left(\tau_{rr}, \tau_{\theta\theta}, \tau_{zz}, \tau_{\theta z}, \tau_{zr}, \tau_{r\theta}\right)^T, \boldsymbol{\tau} = \left(\tau_{rr}, \tau_{\theta\theta}, \tau_{zz}\right)^T, \boldsymbol{\varepsilon} = \varepsilon_{rr} + \varepsilon_{\theta\theta} + \varepsilon_{zz};$$

$$\mathbf{C} = \begin{pmatrix} C_{11} & C_{12} & C_{13} & 0 & 0 & 0 \\ C_{12} & C_{11} & C_{13} & 0 & 0 & 0 \\ C_{13} & C_{13} & C_{33} & 0 & 0 & 0 \\ 0 & 0 & 0 & C_{44} & 0 & 0 \\ 0 & 0 & 0 & 0 & C_{44} & 0 \\ 0 & 0 & 0 & 0 & 0 & C_{66} \end{pmatrix}, \qquad \boldsymbol{\alpha} = \begin{pmatrix} \alpha_1 & 0 & 0 \\ 0 & \alpha_2 & 0 \\ 0 & 0 & \alpha_3 \end{pmatrix},$$

with

$C_{11} = c_{11} + \alpha_1^2 M, C_{12} = c_{12} + \alpha_1\alpha_2 M, C_{13} = c_{13} + \alpha_1\alpha_3 M, C_{33} = c_{33} + \alpha_3^2 M, C_{44} = c_{44}, C_{66} = c_{66},$
where c_{ij} *are the drained elastic contants*, C_{ij} *are the undrained elastic contants*;

α_i $(i = 1,2,3)$ *are Biot's effective coefficients and given by* $\alpha_1 = \alpha_2 = 1 - (c_{11} + c_{12} + c_{13})/(3K_s)$, *and* $\alpha_3 = 1 - (2c_{13} + c_{33})/(3K_s)$, *where* K_s *is the bulk modulus of the grains.*
The matrix bulk modulus M *is given by*

$$M = \frac{K_s^2}{D - (2c_{11} + c_{33} + 2c_{12} + 4c_{13})/9}, \; D = K_s\left[1 + \phi\left(K_s / K_f - 1\right)\right],$$

where K_f *is the fluid bulk modulus.*

Further, we define

$$(v,q)_{i(i=r,\theta,z)} = \partial_i (u,w)_i, \; (v,q)_{i,j(i,j=r,\theta,z)} = \partial_j (v,q)_i,$$

where,

u, w – *the displacement vetors of the solid grain and the pore fluid*, *respectively*;
v, q – *the particle velocity vectors of the solid grain and the pore fluid*, *respectively.*

Following Takeuchi and Saito (1972), the strain components in cylindrical coordinates in a transversely isotropic medium can be calculated from the displacement components:

$$\begin{cases} \tau_{rr} = \partial_r u_r, \\ \tau_{\theta\theta} = \dfrac{1}{r}(\partial_\theta u_\theta + u_r), \\ \tau_{zz} = \partial_z u_z; \\ \tau_{\theta z} = \dfrac{1}{r}\partial_\theta u_z + \partial_z u_\theta, \\ \tau_{zr} = \partial_z u_r + \partial_r u_z, \\ \tau_{r\theta} = \partial_r u_\theta - \dfrac{1}{r}u_\theta + \dfrac{1}{r}\partial_\theta u_r. \end{cases} \tag{4.2.3.3}$$

One can obtain the stress-velocity relationships in a transversely isotropic porous media by time differentiating of equations (4.2.3.1):

$$\partial_t \overline{\boldsymbol{\sigma}} = \boldsymbol{\Sigma}\overline{\mathbf{v}} + \boldsymbol{\Psi}\overline{\mathbf{q}}, \tag{4.2.3.4}$$

where

$$\bar{\mathbf{v}} = (v_r, v_\theta, v_z)^T \ , \ \bar{\mathbf{q}} = (q_r, q_\theta, q_z)^T \ ,$$

$$\mathbf{\Sigma} = \begin{pmatrix} C_{11}\partial_r + C_{12}\cdot\frac{1}{r} & C_{12}\cdot\frac{1}{r}\partial_\theta & C_{13}\partial_z \\ C_{12}\partial_r + C_{11}\cdot\frac{1}{r} & C_{11}\cdot\frac{1}{r}\partial_\theta & C_{13}\partial_z \\ C_{13}(\partial_r + \frac{1}{r}) & C_{13}\cdot\frac{1}{r}\partial_\theta & C_{33}\partial_z \\ 0 & C_{44}\cdot\frac{1}{r}\partial_z & C_{44}\cdot\frac{1}{r}\partial_\theta \\ C_{44}\partial_z & 0 & C_{44}\partial_r \\ C_{66}\cdot\frac{1}{r}\partial_\theta & C_{66}(\partial_r - \frac{1}{r}) & 0 \end{pmatrix}, \qquad \mathbf{\Psi} = M\begin{pmatrix} \alpha_1\left(\partial_r + \frac{1}{r}\right) & \alpha_1\cdot\frac{1}{r}\partial_\theta & \alpha_1\partial_z \\ \alpha_1\left(\partial_r + \frac{1}{r}\right) & \alpha_1\cdot\frac{1}{r}\partial_\theta & \alpha_1\partial_z \\ \alpha_3\left(\partial_r + \frac{1}{r}\right) & \alpha_3\cdot\frac{1}{r}\partial_\theta & \alpha_3\partial_z \end{pmatrix},$$

The time derivative of pore pressure can be written as

$$\partial_t p_f = -\alpha_1 M\left[\left(\partial_r + \frac{1}{r}\right)v_r + \frac{1}{r}\partial_\theta v_\theta\right] - \alpha_3 M\partial_z v_z - M\left[\left(\partial_r + \frac{1}{r}\right)q_r + \frac{1}{r}\partial_\theta q_\theta + \partial_z q_z\right] \qquad (4.2.3.5)$$

Equations (4.2.1.1), (4.2.1.2), (4.2.3.4) and (4.2.3.5) are the complete velocity-stress formulations for modeling of low-frequency acoustic wave propagation in TI poroelastic media.

4.2.4 Equations for 2.5D TI poro-elastic media

Following Randall et al. (1991), assuming only point multipole sources centered on the borehole axis, the field components of the azimuthal dependences

$$\begin{aligned} &\{v_r, v_z, q_r, q_z, \sigma_{rr}, \sigma_{\theta\theta}, \sigma_{zz}, \sigma_{zr}, p_f\} \sim \cos(n\theta), \\ &\{v_\theta, q_\theta, \sigma_{r\theta}, \sigma_{\theta z}\} \sim \sin(n\theta) \end{aligned} \qquad (4.2.4.1)$$

and

$$\begin{cases} n=0, \textit{monopole}, \\ n=1, \textit{dipole}, \\ n=2, \textit{qudrapole}. \end{cases}$$ are chosen.

The equations and related quantities are thus changed and can be found in the Appendix.

4.3 NUMERICAL ALGORITHM

4.3.1 Staggered-grid with the field components and parameters

The staggered-grid is more stable and accurate than a regular grid with the same order of differencing (1986). Using the staggered-grid, one should define the field components and parameters on staggered nodes. In this study, we illustrated the staggered-grid in Figure 4.1.

4.3.2 Finite difference algorithm on staggered-grid

Zhang (1999) developed the time integration method for 2D complex geometry poroelastic media. We use this scheme which can be performed for the considered problem as follows:

a) Given velocity components at time $k\Delta t$, the stresses and pressure at time $(k+1/2)\Delta t$ can be obtained from equations (B9), (B10) and (B13) (see the Appendix B).

b) Using (B8) and (B12) (see the Appendix), the particle velocities at time $(k+1)\Delta t$ can be obtained.

c) Loop a) and b) till the required the time length is achieved.

4.3.3 Implementations of the multipole source

The multipole source can be described by different combinations of forces applied in the form of stresses along different directions together with the fluid pressure. For monopole sources, the radial and the vertical forces are applied to σ_{rr} and σ_{zz}, and the volume variation source is applied to $-p_f$. For dipole, the radial or vertical force is applied to σ_{rr} or σ_{zz}, and the volume variation source is applied to $-p_f$. For quadrupole, the azimuthal force is applied to $\sigma_{\theta\theta}$,

and the volume variation source is applied to $-p_f$. The strengths of the sources for the solid and fluid are described by $(1-\phi)g(t)$ and $\phi g(t)$, where ϕ is the porosity and $g(t)$ is the exciting wavelet.

4.3.4 Boundary conditions

We assume the left boundary is always coinciding with vertical axis. At this boundary, symmetry conditions are available, and all of the shear components must be zero. In other words, the displacements and dilatational stresses obey

$$\begin{aligned} u_r^+ &= (-1)^{n+1} u_r^-, \\ u_\theta^+ &= (-1)^{n+1} u_\theta^-, \\ u_z^+ &= (-1)^n u_z^-, \\ \sigma_{ii}^+ &= (-1)^n \sigma_{ii}^-, i = r, \theta, z. \end{aligned} \tag{4.3.4.1}$$

Where n is the order of the multipole, and the right upper subscript "+" and "-" represent the nodes at the left and the right side of the axis. Implementations for artificial boundaries (upper, bottom and right boundaries) are combined one-way sponge filtering and anisotropic filtering methods (2005).

4.4 NUMERICAL TESTS AND EXAMPLES

4.4.1 Tests

- *Comparison with analytical results in homogenous infinite fluid*

  Comparisons between the numerical and analytical results (1986) for multipole sonic waveform in homogenous infinite fluid are illustrated in Figure 4.2. They agree very well.

- *Comparison with analytical result in homogenous infinite elastic TI medium*

  Comparison of the vertical particle velocities between numerical and analytical results (1983) in infinite elastic TI medium is illustrated in Figure 4.3. The receiver is located bellow a vertical point source with central frequency 2.5 kHz. Grid is 200×300, spatial step is 2cm, and time step is 0.001ms. The homogenous TI elastic medium is Meversade clay shale (1986).

- *Comparison with published result in fluid-filled borehole surrounded by elastic TI medium*

  Figure 4.4 illustrates the agreement among the results from the present method, Mittet et al. (1996) finite-difference method and discrete-wavenumber method. The waveform is hydrostatic pressure recorded on the borehole axis 2m below a 8 kHz central frequency source in a fluid-filled borehole with radius of 10cm. The solid formation is Meversade limestone (1986). The grid is 200×360, the spatial step is 1cm, and the time step is 0.001ms. These results agree very well.

4.4.2 Examples

We model sonic logging in a fluid-filled borehole surrounded by a transversely isotropic fast poro-elastic formation. The parameters used are listed in Table 4.1. The phase velocities of the quasi-body waves are given in Table 4.2. The borehole wall is permeable. The grid consists of 200×255 nodes. Using the dipole source of the new Schlumberger's array sonic tool with 1kHz and 3kHz peak frequency, the wavetrains are obtained and shown in Figure 4.5 (a) and (b), respectively. One can easily find that the maximum energy excited by the dipole with 3 kHz peak frequency arrives earlier than that with a 1kHz peak frequency. Dispersion images are obtained using Surfseis software (© Kansas Geological Survey) and are shown in Figure 4.5 (c) and (d), respectively. Phase velocities of Stoneley wave shown in the two dispersion images are the same and exhibit correct values. For the dispersion image corresponding to the dipole with 1kHz peak frequency (see Figure 4.5 (c)), only the energy of Stoneley waves can be observed. On the contrary, one can observe energy of the flexural mode, which starts with the shear wave velocity of the formation (approximating 2101.2m/s) and decreases gradually at higher frequencies, on the dispersion image of 3kHz peak frequency dipole (see Figure 4.5 (d)). The energy of the Stoneley wave is very strong for dipole logging in the low frequency range. In the higher frequency range, i.e., from 7.5~10.5kHz for the current situation, the flexural mode becomes the most important energy in the dispersion image (ref. Figure 4.5 (d)). That is to say, for dipole sonic logging, the flexural mode becomes the main event in the waveform for a narrow band. This was studied in detail by Kurkjian (1985) for elastic formations. Schmitt et al. (1989) studied poro-elastic fast formations, and found that the Stoneley wave excitation (i.e., the repartition of the energy as a function of frequency) occurs at low frequencies, wherein the

flexural mode is associated with the Airy phase and a narrow band.

4.5 SUMMARY

This study focused on wave propagation in transversely isotropic poroelastic media. First, the 2.5D time domain formulations were derived in cylindrical coordinates. By using an appropriate low-order finite difference algorithm, the full-wave modeling on a staggered grid was programmed. Comparisons of numerical results and analytical results in infinite fluid medium and infinite transversely isotropic elastic medium illustrated the effectiveness of the algorithm. Furthermore, the full-wave of a dipole excited in fluid-filled borehole surrounded by a TI elastic medium was compared to previous published results obtained using the discrete-wavenumber method and the finite difference method, which show a very good agreement. As an example, we finally studied the full-wave and dispersion characters of dipole sonic logging in a fluid-filled borehole surrounded by a semi-infinite TI poroelastic fast formation.

Table 4.1 Parameters of fast transversely isotropic poroelastic formation and borehole fluid (From Schmitt (1989))

Parameter	Fast formation	Borehole fluid	Parameter	Fast formation	Borehole fluid
c_{11} (GPa)	33.37	2.25	K_s (GPa)	37.9	0
c_{13} (GPa)	9.13	2.25	K_f (GPa)	2.25	2.25
c_{33} (GPa)	30.34	2.25	η (Mks)	0.001	0.001
c_{44} (GPa)	10.61	0	ϕ (%)	15	1
c_{66} (GPa)	13.26	0	k_H (darcy)	0.1	0
ρ_s (kg/m^3)	2650.	0	k_V (darcy)	0.1	0
v_f (m/s)	1500	1500	T_H	2.24	1
ρ_f (kg/m^3)	1000.	1000	T_V	2.24	1

Table 4.2 Phase velocities of the quasi-body waves in the low frequency range

c_{p1} (m/s)	horizontal	3950.5	2702.4
	vertical	3792.7	2600.5
c_{SV} (m/s)	horizontal	2101.2	1146.2
	vertical	2101.2	1146.2
c_{SH} (m/s)	horizontal	2101.2	1146.2
	vertical	2349.2	1356.2

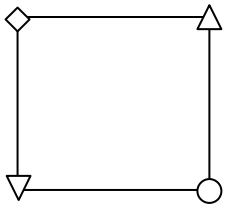

symbol	*node*	*attached variables and parameters*
◊	(i, j)	$v_\theta, q_\theta, \sigma_{rr}, \sigma_{\theta\theta}, \sigma_{zz}, c_{ij}(i, j = 1,2,3), p_f,$ $\rho, \rho_f, \phi, \eta, K_s, K_f$
Δ	$(i+\frac{1}{2}, j)$	$v_r, q_r, \sigma_{r\theta}, \rho, \rho_f, T_h, \kappa_h, \eta, c_{66}$
∇	$(i, j+\frac{1}{2})$	$v_z, q_z, \rho, \rho_f, T_v, \kappa_v, \eta, \sigma_{\theta z}, c_{44}$
O	$(i+\frac{1}{2}, j+\frac{1}{2})$	σ_{rz}, c_{44}

Figure 4.1 The staggered-grid and attached variables and parameters.

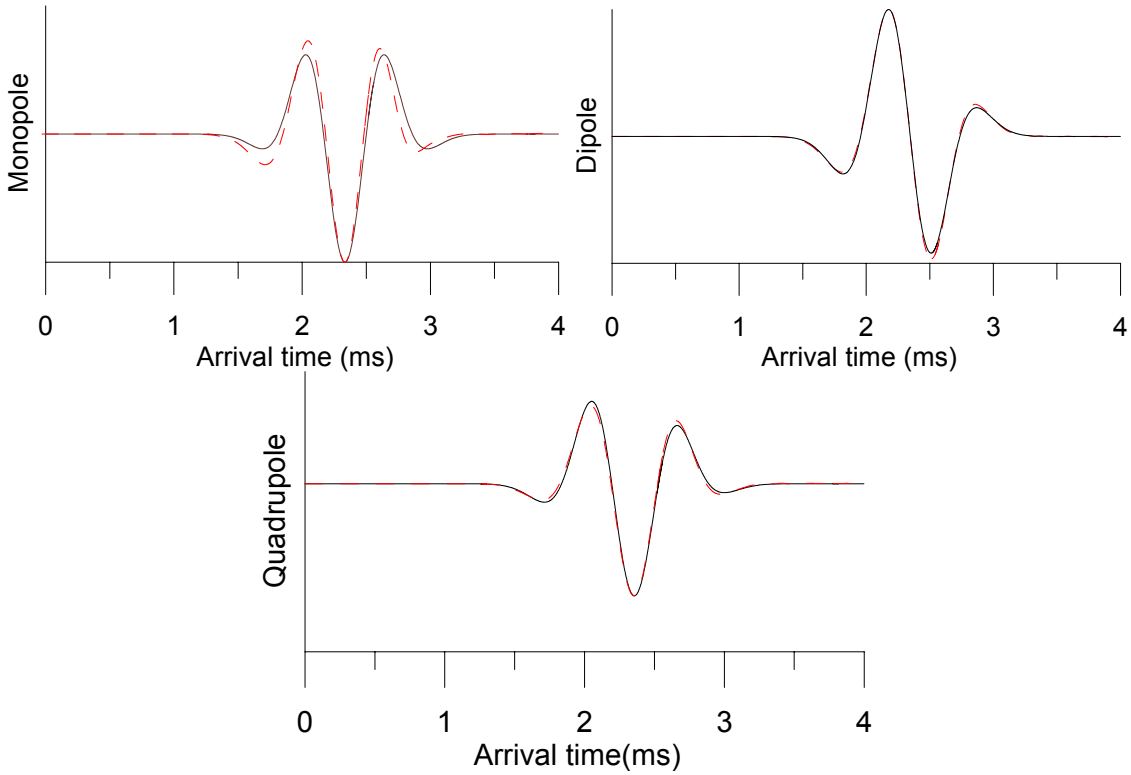

Figure 4.2 Comparisons between numerical results (red dotted line) and analytical results (black solid line) for multipole sonic waveform in the infinite fluid medium.

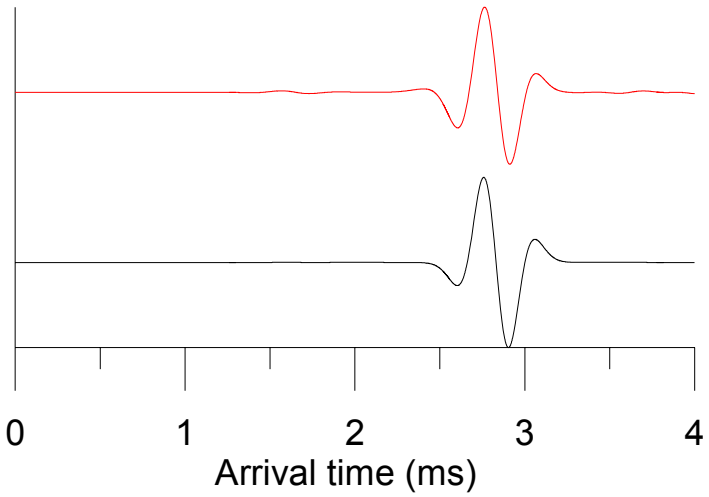

Figure 4.3 Comparison of the vertical particle velocities between numerical (top red line) and analytical results (bottom black line) in infinite elastic TI medium.

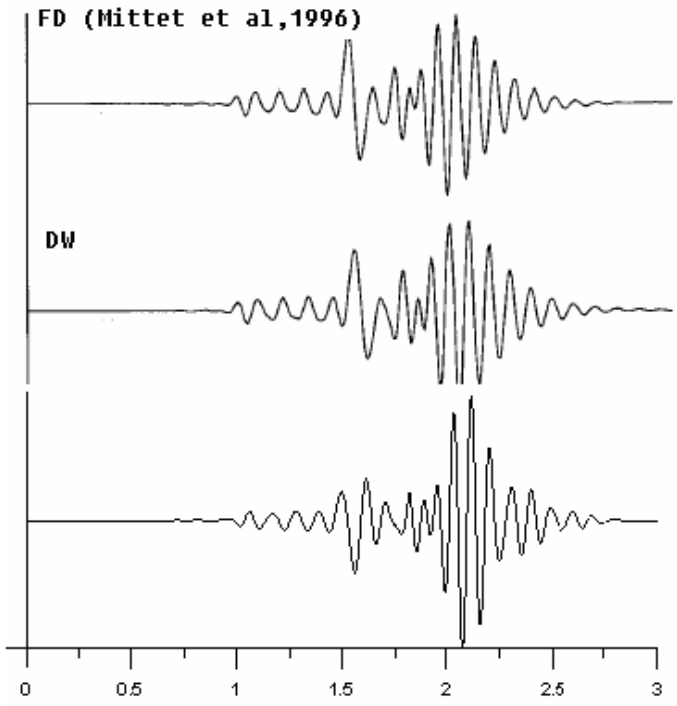

Figure 4.4 Comparisons of numerical result (this study, bottom waveform), result calculated by discrete-wavenumber method (the middle waveform) and numerical result obtained from Mittet et al. (1996) finite-difference method (the top waveform).

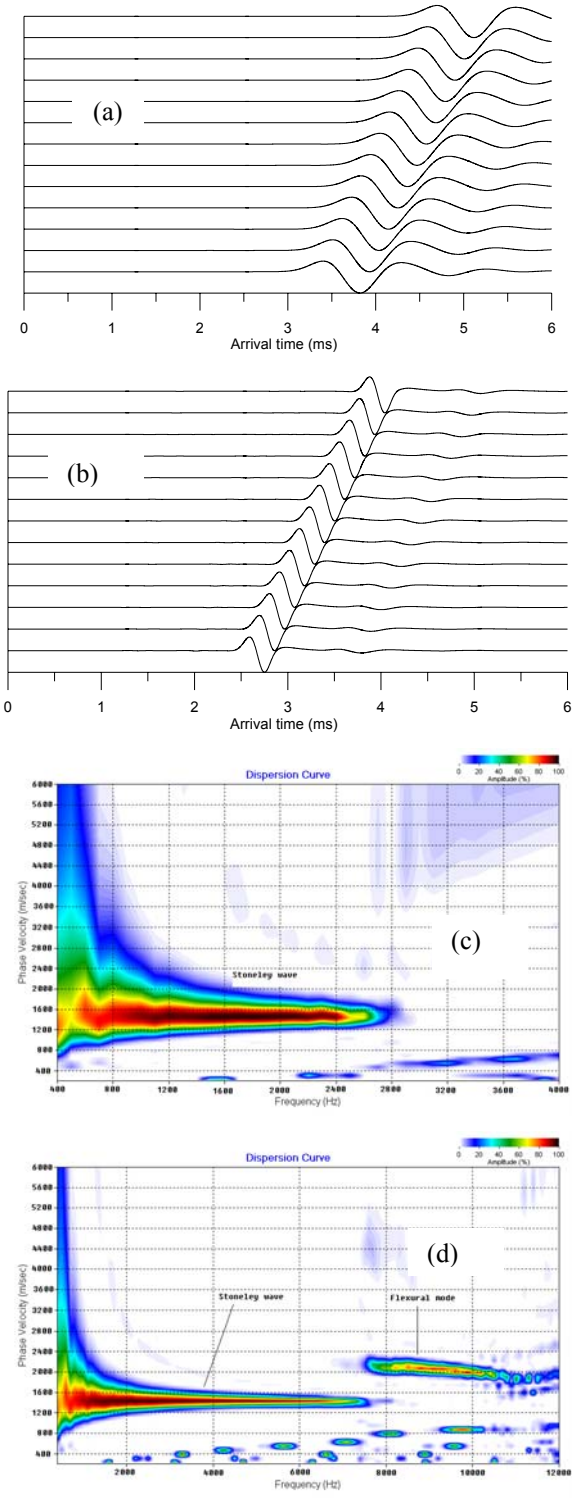

Figure 4.5 The full-waveforms and dispersion images of sonic logging in a fluid-filled borehole surrounded a transversely isotropic poroelastic fast formation. (a) and (c) 1kHz dipole source, (b) and (d) 3kHz dipole source.

CHAPTER 5

NUMERICAL SIMULATION OF BOREHOLE SONIC MEASUREMENTS ACQUIRED IN 3D ANISOTROPIC, DIPPING, AND INVADED ROCK FORMATIONS

This chapter describes a newly developed three-dimensional (3D) finite-difference time-domain (FDTD) algorithm to simulate borehole sonic measurements acquired in inhomogeneous anisotropic, dipping, and invaded rock formations. A second-order explicit FDTD scheme is used to solve the first-order coupled velocity-stress elastic wave equations with staggered-grid central differencing in both space and time. Non-splitting perfectly matched layers (PML) and absorbing boundary conditions (ABC) are used to reduce spurious reflections from the artificial finite computational domain. We discuss the stability, accuracy, and material property averaging of this method when applied to the simulation of wave propagation due to multipole acoustic sources. A 3D FDTD code has been written on the basis of our FDTD formulation with non-splitting PML-ABC. This code is first tested against analytical solutions for full-space homogeneous fluid and solid media and against a real-axis integration method. We then make internal consistency checks using the acoustic-source equivalent principle and the theorem of reciprocity. Finally, we describe results of the simulation of borehole sonic measurements acquired in the presence of various dip angles, anisotropy ratios, and invasion radii. Some interesting propagation phenomena are observed from these simulation results.

5.1 Introduction

Simulation of elastic wave propagation in 3D isotropic and anisotropic media in the presence of dipping rock formations and fluid-filled boreholes remains an open research challenge. It is necessary to fully understand the physics of acoustic and elastic wave propagation in and around the borehole to properly interpret sonic arrival times and amplitudes in terms of petrophysical properties of rock formations.

Due to the complexity of the wave equation and propagating media involved, there are practically no analytical solutions available to simulate acoustic and elastic wave propagation in complex borehole environments. Therefore, in the past, numerical simulation of wave propagation in complex elastic media has been widely used to reproduce borehole sonic

measurements. Three main types of numerical methods have been used to simulate borehole sonic measurements: the finite-difference method (FDM), the finite-element (FE) method including the boundary element method (BEM), and the pseudo-spectral (PS) method.

The FD method is becoming popular among the well logging community because of its flexibility and efficiency to simulate elastic and poro-elastic wave propagation in a variety of rock- formation and petrophysical conditions. Several researchers have applied the FD method to simulate sonic logging measurements. For example, Stephen et al. (1985) described a full 3D numerical solution for isotropic models in cylindrical coordinates using the displacement equations. Yoon et al. (1992) used the 3D staggered-grid method of the displacement equations in a Cartesian coordinate system. Liu et al. (1996) used the velocity-stress system of equations for 3D modeling in isotropic media with a staggered grid. Chen et al. (1998) described a numerical code for the simulation of wave propagation in 3D cylindrical coordinates. For anisotropic elastic wave modeling, Leslie et al. (1992) discussed 2.5D problems, and Chen et al. (1995) described 3D orthorhombic modeling results.

The application of the FD method to simulate wave propagation phenomena in unbounded domains requires artificial boundary conditions to eliminate spurious reflections originating from the edges of the finite computational domain. For example, Lindman's, Liao's, Higdon's, and perfectly-matched-layer (PML) boundary conditions have been used successfully in 2D and 3D simulation algorithms (Chen et al., 1998; Liao et al., 1984; Chen. et al., 1995; Chew et al., 1996). It has been shown that the PML is the most effective ABC condition, and hence it has been widely used in the simulation of wave propagation. Historically, the PML was formulated based on field splitting to avoid convolution operations in the time domain. Recently, Wang et al. (2003) reported a non-splitting PML approach for 2D FD modeling of elastic wave propagation.

In this chapter, the 3D FD time-domain (FDTD) method is used to simulate elastic wave propagation in inhomogeneous and anisotropic rock formations with the presence of a fluid-filled borehole. The second-order explicit FDTD scheme solves the first-order elastic wave equation with staggered-grid central differencing in both space and time. A non-splitting PML absorbing boundary condition (ABC) for 3D simulations is applied to reduce spurious reflections from the finite computational domain. We also discuss the stability and spatial resolution, type of sources

and their modeling, as well as schemes for the averaging of material properties. Computational results are shown for different formation-dip angles, anisotropy ratios, and invasion radii.

5.2 Theory

Consider an inhomogeneous, anisotropic linear elastic medium with mass density ρ, and elastic constant stiffness matrix C. In a Cartesian coordinate frame, the linear elastic wavefields are governed by velocity-stress (v-s) equation system

$$\rho \frac{\partial \vec{V}}{\partial t} = D \cdot \vec{T} + \vec{f}, \tag{5.2.1}$$

and

$$\frac{\partial \vec{T}}{\partial t} = C \cdot \vec{\varepsilon} + \vec{m}, \tag{5.2.2}$$

where $\vec{V} = (V_x, V_y, V_z)^T$ is the velocity vector, $\vec{T}$ is the stress vector, and D is the divergence operator,

$$\vec{\varepsilon} = (\frac{\partial V_x}{\partial x}, \frac{\partial V_y}{\partial y}, \frac{\partial V_z}{\partial z}, (\frac{\partial V_z}{\partial y} + \frac{\partial V_y}{\partial z}), (\frac{\partial V_z}{\partial x} + \frac{\partial V_x}{\partial z}),$$
$$, (\frac{\partial V_x}{\partial y} + \frac{\partial V_y}{\partial x}))^T$$

and the superscript T denotes the transpose operation. If the velocity is the total velocity field and the stress is the total stress field, then $\vec{f}$ is the body-force source, and $\vec{m}$ is the moment rate source. Alternatively, if the velocity and the stress are the scattered field, $\vec{f}$ is the equivalent body-force source, and $\vec{m}$ is the equivalent moment rate source. Therefore, one can use $\vec{f}$ or $\vec{m}$ to describe different acoustic multipole sources (Kurkjian, et al., 1986).

Assuming the $e^{-i\omega t}$ time convention, the space-frequency domain v-s equation system is given by

$$-i\omega\rho \cdot \overrightarrow{V_\omega} = D \cdot \overrightarrow{T_\omega} + \overrightarrow{f_\omega}, \tag{5.2.3}$$

and

$$-i\omega \cdot \vec{T}_\omega = C \cdot \overrightarrow{\varepsilon_\omega} + \overrightarrow{m_\omega}, \tag{5.2.4}$$

where $\overrightarrow{V_\omega}$, $\overrightarrow{T_\omega}$, $\overrightarrow{f_\omega}$, $\overrightarrow{\varepsilon_\omega}$, and $\overrightarrow{m_\omega}$ are the frequency-domain counterparts of $\vec{V}$, $\vec{T}$, $\vec{f}$, $\dot{\vec{\varepsilon}}$, and $\vec{m}$, respectively, and ω is angular frequency.

Following Wang et al. (2003), we choose the complex coordinate stretching variables

$$\tilde{p} = \int_0^p s_p(p')dp', p = x, y, z \ , \tag{5.2.5}$$

where $s_p = 1 - i\frac{\Omega_p}{\omega}$ ($\Omega_p \geq 0$). In a PML region, the imaginary part Ω_p is an attenuation factor, whereupon we choose $\Omega_p > 0$. For a regular non-PML region, we choose $\Omega_p = 0$.

The operator $\frac{\partial}{\partial \tilde{p}}$ can be expressed in terms of Cartesian coordinates as $\frac{\partial}{\partial \tilde{p}} = \frac{1}{s_p}\frac{\partial}{\partial p}$, where $p = x, y, z$.

Replacement of the spatial derivatives in equations (5.2.3) and (5.2.4) with those given in terms of complex coordinates, yields the space-frequency domain v-s equation system, given by

$$-i\omega\rho \cdot \overrightarrow{V_\omega} = D'_\omega \cdot \overrightarrow{T_\omega} + \overrightarrow{f_\omega}, \tag{5.2.6}$$

and

$$-i\omega \cdot \vec{T}_\omega = C \cdot \overrightarrow{\varepsilon'_\omega} + \overrightarrow{m_\omega}, \tag{5.2.7}$$

where

$$D'_\omega = \begin{pmatrix} \frac{1}{s_x}\frac{\partial}{\partial x} & 0 & 0 & 0 & \frac{1}{s_z}\frac{\partial}{\partial z} & \frac{1}{s_y}\frac{\partial}{\partial y} \\ 0 & \frac{1}{s_y}\frac{\partial}{\partial y} & 0 & \frac{1}{s_z}\frac{\partial}{\partial z} & 0 & \frac{1}{s_x}\frac{\partial}{\partial x} \\ 0 & 0 & \frac{1}{s_z}\frac{\partial}{\partial z} & \frac{1}{s_y}\frac{\partial}{\partial y} & \frac{1}{s_x}\frac{\partial}{\partial x} & 0 \end{pmatrix},$$

and

$$\overrightarrow{\varepsilon'_\omega} = \left(\frac{1}{s_x}\frac{\partial V_x^{(\omega)}}{\partial x}, \frac{1}{s_y}\frac{\partial V_y^{(\omega)}}{\partial y}, \frac{1}{s_z}\frac{\partial V_z^{(\omega)}}{\partial z}, \left(\frac{1}{s_y}\frac{\partial V_z^{(\omega)}}{\partial y} + \frac{1}{s_z}\frac{\partial V_y^{(\omega)}}{\partial z}\right)\right.$$
$$\left., \left(\frac{1}{s_x}\frac{\partial V_z^{(\omega)}}{\partial x} + \frac{1}{s_z}\frac{\partial V_x^{(\omega)}}{\partial z}\right), \left(\frac{1}{s_y}\frac{\partial V_x^{(\omega)}}{\partial y} + \frac{1}{s_x}\frac{\partial V_y^{(\omega)}}{\partial x}\right)\right)^T.$$

Equations (5.2.6) and (5.2.7) are commonly used for the simulation of elastic wave propagation via space-frequency domain methods.

First, note that the inverse Fourier transform of $\frac{\partial}{\partial \tilde{p}}$ is

$$F^{-1}[\frac{\partial}{\partial \tilde{p}}] = [1 + \phi_p]\frac{\partial}{\partial p}, \tag{5.2.8}$$

where $\phi_p = -u_{-1}(t)\Omega_p e^{-\Omega_p t} *$ is a convolution operator, and $-u_{-1}(t)$ is the unit-step function. Equations (5.2.6) and (5.2.7) can be readily expressed in the time domain using the inverse Fourier transform.

The v-s equation system with the non-splitting PML ABC conditions can be written in compact form as

$$\rho\frac{\partial \vec{V}}{\partial t} = (D + \delta D)\cdot\vec{T} + \vec{f}, \tag{5.2.9}$$

and

$$\frac{\partial \vec{T}}{\partial t} = C\cdot(\vec{\varepsilon} + \delta\vec{\varepsilon}) + \vec{m}, \tag{5.2.10}$$

where

$$\delta D = \begin{pmatrix} \phi_x\frac{\partial}{\partial x} & 0 & 0 & 0 & \phi_z\frac{\partial}{\partial z} & \phi_y\frac{\partial}{\partial y} \\ 0 & \phi_y\frac{\partial}{\partial y} & 0 & \phi_z\frac{\partial}{\partial z} & 0 & \phi_x\frac{\partial}{\partial x} \\ 0 & 0 & \phi_z\frac{\partial}{\partial z} & \phi_y\frac{\partial}{\partial y} & \phi_x\frac{\partial}{\partial x} & 0 \end{pmatrix},$$

and

$$\delta\vec{\varepsilon} = (\phi_x\frac{\partial V_x}{\partial x}, \phi_y\frac{\partial V_y}{\partial y}, \phi_z\frac{\partial V_z}{\partial z}, (\phi_y\frac{\partial V_z}{\partial y} + \phi_z\frac{\partial V_y}{\partial z}),$$
$$(\phi_x\frac{\partial V_z}{\partial x} + \phi_z\frac{\partial V_x}{\partial z}), (\phi_y\frac{\partial V_x}{\partial y} + \phi_x\frac{\partial V_y}{\partial x}))^T.$$

Obviously, equations (5.2.9) and (5.2.10) reduce to the original v-s equations (5.2.1) and (5.2.2) in the domain of interest, where Ω_p=0.

To simulate the wave field using the FDTD method, we approximate the v-s equations (5.2.9) through (5.2.10) with a centered differencing scheme and staggered grids both in the spatial and temporal domains. These final FD equations embody a leap-frog time-stepping system.

5.3 Numerical Examples

We have programmed the novel 3D FDTD algorithm described above with non-splitting PML absorbing boundary conditions in the presence of anisotropic elastic media using FORTRAN and a PC computer. The code is first tested against analytical solutions for full-space homogeneous fluid and solid media and against real-axis integration (RAI) methods (Schmitt, 1988). Subsequently, we make internal consistency checks using the acoustic source equivalent principle and the theorem of reciprocity. Simulations are performed for different formation-dip angles, anisotropy ratios, and invasion radii. We assume that the acoustic source is an x-directed dipole and that its time signature is the second-order derivative of the Gaussian function with a central frequency equal to 1 kHz. As illustrated in Figure 5.1, the measurement acquisition system consists of a source located at (x, y, z) = (0, 0, 0) and 10 receivers deployed at (x, y, z) = (0, 0, 1+(k-1)*0.05, k=1,2,…, 10). We make use of a non-uniform spatial grid wherein the minimum grid size is $\Delta x = \Delta y = \Delta z = 0.025$m, and the time step is $\Delta t = 5\mu s$. On the horizontal plane, variable grid steps are determined with the optimal grid method described by Asvadurov et al., 2000. The assumed 3D formation model is schematically shown in Figure 5.1. Figures 5.2 and 5.3 compare the x-component of the velocity, Vx, simulated for various formation-dip angles in the presence of both anisotropic and isotropic layered formations, as well as a fluid-filled borehole and invasion. Figure 5.4 compares simulations of Vx performed for various anisotropic factors in a layered formation dipping at an angle of 60 degrees in the presence of a fluid-filled borehole and invasion. Finally, Figures 5.5 and 5.6 compare simulations of Vx for different invasion radii in an anisotropic layered formation dipping at an angle of 60 degrees and in the presence of a fluid-filled borehole.

5.4 Conclusions

We have developed, implemented, and tested a novel 3D FDTD algorithm to simulate borehole sonic measurements acquired in dipping, anisotropic, and invaded formations in the

presence of a fluid-filled borehole. This algorithm solves the first-order coupled velocity-stress elastic wave equations with second-order explicit staggered-grid central finite differences in both space and time. Non-splitting PML absorbing boundary conditions are used to effectively truncate the computational domain with minimum influence of spurious reflections. We have benchmarked the algorithm against analytical solution and have shown its application to the numerical simulation of borehole sonic measurements acquired in dipping, anisotropic, and invaded rock formations.

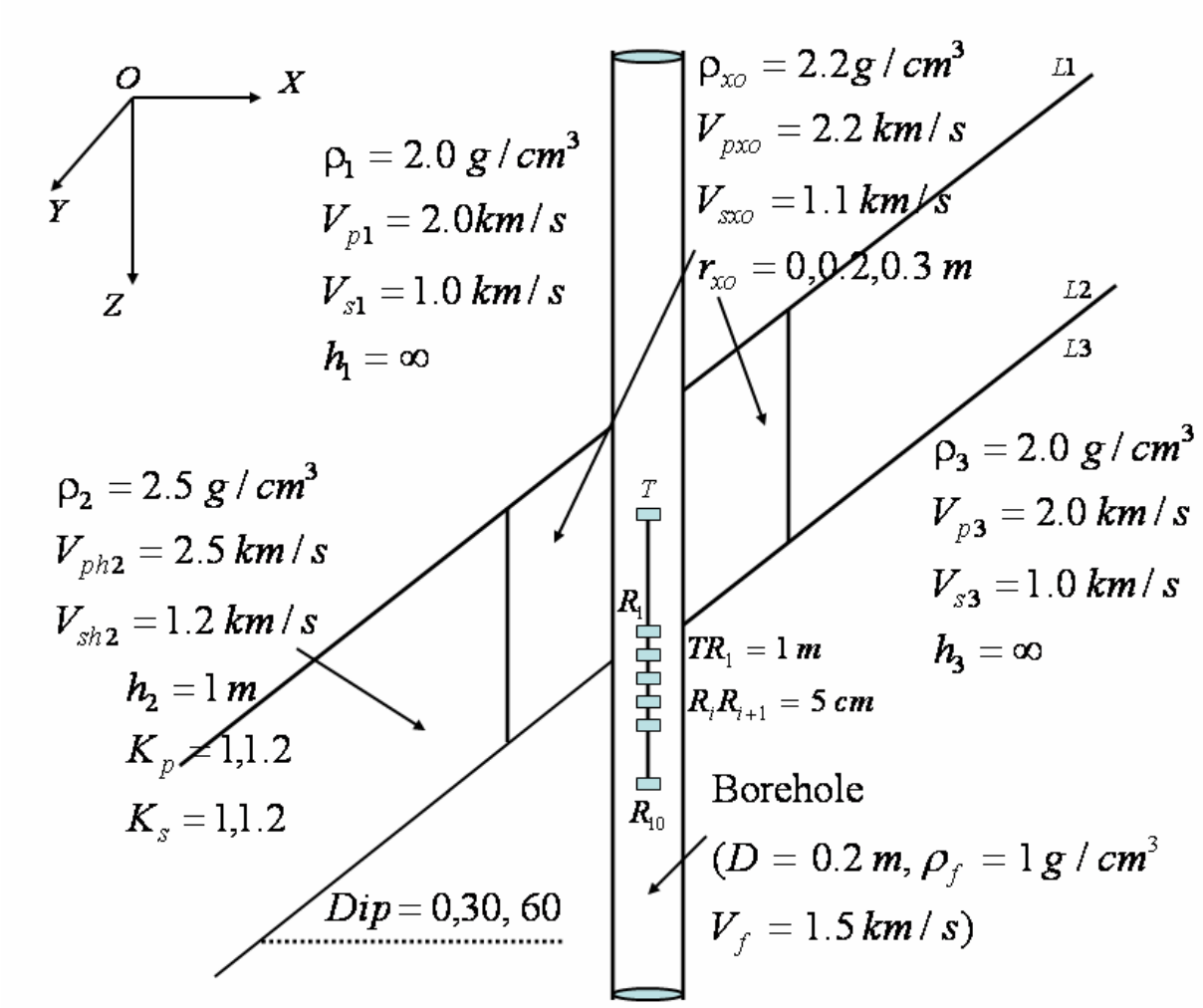

Figure 5.1: Description of the dipping and anisotropic layered formation model assumed in the numerical simulations of borehole sonic measurements.

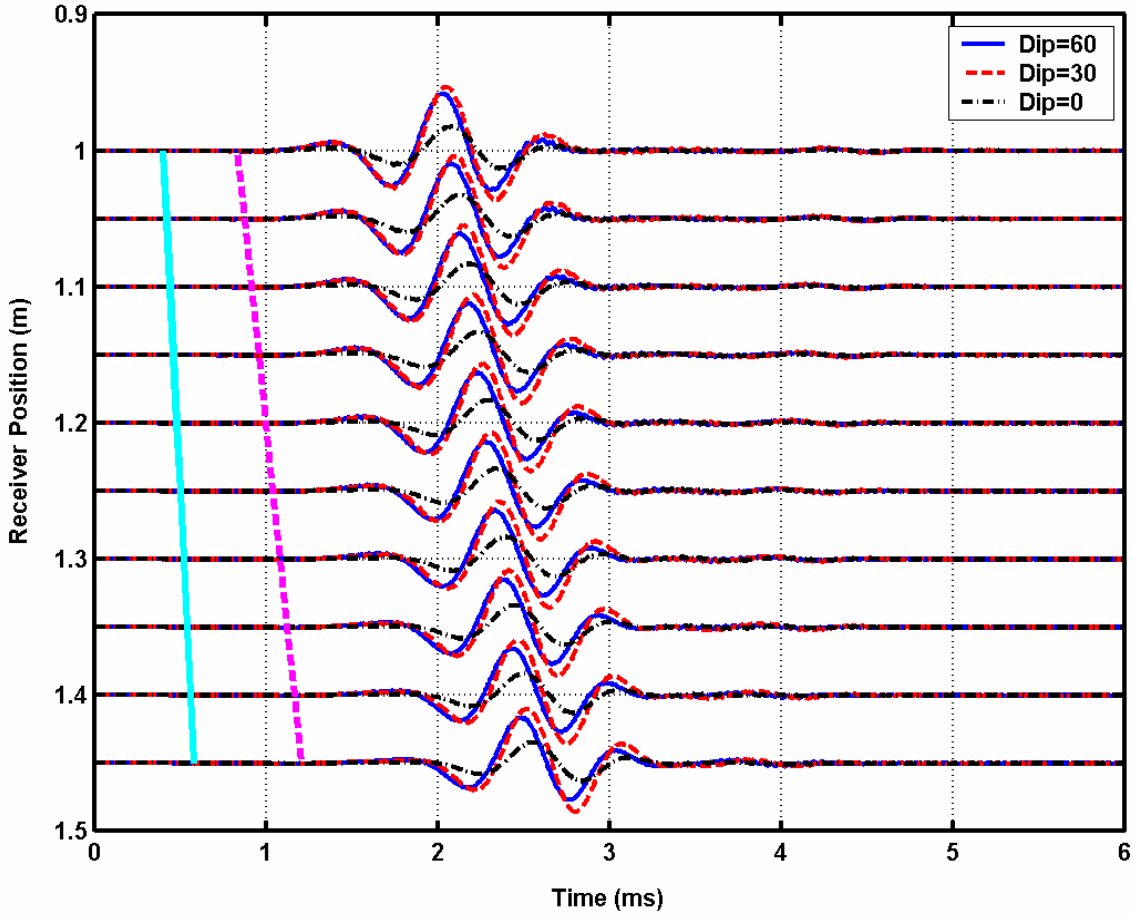

Figure 5.2: Comparison of Vx for different dip angles of an anisotropic layered formation model.

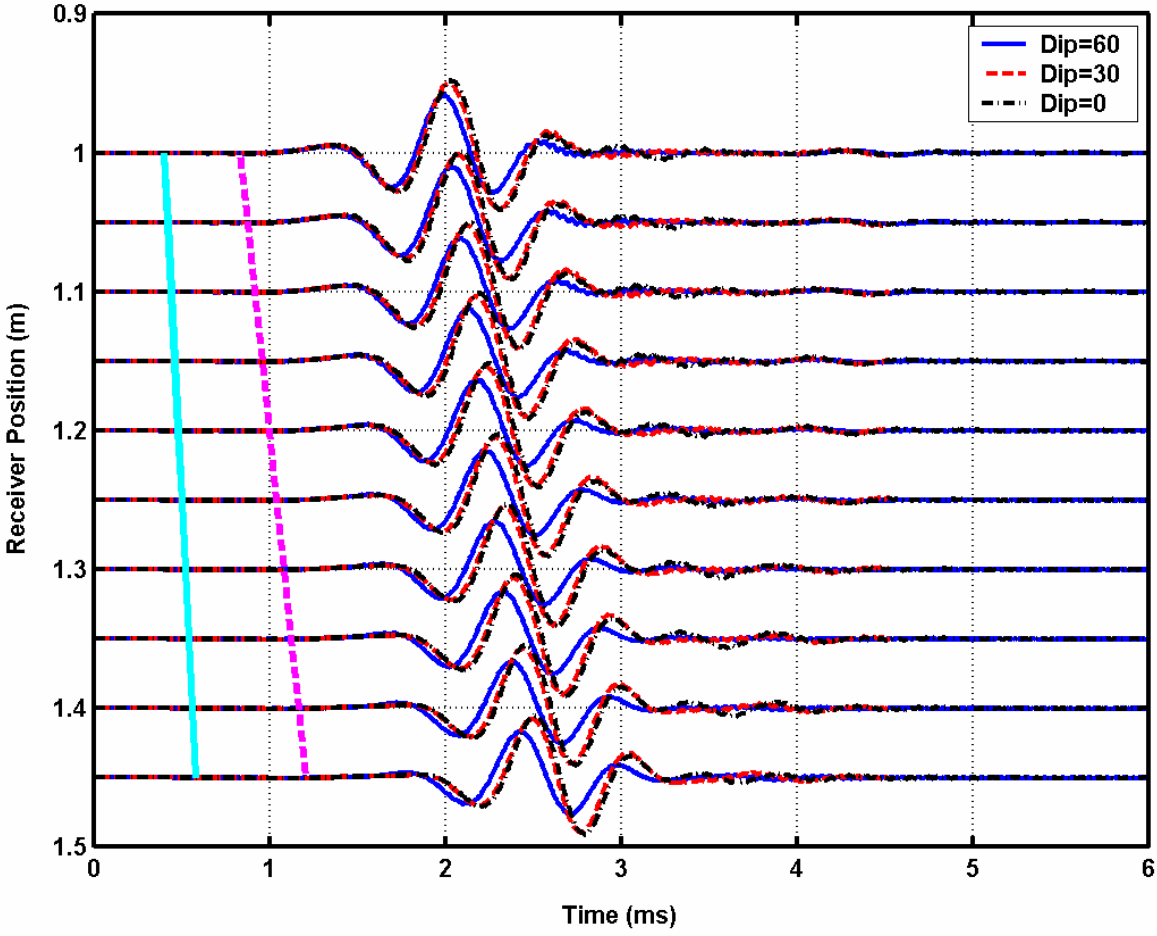

Figure 5.3: Comparison of Vx for different dip angles of an isotropic layered formation model.

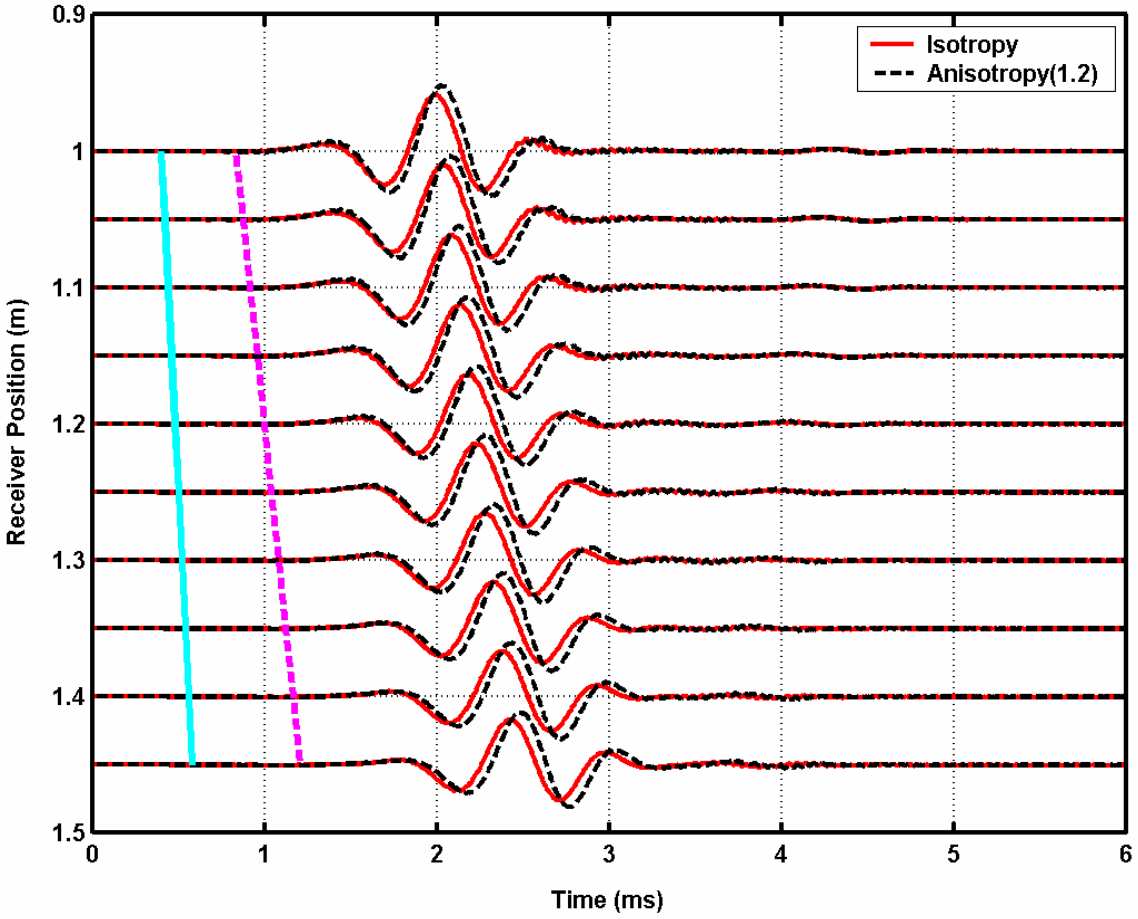

Figure 5.4: Comparison of Vx with and without TI anisotropy in a dipping (60 degrees) layered formation model.

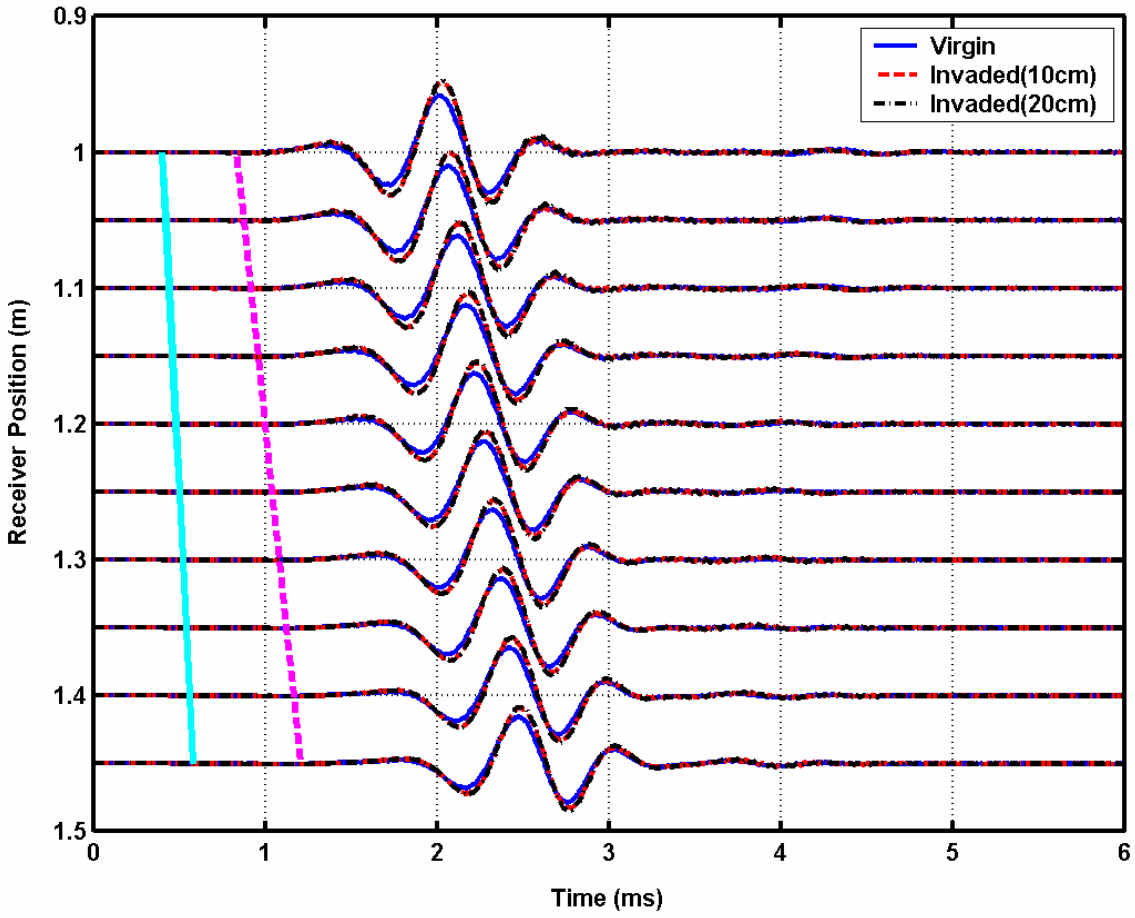

Figure 5.5: Comparison of Vx for different invasion radii in a dipping (60 degrees) anisotropic layered formation model.

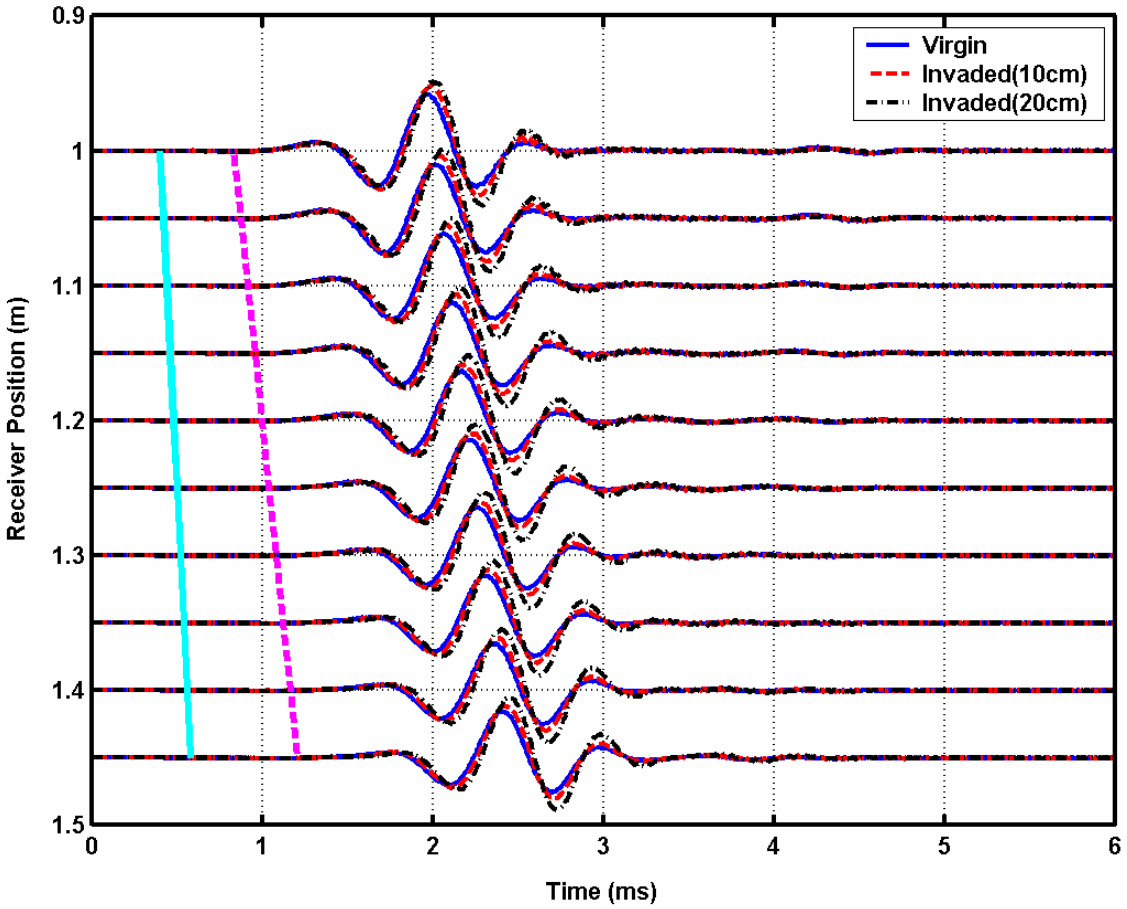

Figure 5.6: Comparison of Vx for different invasion radii in a dipping (60 degrees) isotropic layered formation model.

CHAPTER 6

COMBINED INVERSION OF BOREHOLE RESISTIVITY AND SONIC MEASUREMENTS TO ESTIMATE WATER SATURATION, POROSITY, AND DRY-ROCK ELASTIC MODULI IN THE PRESENCE OF INVASION

Water saturation, porosity and dry-rock (skeleton) elastic moduli are often evaluated independently using measurements that obey different physical principles. Such an interpretation methodology does not take into account possible deterministic or statistical relationships between different physical measurements when probing the same rock formation. We describe a new inversion-based method that combines resistivity and sonic borehole measurements to estimate the four properties simultaneously. The objective of the combined inversion is to suppress ambiguity in the estimation of in-situ properties thereby improving the accuracy and reliability of the results over traditional methods.

We assume a radial one-dimensional model to develop the numerical simulation and inversion components of the study. Moreover, for simplicity we assume invasion in the form of a single piston-like fluid saturation front with one invaded and one virgin zone. The inversion is driven by array-induction and sonic waveform measurements. We use the numerical-mode-matching method and the frequency-wavenumber domain method to simulate induction and sonic measurements, respectively. Induction measurements are related to water saturation and porosity via Archie's equations. For sonic measurements, we resort to Biot-Gassmann's equation to relate the saturated rock's elastic moduli to porosity and fluid saturation. The distorted Born iterative method and a modified preconditioned conjugate gradient method are used for the inversion of induction and sonic measurements, respectively

Results confirm that the combined use of resistivity and sonic measurements considerably reduces ambiguity in the inversion and provides reliable estimates of saturation in both the invaded and virgin zones. Moreover, inclusion of the dry-rock elastic moduli as independent variables avoids enforcing a lithology-specific relationship to porosity.

6.1 INTRODUCTION

Water saturation, S_w, and porosity, ϕ, play important roles in well-log interpretation and formation evaluation, while dry-rock bulk modulus, K_d, and dry-rock shear modulus, μ_d, are indispensable parameters for fluid substitution in the study of seismic properties of rocks.

Generally, S_w is computed using Archie's equation with prior knowledge of ϕ. Porosity is commonly calculated from other measurements, such as neutron and/or density logs, and is often biased by environmental factors as well as by specific assumptions about matrix and fluid properties. This introduces additional biases in the estimation of water saturation. To reduce such an adverse effect, ϕ can be introduced as an additional unknown while evaluating water saturation. However, it is found that resistivity measurements are only sensitive to the product $\phi^m S_w^n$. In other words, resistivity measurements alone can not render separate estimates of S_w and ϕ. One has to include additional data in the estimation method to circumvent this lack of sensitivity.

For the case of elastic properties of rocks, the implementation of fluid substitution procedures requires specific knowledge about K_d and μ_d. Commonly, K_d is derived from velocity measurements performed on controlled-humidity dried core samples. It can also be calculated using lithology-dependent empirical relationships based on well-log data. The first method is cost prohibitive as it often requires the testing of a significant number of core samples. Likewise, empirical relationships for K_d are often established for specific rocks models within specific pressure regimes and hence cannot be generalized for different lithology transitions and/or depths of burial. One has to exercise caution when applying these relationships in the absence of core measurements.

Advances in numerical modeling techniques make it possible to accurately quantify environmental effects on sonic measurements. This provides the possibility of correcting velocity and density for these effects with an inversion-based method. When velocity and density are properly estimated, one can use these estimates to calculate K_d and μ_d. Alternatively, one may resort to Gassmann's equation to estimate K_d, which in turn requires knowledge of S_w and ϕ. Recalling that $\phi^m S_w^n$ can be determined from the inversion of borehole resistivity data, if we further assume that the fluid components are known, then S_w and ϕ can be derived from the volume-average equation of density together with knowledge of the product $\phi^m S_w^n$.

Inversion of array-sonic measurements has proven challenging due to both the large data size involved and the inherent strong nonlinearity of the problem. Different inversion methods have been proposed to estimate rock elastic properties from sonic measurements. Travel-time tomography is based upon a high-frequency approximation and utilizes first arrivals; it has been

well-accepted by formation-evaluation practitioners due to its efficiency and robustness (Hornby, 1993). Full-wave inverse scattering methods have also been proposed to use the information contained in sonic waveforms and has gained some attention over the past years (Tarantola, 1984, Mora, 1987, and Chi et al., 2004). Recently, Sinha et al. (2005) introduced linear inversion methods to estimate radial variations of shear slowness from flexural and Stoneley dispersions. Their work was based on the extraction of dispersion information together with a linear perturbation technique that assumes small variations of elastic properties from a depth-dependent background.

The inversion method developed in this chapter falls into the category of full-wave nonlinear inverse scattering. In so doing, we introduce a modified preconditioned conjugate gradient method to minimize the quadratic cost function and to expedite the inversion. In addition, we use the average trace normalization method to reduce the dependence of waveforms on the amplitude spectrum of the sonic source.

In the following sections, we first introduce the conceptual basis of the proposed inversion method to combine borehole induction and sonic measurements for the in-situ estimation of elastic moduli of rocks. The method is based on the presence of radial zones of invaded and virgin fluid distributions. These distinct zones of fluid saturation provide the necessary measurement sensitivity (and hence degrees of freedom) to estimate K_d and μ_d as well as porosity and fluid saturation. Subsequently, we appraise the accuracy and reliability of the inversion method on several synthetic examples that include slow and fast sandstone formations. The examples are constructed based on actual field measurements. Even though the combined inversion method is readily applicable to the interpretation of field measurements, in this chapter we focus our attention exclusively to noisy synthetic measurements.

6.2 METHOD

We assume a radial one-dimensional (1D) model to develop the numerical simulation and inversion components of the study. As described in Figure 6.1, the radial profile of invasion includes a borehole and flushed and virgin zones.

To better quantify the invasion profile, we use array induction and sonic data as the input measurements to the inversion. The assumed induction and sonic tools are AIT-H[1] and Sonic

[1] Trademark of Schlumberger

Scanner*, respectively. Array induction measurements include 16 signals with different radial lengths of investigation. We use only 8 in-phase signals, which exhibit high radial resolution and long-enough radial length of investigation for general problems. Figure 6.2 shows the configuration of the assumed sonic tool. It provides a combination of monopole and dipole waveforms in the frequency range from 100 Hz to 10 kHz. In total, there are 5 transmitters and 13 receivers, thereby yielding a large data set to describe the mechanical properties of the surrounding formation in great detail. However, in this study we only make use of data acquired with the lower near monopole transmitter. The field excited by a monopole source attenuates slower than that of a dipole source, and hence is more amenable to inversion. In addition, this choice of source has higher radial resolution than using the far monopole source, thereby providing a data set more sensitive to the variation of components of pore-filling fluid included in the invasion profile.

We use the numerical-mode-matching method (Chew et al., 1984; Zhang et al., 1995; Zhang et al., 1999) to simulate induction measurements. This is a hybridization of the 1D finite element method in the radial direction with an analytic solution in the axial direction. Generally, this method is used to simulate induction measurements in the presence of axially-symmetric two-dimensional (2D) formations. For our problem, the implementation is relatively simple because there no reflection and transmission effects are required in the formulation. For the simulation of the sonic tool we use the generalized reflection-transmission method (Chen et al., 1996; Chi and Torres-Verdín, 2004). This is a frequency-wavenumber domain method applicable to the simulation sonic waveforms acquired with a multi-pole source in cylindrically layered elastic media.

As emphasized earlier, in this chapter we are concerned with the response of a monopole source. To model time-domain sonic data, the monopole source is driven with a Ricker wavelet excitation. The selected Ricker wavelet, shown in Figure 6.3, has a central frequency of 8 kHz.

In this study, there are two inverse problems to solve. One is the inversion of array induction data; the other is the inversion of sonic data. Each of the two inverse problems is formulated as the minimization of the quadratic cost function

$$C(\mathbf{m}) = \frac{1}{2}\left\{\left\|\mathbf{d}(\mathbf{m}) - \mathbf{d}^o\right\|_2^2 + \alpha\left\|\mathbf{m} - \mathbf{m}_R\right\|_2^2\right\}, \tag{6.2.1}$$

where $\mathbf{d}^o$ are the measurements, $\mathbf{d}(\mathbf{m})$ are the synthetic data, $\mathbf{m}$ designates the model parameters, $\mathbf{m}_R$ is the reference model, and α is the regularization (stabilization) parameter. For the inversion of array induction data, we use a logarithm transformation to describe both data and unknown parameters instead of their original values. Numerical experiments show that this transformation helps to capitalize on the quasi-linearity of the induction problem. The distorted Born iterative method (DBIM) (Chew and Liu, 1994) is then used to solve the problem iteratively. For the inversion of sonic waveforms, we first normalize the data using the method of average trace normalization (Appendix C), by which we reduce the dependence of the data on the source spectrum. We then use a preconditioned conjugate gradient method (PCG) (Appendix D) to solve the inverse problem with the normalized data. It is noted, however, that there exist alternative methods described in the open technical literature which could also be used for sonic inversion (Tarantola, 1984; Hornby, 1993; Chi et al., 2004; Sinha, 2005).

In both DBIM and PCG, the derivatives of the measurements with respect to model parameters are required to provide a feasible search direction at each iteration. These derivatives are computed using the finite-difference approximation

$$\frac{\partial d}{\partial m} \approx \frac{d(m+\Delta m)-d(m)}{\Delta m}, \tag{6.2.2}$$

where d and m designate a datum and a model parameter, respectively, Δm is the increment on m, and is equal to $0.01m$. For the induction problem, d is apparent conductivity, and m is either ϕ, S_{xo}, S_t, or r_{xo}. Here, S_{xo} and S_t designate the water saturation of flushed and virgin zones, respectively, and r_{xo} is the invasion radius. For the sonic inversion problem, d is pressure, and m designates either density, compressional velocity, or shear velocity of both flushed and virgin zones, i.e. ρ_{xo}, ρ_t, $V_{p,xo}$, $V_{p,t}$, $V_{s,xo}$ and $V_{s,t}$.

For the inversion of induction measurements, the data set includes 8 apparent conductivity measurements. Model parameters are ϕ, S_{xo}, S_t and r_{xo}. Values of ϕ, S_{xo}, and S_t are related to σ_{xo} and σ_t through Archie's equation, namely,

$$\sigma_{xo} = \frac{1}{a}\phi^m S_{xo}^n \sigma_w, \tag{6.2.3a}$$

and

$$\sigma_t = \frac{1}{a}\phi^m S_t^n \sigma_w \,. \tag{6.2.3b}$$

In the above expressions, σ_w, σ_{xo}, and σ_t are the electrical conductivities of formation water, flushed zone, and virgin zone, respectively. Moreover, *a*, *m*, and *n* are the cementation coefficient, cementation exponent, and saturation exponent, respectively. We assume that σ_w is known from independent measurements.

For the inversion of sonic measurements, input data are the micro seismogram in the time-domain (sonic waveforms). Sonic waveforms are first transformed to the frequency-domain. Then the components ranging from 1 kHz to 10 kHz with spacing of 0.5 kHz are selected as input measurements for the inversion. In total, there are 19 frequency components input to the inversion. The reason why we choose frequency samples this way is to use as much as possible information from the formation while keeping the computational overhead at an affordable level. Because each frequency component consists of both real and imaginary parts, the number of data finally doubles to 38. Model parameters involved are ρ_{xo}, ρ_t, $V_{p,xo}$, $V_{p,t}$, $V_{s,xo}$ and $V_{s,t}$.

We use the multiplicative regularization technique introduced by Habashy and Abubakar (2004) to choose the regularization parameter α included in the inversion of induction measurements. Moreover, we choose the model $\mathbf{m}$ obtained in the previous step as the reference model $\mathbf{m}_R$ for the current step. For the inversion of sonic measurements, we simply let $\alpha = 0$.

From Archie's equations, we note that it is the product of S_w and ϕ that is well resolved by the apparent conductivity σ_a, not S_w and ϕ themselves. In fact, any combination of S_w and ϕ satisfying the two equations

$$\phi^m S_{xo}^n = a\sigma_{xo}\sigma_w^{-1}, \tag{6.2.4a}$$

and

$$\left(\frac{S_{xo}}{S_t}\right)^n = \frac{\sigma_{xo}}{\sigma_t}, \tag{6.2.4b}$$

become a minimum of the cost function. These two equations describe a spatial curve in the three-dimensional (3D) space of the triplet (ϕ, S_{xo}, S_t). Therefore, the estimation of S_w and ϕ is essentially ill-posed. However, the estimation of $\phi^m S_w^n$ is generally well-posed considering that we have 8 apparent conductivity measurements with increasingly long radial lengths of investigation while the formation exhibits a step profile of invasion.

We first perform the inversion of array induction data, from which we obtain good estimates of $\phi^m S_w^n$ and r_{xo}. We then fix r_{xo} and perform the inversion of sonic data. The estimated density is used to calculate ϕ. We assume that the pore fluid consists of two phases, either water-oil, or water-gas. According to the volume average equation for density (Smith et al., 2003), one has

$$\rho = \rho_g + \phi\left(\rho_{hc} - \rho_g\right) + \phi S_w\left(\rho_w - \rho_{hc}\right), \tag{6.2.5}$$

where ρ_g, ρ_w are the density of mineral matrix and formation water, respectively, and ρ_{hc} is either ρ_{oil} or ρ_{gas}. This equation, augmented with the knowledge of $\phi^m S_w^n$, yields S_w and ϕ with a non-linear equation solver. From the estimated value of ϕ, one can compute k_d via (Mavko et al., 2003)

$$k_d = \frac{K_{sat}\left(\frac{\phi K_o}{K_{fl}} + 1 - \phi\right) - K_o}{\frac{\phi K_o}{K_{fl}} + \frac{K_{sat}}{K_o} - 1 - \phi}, \tag{6.2.6}$$

where K_{sat} is the bulk modulus of saturated rock, K_o is the bulk modulus of the mineral matrix, and K_{fl} is the bulk modulus of the pore fluid. In Equation (6.2.6), K_{fl} is computed via Reuss' average (Smith et al., 2003), namely,

$$K_{fl}^{-1} = S_w K_w^{-1} + (1 - S_w) K_{hc}^{-1}, \tag{6.2.7}$$

where K_w is the bulk modulus of the pore-filling water, and K_{hc} is the bulk modulus of the pore-filling hydrocarbon. The variable K_{hc} can be either K_{oil} or K_{gas}. Moreover, K_{sat} is derived from the estimated density and velocity by way of the expressions (Mavko et al., 2003)

$$K_{sat} = \rho V_p^2 - \frac{4}{3}\mu_d, \tag{6.2.8a}$$

and

$$\mu_d = \rho V_s^2. \tag{6.2.8b}$$

We note that ρ, V_p and V_s can be either ρ_{xo}, $V_{p,xo}$ and $V_{s,xo}$, or ρ_t, $V_{p,t}$ and $V_{s,t}$.

6.3 NUMERICAL EXAMPLES

In this study, we discuss the application of the combined inversion method to synthetic data generated for clean sandstones. Table 6.1 describes the assumed values of density, bulk, and shear moduli of quartz, the matrix mineral of sandstone. Table 6.2 describes the assumed values of density and bulk modulus of water, oil and gas filling the pore space.

The formation water conductivity, σ_w, and Archie's constants *a*, *m,* and *n* are assumed known from independent measurements. We choose $\sigma_w = 10$ S/m and consider the case of clean sandstones with *a*=1, *m*=2 and *n*=2. The dry-rock elastic moduli K_d and μ_d are calculated using the porosity relationships (Mavko et al., 2003)

$$K_d = K_o\left(1 - \frac{\phi}{\phi_c}\right), \tag{6.3.1a}$$

$$\mu_d = \mu_o\left(1 - \frac{\phi}{\phi_c}\right). \tag{6.3.1b}$$

Here, K_o and μ_o are the bulk and shear moduli of the mineral matrix, and ϕ_c is critical porosity. For sandstones, $\phi_c = 40\%$ (Mavko et al., 2003). To model a fast sandstone, we choose

$\phi = 25\%$, while for the case of a slow sandstone, we choose $\phi = 37.5\%$. Table 6.3 lists the resulting values of K_d and μ_d.

Given σ_w and ϕ, σ_{xo}, and σ_t are computed using Archie's equations. They are input to the forward solver together with the assumed values of S_{xo}, S_t and r_{xo} to generate a synthetic data set, σ_a. With two values of porosity, we obtain two array-induction data sets, shown in Figure 6.4. In all example cases considered below, the values S_{xo}, S_t and r_{xo} are uniformly set to 0.8, 0.2, and 0.25 m, respectively. In addition, borehole radius and borehole conductivity are fixed at 0.1 m and 1 S/m, respectively.

For the inversion of sonic waveforms, we consider four data sets depending on porosity and the type of hydrocarbon filling the pore space of the rock. We first compute ρ_{xo} and ρ_t using Equation (6.2.5), then compute $K_{sat,xo}$ and $K_{sat,t}$ using Equation (6.2.6), finally compute $V_{p,xo}$, $V_{p,t}$, $V_{s,xo}$ and $V_{s,t}$ using Equations (6.2.8a) and (6.2.8b). Table 6.5 describes the computed parameters. Subsequently, we perform numerical simulation to calculate four sets of sonic seismograms and their corresponding frequency spectra, shown in Figure 6.5.

We first perform the inversion on the two resistivity induction data sets contaminated with different levels of noise.

For all cases, we initialize the inversion with values of ϕ, S_{xo} and S_t equal to 0.45, 0.6, and 0.4, respectively. Both borehole radius and borehole conductivity are taken as known parameters and are not included in the inversion. When necessary, noise is added as follows:

$$d \leftarrow d(1+\beta), \tag{6.3.2}$$

where d is any of the eight apparent conductivity measurements, and β is the noise level, for which we choose the two values of 2% and 5%.

Table 6.4 summarizes the corresponding inversion results. We note that the estimates of S_{xo} and S_t are not good even in the presence of noise-free data. However, we find that the product of ϕ and S_{xo} or S_t is close to the true value. In fact, with different initial values of ϕ, we arrive at different values for S_{xo} and S_t, but ϕS_{xo} and ϕS_t remain constant. In these cases, the

product ϕS_w is easily obtained because of our previous assumption that that $m = n = 2$.

Figure 6.6 shows possible solution of ϕ, S_{xo}, and S_t to the inversion of noise-free data for the case of the fast sandstone formation. Any point along the 3D curve is a solution to the inversion. This behavior emphasizes our previous argument about the non-uniqueness of the determination of ϕ, S_{xo}, and S_t using induction measurements alone. The estimate of r_{xo} is generally good. In the presence of noise-free data, r_{xo} is close to the true values. Figures 6.7 and 6.8 describe the iteration history of the minimization procedure. We note that in all example cases no more than 15 iterations are needed to arrive at the results shown in Table 6.4.

We then input the values of r_{xo} obtained from the inversion of induction data to the inversion of sonic waveforms. For the two cases of fast formation, the values of r_{xo} are 0.25, 0.262, and 0.279, respectively, while for the two cases of slow formation, the values are 0.25, 0.257, and 0.266, respectively. Table 6.6 describes the values of ρ, V_p and V_s used to initialize the inversion. We note that these values are not far from their respective true values. In practice, such a choice of initial values is feasible because fairly good estimates of V_p and V_s can be obtained via slowness-time coherence processing or dispersion analysis of sonic waveforms, while good estimates of ρ can be obtained from neutron and/or density logs. Actually, the initial values of ρ, V_p and V_s obtained via these methods can be better than the ones used here, especially those included in the first row of the fast oil-bearing case. When necessary, different levels of noise are added to the spectrum of sonic data ($p_{ij}^{son,obs}$) as done for induction data before initiating the inversion procedure.

Table 6.7 lists the inverted values of ρ, V_p and V_s. Again, as in the inversion of induction data for ϕS_w and r_{xo}, these values converge to their respective true values while the level of noise added to the data becomes gradually small. Close inspection of the results indicates that, in general, the estimates of V_s are the best among all the inverted properties. The accuracy of the inverted values of ρ is lower than the accuracy of the inverted values of V_p and V_s; the largest relative error of 6.7% is observed for ρ_t in the fast oil-bearing case when the noise level is 5%. Relative errors for other estimates are below 5% under the same conditions. Figures 6.9 through 6.12 shows details of the inversion procedure where we observe that the PCG approach works equally well for both fast and slow formation cases, thereby providing confidence in using the

inversion results for the computation of porosity and dry-rock elastic moduli.

After completing the inversion of sonic waveforms, we turn our attention to Equations (6.2.5), (6.2.8a) and (6.2.8b) to calculate ϕ, K_{sat} and u_d. Subsequently, we use ϕ, K_{sat} to calculate K_d via Equation (6.2.6).

We note that the inverted property values in the flushed and virgin zones can both be used to calculate ϕ, K_d and u_d, whereupon we have two values for each of them although they are both single-valued. As a final result, we can use either of them depending on their confidence levels or else use their average.

Table 6.8 summarizes the final inversion results. In general, the estimate of K_d is very good in all cases including noise-contaminated data sets. From Equation (6.2.8b), we know that

$$\frac{\Delta\mu_d}{\mu_d} = \frac{\Delta\rho}{\rho} + 2\frac{\Delta V_s}{V_s}. \tag{6.3.3}$$

Close examination of the changes of ρ and V_s with noise level indicates that ρ and V_s vary in opposite directions in all cases. Therefore, errors in the two variables caused by the presence of noise tend to cancel each other according to the above equation. This behavior explains why the estimate of K_d is close to the true value even in the presence of very noise data sets.

Examination of the inverted values of ϕ indicate that, on occasion, the estimates are insensitive to the level of noise, although sometimes they are also greatly affected by the presence of noise. Sensitivity analysis via Equation (6.2.6) shows that

$$\Delta\phi = \frac{1}{\rho_{hc} - \rho_g}\Delta\rho - \frac{\rho_w - \rho_{hc}}{\rho_{hc} - \rho_g}\Delta(\phi S_w). \tag{6.3.4}$$

Obviously, in oil-bearing formations, the contribution from the second term on the right-hand side of Equation (6.3.4) is comparatively small, hence $\Delta\phi \approx \Delta\rho/(\rho_{hc} - \rho_g)$. That is, the error in ϕ is mainly determined by that of ρ. In the three fast oil-bearing cases, we note that ρ_{xo} is close to its true value. Accordingly, ϕ_{xo} is very close to 0.25, the true value. The corresponding estimate of ρ_t is not good, whereas the error in the estimate of ϕ_t is correspondingly large.

However, for cases of gas-bearing formations the contribution from the second term of Equation (6.3.4) becomes significant and cannot be ignored. When the variations of ρ and ϕS_w with noise level are in line with each other, the corresponding errors tend to cancel each other (see the estimate of ϕ_{xo} in the two gas-bearing cases). When the two variations are opposite to each other the error in ϕ becomes large. Theoretically, this behavior should be observed in the estimate of ϕ_t obtained for the two gas-bearing cases. However, from Table 6.4, we observe that the variation of ϕS_t is significantly small, hence its contribution is negligible, and the error in ϕ_t is basically determined by that of ρ_t. Comparison of errors in the estimates of ϕ_t and ρ_t obtained for the two gas-bearing cases shows that they do follow each other with a change of noise level.

The error in the estimate of S_w is closely related to that of ϕS_w and ϕ, namely,

$$\frac{\Delta S_w}{S_w} = \frac{\Delta(\phi S_w)}{\phi S_w} - \frac{\Delta\phi}{\phi}. \tag{6.3.5}$$

The analysis of the variation of S_w is similar to that of ρ. Accordingly, when changes of ϕS_w and ϕ are in the same direction, the error in S_w becomes small; otherwise, the error in S_w is large. However, when ϕS_w is significantly small, the error is mainly controlled by that of ϕ. Comparison of the columns of ϕ_t and S_t shows that the two properties exhibit exactly the opposite behavior, thereby proving our argument. For S_{xo}, given that the variation of ϕ and S_w are opposite in this region, we observe that the estimate of S_{xo} is generally better than that of S_t.

We also note that the values of S_w and ϕ obtained with the combined inversion approach are more accurate than those estimated with the induction measurements alone. This observation indicates that the inclusion of information from sonic inversion is critical to suppress ambiguity in the inversion of S_w and ϕ.

The sensitivity analysis of K_d is complex due to the nonlinear dependence of this parameter on ϕS_w and ϕ. In general, the estimate for the case of fast formations is better than that of slow formations, and it is better in gas-bearing cases than in oil-bearing cases.

6.4 CONCLUSIONS

We developed a new method for the simultaneous estimation of water saturation, porosity and dry-rock elastic moduli. The estimation effectively combines the information content available in both array-induction measurements and sonic waveforms acquired in the presence of a step profile of radial mud-filtrate invasion. Moreover, the estimation enforces a determinist relationship between common formation properties included in Biot-Gassmann's fluid-substitution equations and Archie's saturation-resistivity equations.

Application of the combined inversion to noisy synthetic data sets confirms that the method provides reliable and accurate estimates of porosity, water saturation, and dry-rock elastic moduli for cases of both fast and slow formations which can be either oil- or gas-bearing. In general, the estimate of dry-rock shear modulus is accurate in all cases even in the presence of 5% measurement noise. Also, it was found that the estimate of dry-rock shear modulus in fast formations was generally better in slow formations than in fast formations. Estimates of water saturation and porosity exhibit a desirably behavior in the presence of noisy measurements manifested by a decrease of accuracy with an increase in the level of measurement noise.

The inclusion of a density estimate yielded by the inversion of sonic data provides an independent relationship which is necessary to reduce non-uniqueness in the determination of water saturation and porosity from induction data. On the other hand, induction data provide the sensitivity to water saturation and porosity necessary to obatine reliable estimates of dry-rock elastic moduli, which otherwise would be difficult to estimate given that sonic data are less sensitive than induction data to variations of porosity and fluid saturation.

In the future, we will investigate the applicability of the combined inversion method to cases of low-porosity sandstone formations as well as carbonate formations. For the cases of shaly-sand and shale-laminated formations, we anticipate the use of different deterministic relationships between porosity, saturation, and dry-rock elastic moduli that can account for the presence of shale.

Table 6.1. Assumed values of density, and bulk and shear moduli of quartz.

ρ(g/cm^3)	K(GPa)	μ(GPa)
2.65	37	44

Table 6.2. Assumed values of density and bulk modulus of water, oil and gas.

	Water	Oil	Gas
ρ(g/cm^3)	1.089	0.749	0.103
K(GPa)	2.38	0.67	0.0208

Table 6.3. Assumed values of dry-rock elastic moduli for the fast and slow sandstone formations considered in this chapter.

	ϕ (%)	K_d (GPa)	μ_d (GPa)
Fast Sandstone	25	13.875	16.5
Slow Sandstone	37.5	2.3125	2.75

Table 6.4. Summary of results obtained from the inversion of array-induction data.

		Noise-free	$\varepsilon = 2\%$	$\varepsilon = 5\%$
Fast sandstone formation	ϕ	0.293	0.289	0.277
	S_{xo}	0.684	0.661	0.653
	S_t	0.171	0.175	0.186
	ϕS_{xo}	0.200	0.191	0.180
	ϕS_t	0.050	0.051	0.051
	r_{xo}	0.250	0.262	0.279
Slow sandstone formation	ϕ	0.404	0.397	0.388
	S_{xo}	0.743	0.738	0.729
	S_t	0.186	0.191	0.198
	ϕS_{xo}	0.300	0.293	0.283
	ϕS_t	0.075	0.076	0.077
	r_{xo}	0.250	0.257	0.266

Table 6.5. Values of density, compressional velocity, and shear velocity assumed for the synthetic models considered in this chapter**.**

CASE	ρ_{xo} (g/cm^3)	ρ_t (g/cm^3)	$V_{p,xo}$ (m/s)	$V_{p,t}$ (m/s)	$V_{s,xo}$ (m/s)	$V_{s,t}$ (m/s)
Fast oil-bearing	2.243	2.192	4126.48	4112.04	2712.39	2743.76
Fast gas-bearing	2.210	2.063	4037.38	4172.91	2732.13	2828.39
Slow oil-bearing	2.039	1.963	2152.80	1988.00	1161.30	1183.72
Slow gas-bearing	1.991	1.769	1766.75	1847.88	1175.35	1246.88

Table 6.6. Values of density, compressional velocity, and shear velocity used to initialize the inversion examples considered in this chapter.

CASE	ρ_{xo} (g/cm^3)	ρ_t (g/cm^3)	$V_{p,xo}$ (m/s)	$V_{p,t}$ (m/s)	$V_{s,xo}$ (m/s)	$V_{s,t}$ (m/s)
Fast oil-bearing	2.3	2.3	4500	4500	3100	3100
Fast gas-bearing	2.3	2.3	4200	4200	2900	2900
Slow oil-bearing	2.1	2.1	2200	2200	1200	1200
Slow gas-bearing	2	2	1900	1900	1300	1300

Table 6.7. Estimated values of density, compressional velocity, and shear velocity for the inversion examples considered in this chapter.

CASE		ρ_{xo} (g/cm^3)	ρ_t (g/cm^3)	$V_{p,xo}$ (m/s)	$V_{p,t}$ (m/s)	$V_{s,xo}$ (m/s)	$V_{s,t}$ (m/s)
Fast oil-bearing	Noise-free	2.243	2.192	4126.44	4111.92	2712.40	2743.75
	$\varepsilon = 2\%$	2.232	2.127	4150.04	4162.83	2711.14	2749.51
	$\varepsilon = 5\%$	2.223	2.043	4188.91	4198.94	2704.47	2773.55
Fast gas-bearing	Noise-free	2.210	2.063	4037.41	4173.03	2732.11	2828.40
	$\varepsilon = 2\%$	2.200	2.007	4052.57	4151.76	2733.46	2828.61
	$\varepsilon = 5\%$	2.196	1.974	4080.22	4148.03	2725.63	2841.53
Slow oil-bearing	Noise-free	2.039	1.963	2152.78	1988.00	1161.30	1183.72
	$\varepsilon = 2\%$	2.009	1.953	2189.40	2010.28	1160.79	1193.81
	$\varepsilon = 5\%$	1.969	1.984	2248.25	2022.21	1160.57	1199.54
Slow gas-bearing	Noise-free	1.991	1.769	1766.76	1847.90	1175.34	1246.88
	$\varepsilon = 2\%$	1.947	1.740	1777.05	1825.44	1179.97	1261.27
	$\varepsilon = 5\%$	1.889	1.719	1788.66	1776.06	1187.44	1282.21

Table 6.8. Estimated values of water saturation, porosity, and dry-rock elastic moduli for the inversion examples considered in this chapter.

CASE		$K_{d,xo}$ (GPa)	$K_{d,t}$ (GPa)	$\mu_{d,xo}$ (GPa)	$\mu_{d,t}$ (GPa)	ϕ_{xo} (%)	ϕ_t (%)	S_{xo} (%)	S_t (%)	$\bar{\phi}$ (%)	$\bar{K}_d$ (GPa)	$\bar{\mu}_d$ (GPa)
Fast oil-bearing	Noise-free	13.874	13.873	16.500	16.500	0.250	0.250	0.800	0.200	0.250	13.873	16.500
	$\varepsilon = 2\%$	14.564	14.436	16.409	16.077	0.254	0.284	0.754	0.178	0.269	14.500	16.243
	$\varepsilon = 5\%$	15.651	14.211	16.259	15.719	0.257	0.328	0.703	0.157	0.293	14.931	15.989
Fast gas-bearing	Noise-free	13.876	13.878	16.500	16.501	0.250	0.250	0.800	0.200	0.250	13.877	16.500
	$\varepsilon = 2\%$	14.082	13.146	16.436	16.059	0.251	0.272	0.763	0.186	0.261	13.614	16.247
	$\varepsilon = 5\%$	14.698	12.675	16.314	15.939	0.248	0.285	0.727	0.181	0.267	13.687	16.126
Slow oil-bearing	Noise-free	2.312	2.312	2.750	2.750	0.375	0.375	0.800	0.200	0.375	2.312	2.750
	$\varepsilon = 2\%$	3.029	2.440	2.707	2.784	0.390	0.380	0.751	0.200	0.385	2.735	2.746
	$\varepsilon = 5\%$	3.919	2.479	2.652	2.855	0.409	0.364	0.692	0.211	0.387	3.200	2.753
Slow gas-bearing	Noise-free	2.313	2.313	2.750	2.750	0.375	0.375	0.800	0.200	0.375	2.313	2.750
	$\varepsilon = 2\%$	2.350	2.048	2.710	2.768	0.390	0.387	0.752	0.196	0.388	2.199	2.739
	$\varepsilon = 5\%$	2.350	1.594	2.663	2.826	0.408	0.395	0.693	0.195	0.402	1.972	2.745

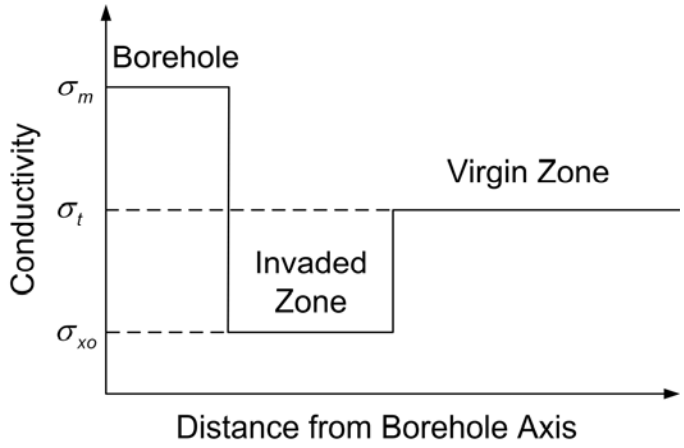

Figure 6.1. Description of the single-step radial profile of invasion assumed in the inversion examples considered in this chapter.

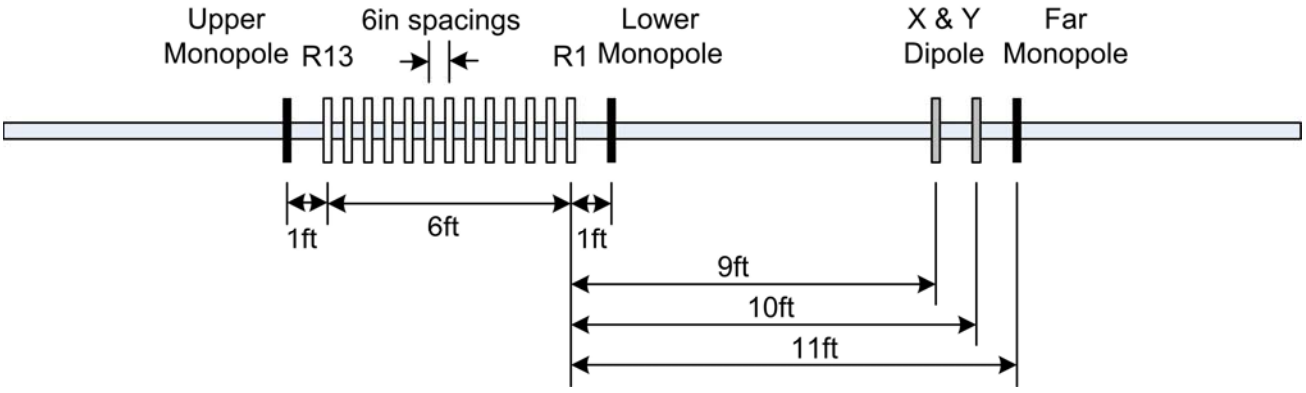

Figure 6.2. Description of the assumed array-sonic tool.

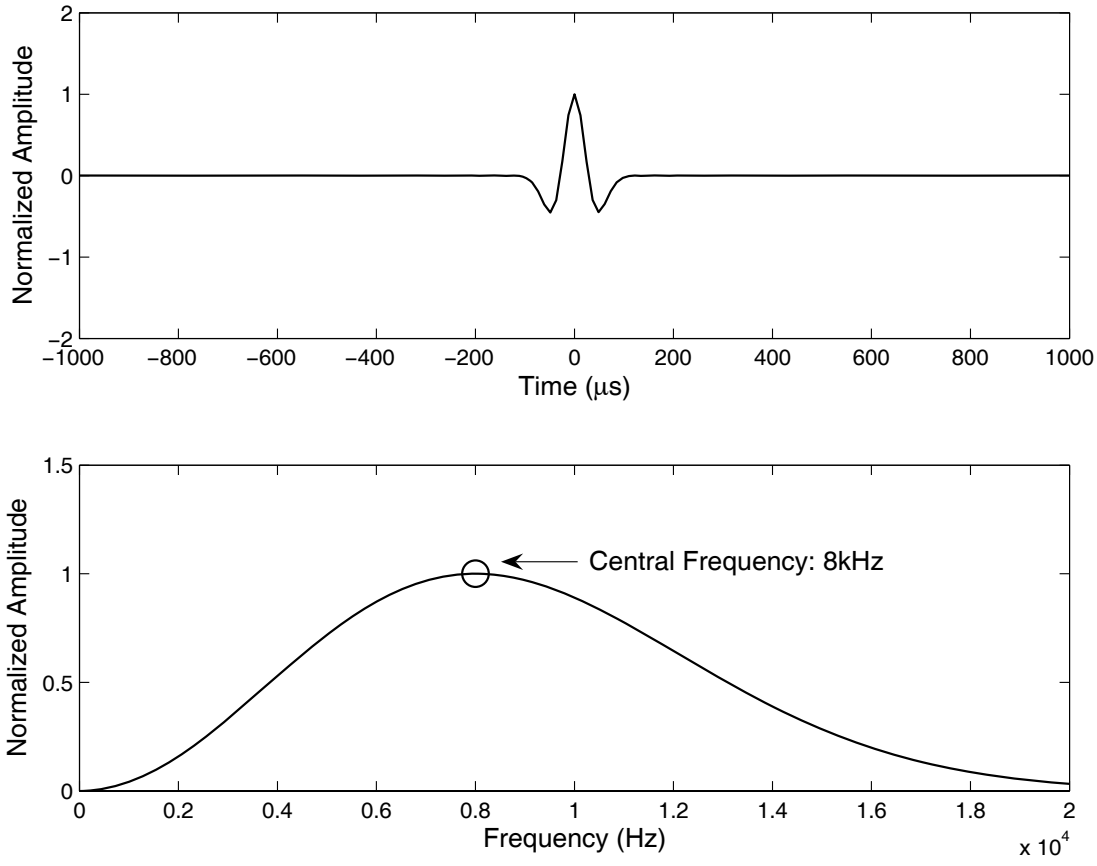

Figure 6.3. Time- and frequency-domain representations of the Ricker wavelet assumed in the simulation of sonic measurements.

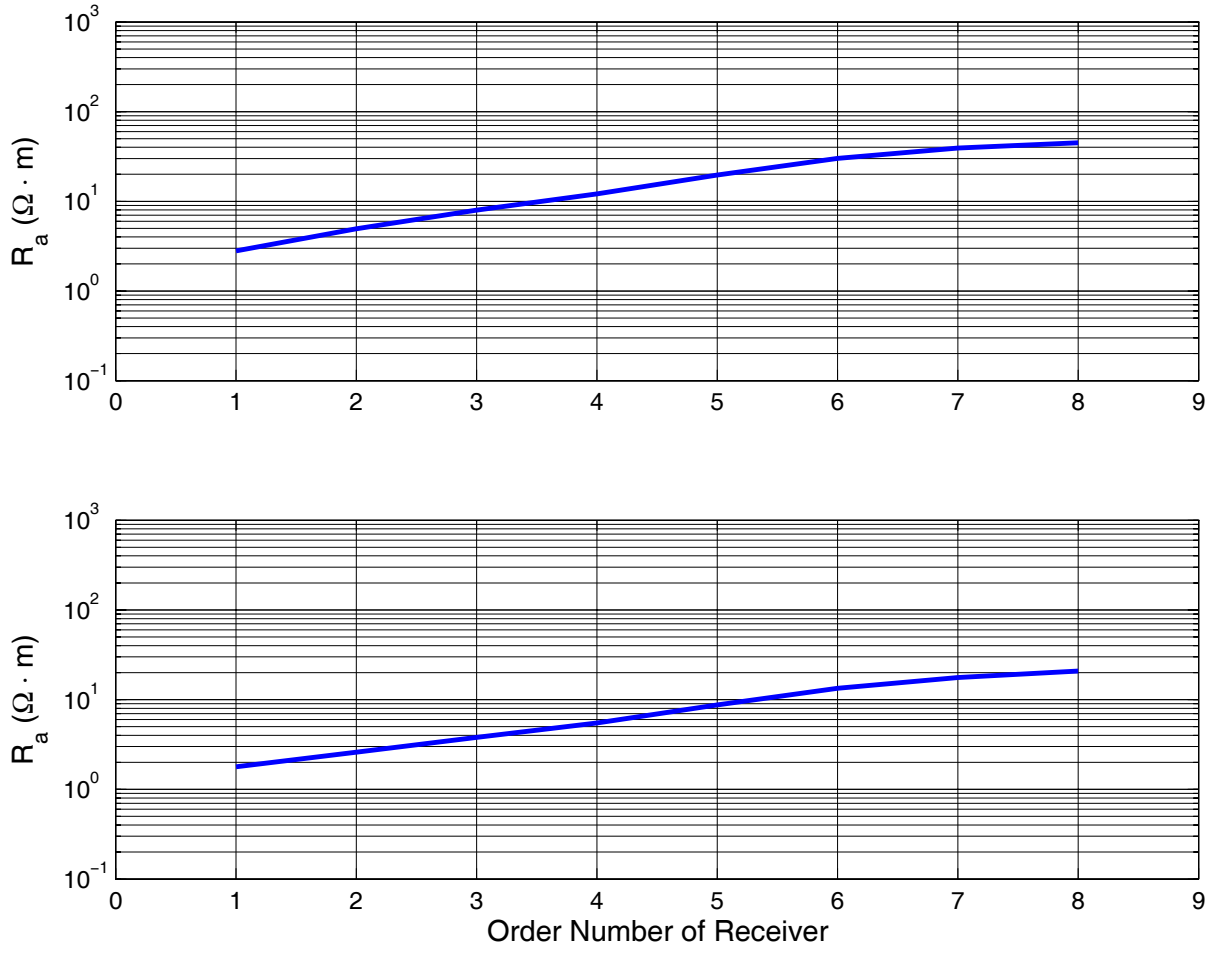

Figure 6.4. Synthetic apparent resistivities (reciprocal of apparent conductivity) simulated for two different cases of clean sandstone formations. The upper and lower panels show apparent resistivities associated with fast and slow sandstones, respectively.

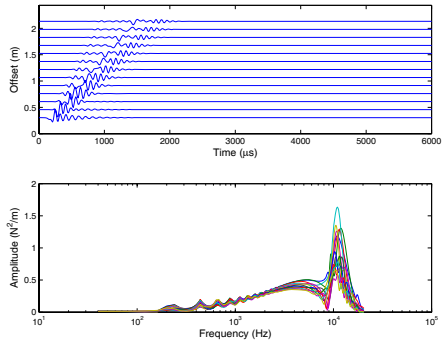

(a)

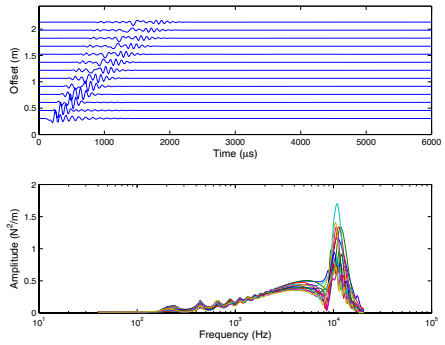

(b)

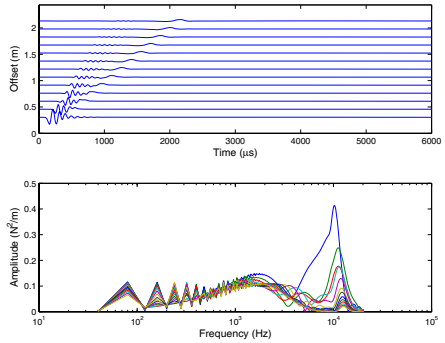

(c)

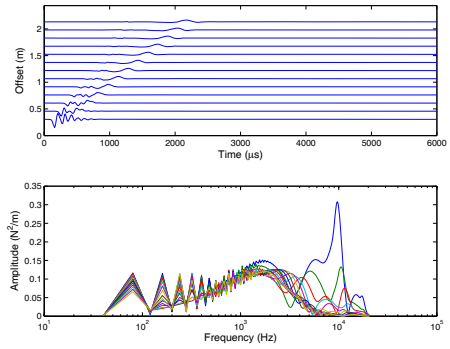

(d)

Figure 6.5. Synthetic sonic waveforms and their frequency spectra associated with four different formation models. (a) and (b) are waveforms for the fast oil- and gas-bearing sandstone, respectively. (c) and (d) are waveforms for the slow oil- and gas-bearing sandstone, respectively.

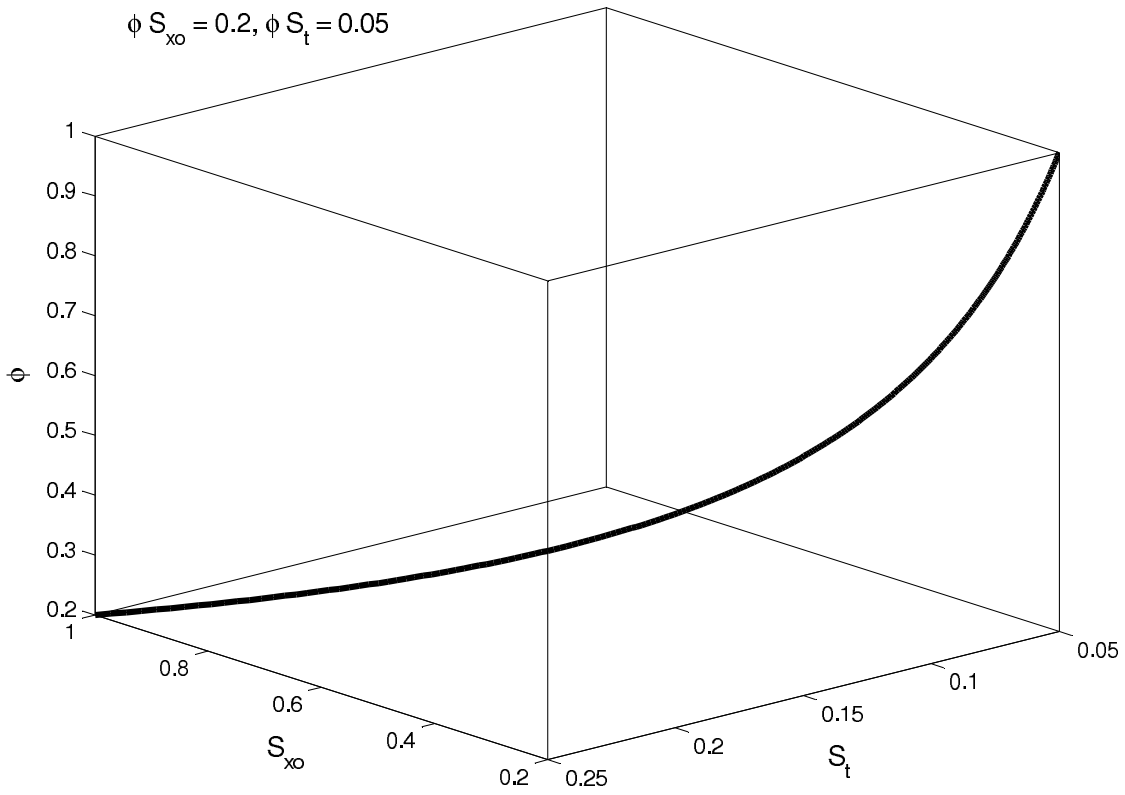

Figure 6.6. Space of plausible porosity-water saturation solutions for the case of a fast sandstone formation. All feasible solutions reside along the curve extending from (0.2, 1, 0.25) to (1, 0.2, 0.05) in the space of triplets ($\phi, \sigma_{xo}, \sigma_t$).

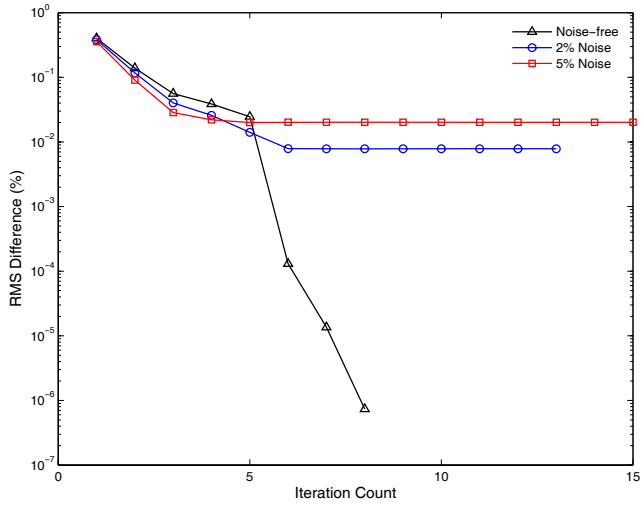

(a)

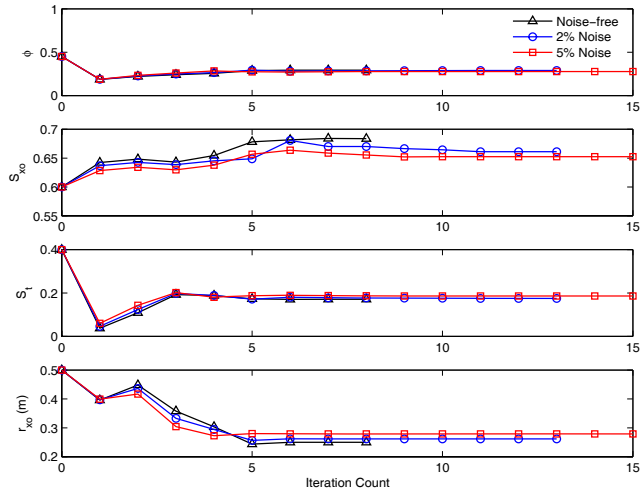

(b)

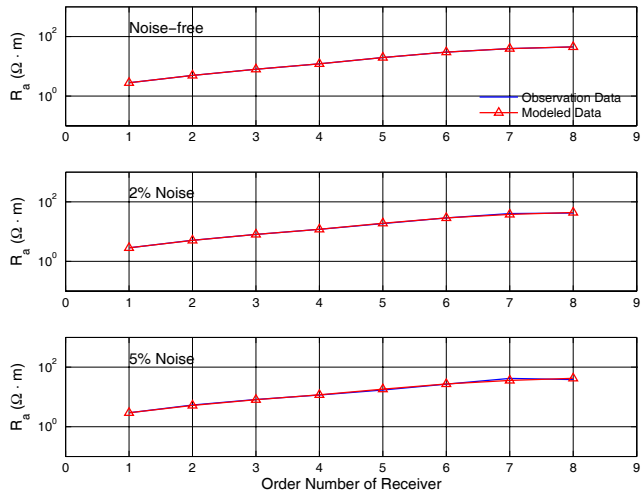

(c)

Figure 6.7. Evolution of data misfit as a function of iteration for the case of array-induction data acquired in a fast sandstone formation. (a) shows the evolution of the RMS difference between simulated and measured array-induction data. (b) shows the evolution of the inverted parameters as a function of iteration. (c) shows the misfit between simulated and measured array-induction data at the end of the minimization.

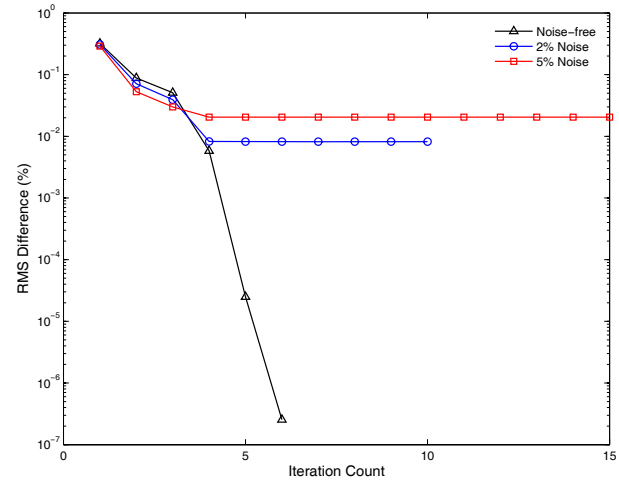

(a)

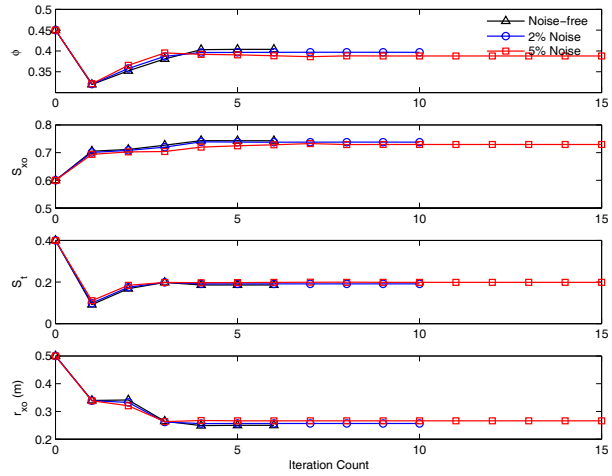

(b)

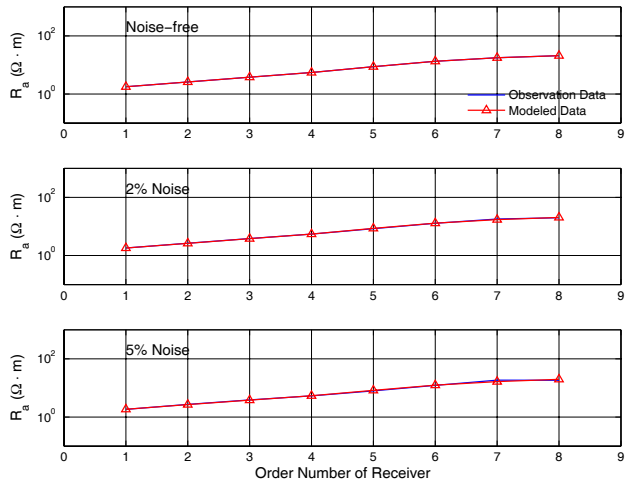

(c)

Figure 6.8. Evolution of data misfit as a function of iteration for the case of array-induction data acquired in a slow sandstone formation. (a) shows the evolution of the RMS difference between simulated and measured array-induction data. (b) shows the evolution of the inverted parameters as a function of iteration. (c) shows the misfit between simulated and measured array-induction data at the end of the minimization.

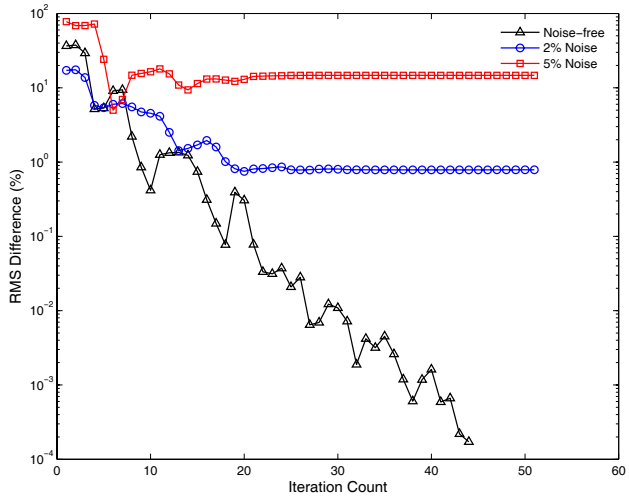

(a)

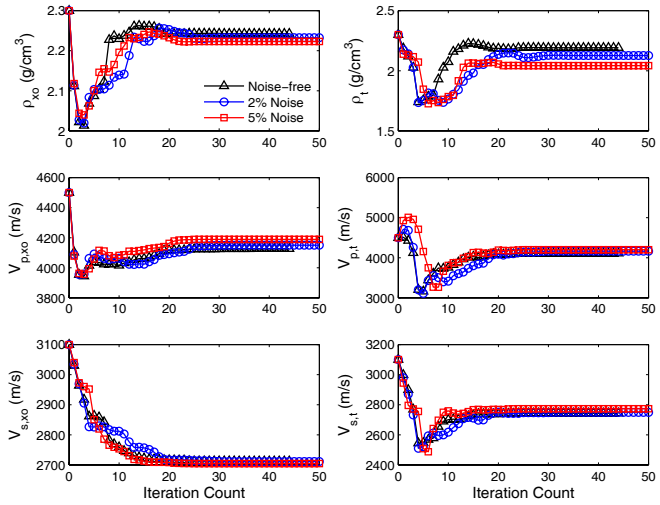

(b)

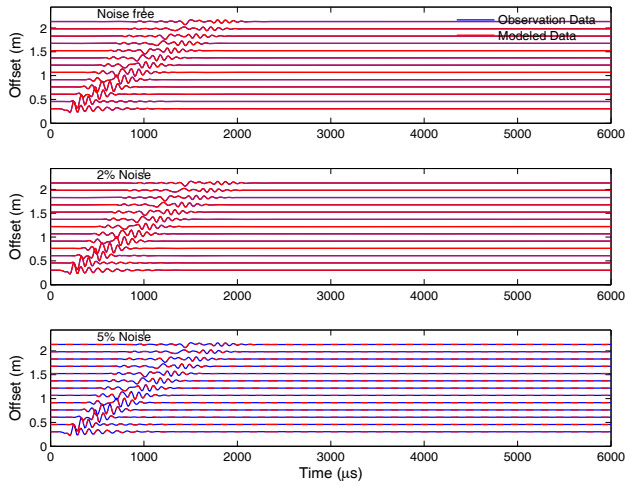

(c)

Figure 6.9. Evolution of data misfit as a function of iteration for the case of array-sonic data acquired in a fast sandstone formation. (a) shows the evolution of the RMS difference between simulated and measured array-sonic data. (b) shows the evolution of the inverted parameters as a function of iteration. (c) shows the misfit between simulated and measured array-sonic data at the end of the minimization.

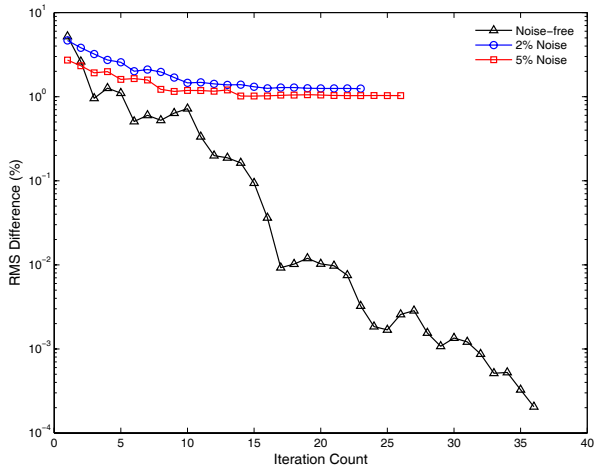

(a)

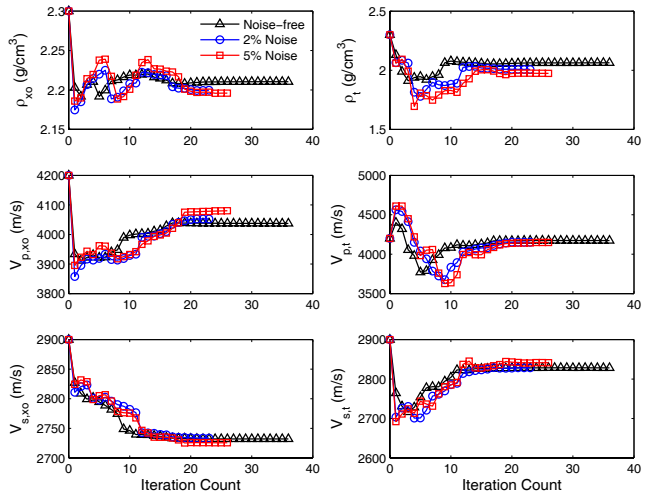

(b)

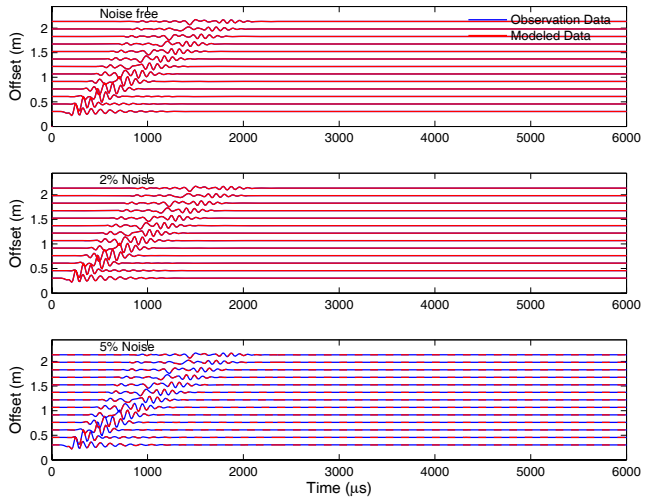

(c)

Figure 6.10. Evolution of data misfit as a function of iteration for the case of array-sonic data acquired in a fast gas-bearing sandstone formation. (a) shows the evolution of the RMS difference between simulated and measured array-sonic data. (b) shows the evolution of the inverted parameters as a function of iteration. (c) shows the misfit between simulated and measured array-sonic data at the end of the minimization.

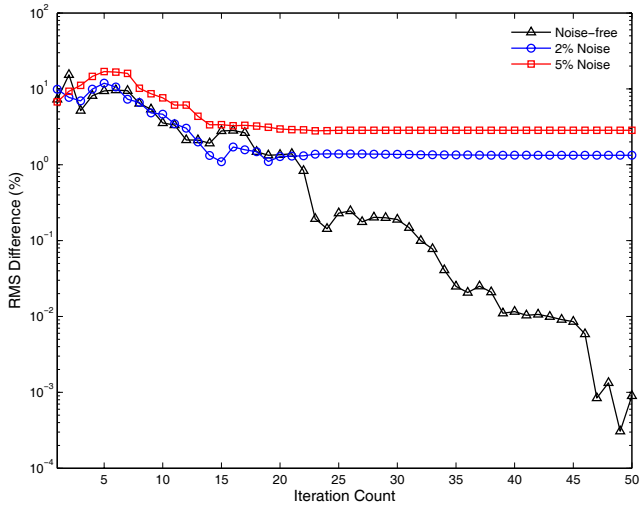

(a)

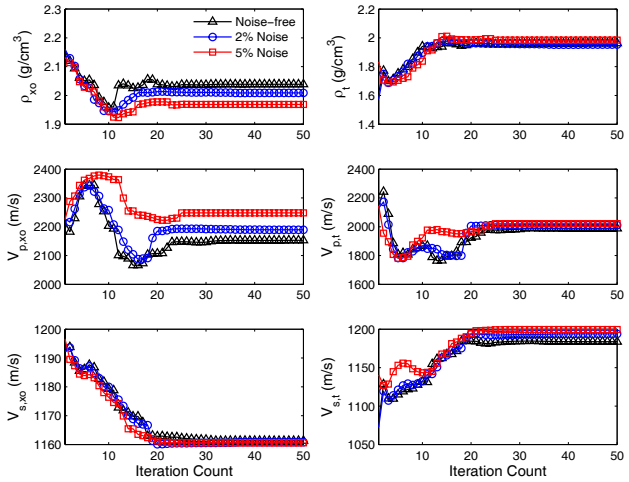

(b)

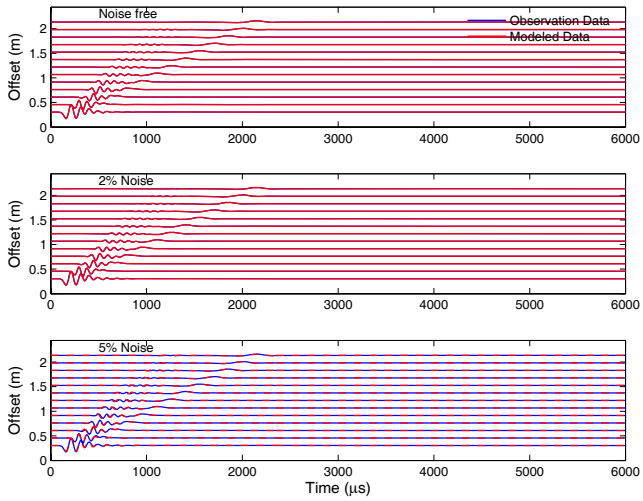

(c)

Figure 6.11. Evolution of data misfit as a function of iteration for the case of array-sonic data acquired in a slow oil-bearing sandstone formation. (a) shows the evolution of the RMS difference between simulated and measured array-sonic data. (b) shows the evolution of the inverted parameters as a function of iteration. (c) shows the misfit between simulated and measured array-sonic data at the end of the minimization.

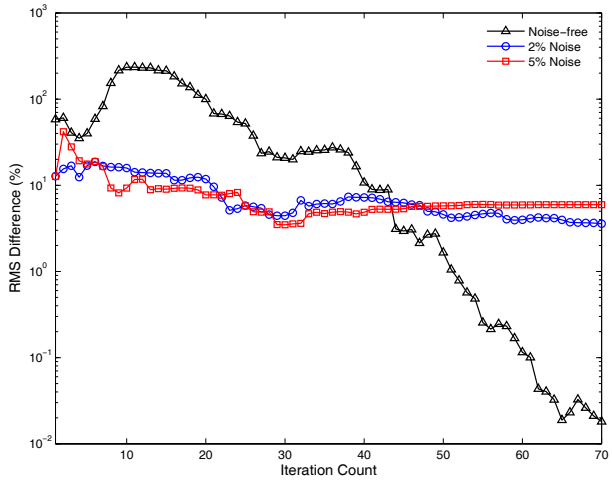

(a)

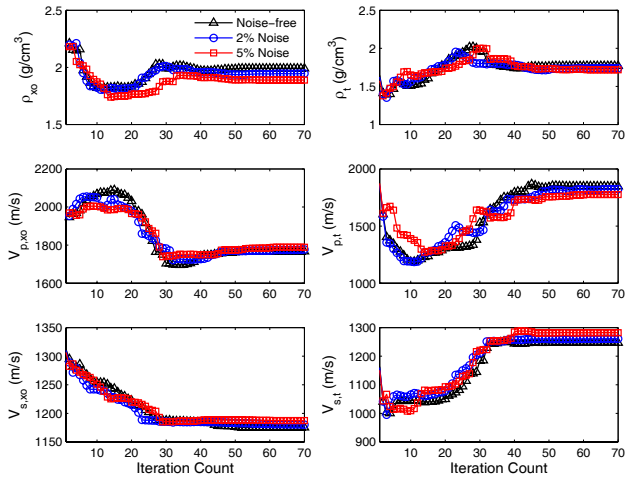

(b)

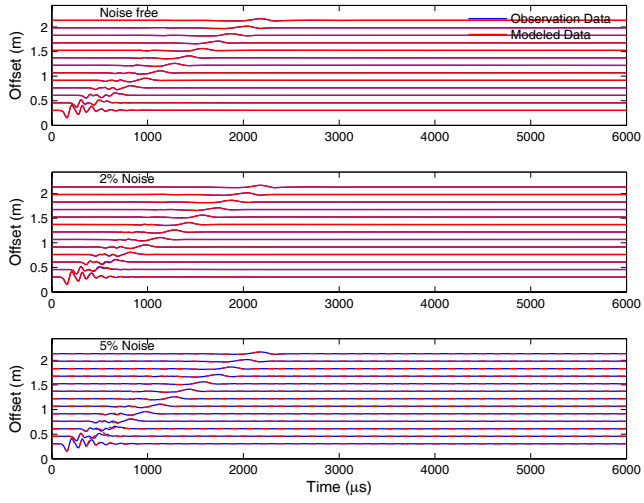

(c)

Figure 6.12. Evolution of data misfit as a function of iteration for the case of array-sonic data acquired in a slow gas-bearing sandstone formation. (a) shows the evolution of the RMS difference between simulated and measured array-sonic data. (b) shows the evolution of the inverted parameters as a function of iteration. (c) shows the misfit between simulated and measured array-sonic data at the end of the minimization.

CHAPTER 7

ESTIMATION OF DRY-ROCK ELASTIC MODULI BASED ON THE SIMULATION OF MUD-FILTRATE INVASION EFFECTS ON BOREHOLE ACOUSTIC LOGS

Reliable estimates of dry-rock elastic properties are critical to accurately interpreting the seismic response of hydrocarbon reservoirs. We describe a new method for estimating elastic moduli of rocks in-situ by simulating the effect of mud-filtrate invasion on resistivity and acoustic logs.

Simulations of mud-filtrate invasion account for the dynamic process of fluid displacement and mixing between mud-filtrate and hydrocarbons. The calculated spatial distributions of electrical resistivity are matched against resistivity logs by adjusting the underlying petrophysical properties. We then perform Biot-Gassmann fluid substitution on the two-dimensional spatial distributions of fluid saturation with initial estimates of dry-bulk (kdry) modulus and shear rigidity (μdry) and a constraint of Poisson's ratio (ν) typical of the formation. This process generates two-dimensional spatial distributions of compressional and shear-wave velocities, and density. Subsequently, sonic waveforms are simulated to calculate shear-wave slowness. Initial estimates of the dry-bulk modulus are progressively adjusted using a modified Gregory-Pickett (1963) solution to Biot's (1956) equation to estimate a shear rigidity that converges on the log value of shear-wave slowness. The constraint on Poisson's ratio is then removed and a refined estimate of the dry-bulk modulus is obtained by both simulating the acoustic log (monopole) and matching the log-derived compressional-wave slowness.

This technique leads to reliable estimates of dry-bulk moduli and shear rigidity that compare well to laboratory core measurements. The resulting dry-rock elastic properties can be used to calculate seismic compressional-wave and shear-wave velocities devoid of mud-filtrate invasion effects for further seismic-driven reservoir-characterization studies.

7.1 INTRODUCTION

As the industry continues to make use of seismic amplitude measurements to construct reservoir flow models and to monitor fluid movement between wells, fluid substitution calculations are becoming more routine and prevalent. Fluid substitution is used to predict elastic

properties of reservoir rocks saturated with one fluid from the elastic properties corresponding to a different state of fluid saturation. The most widely used fluid substitution procedure is based on Gassmann's (1951) equations, which predict velocity changes resulting from variations of pore-fluid saturation. Although Gassmann's equations are widely popular in commercial software packages, a significant limitation which is often overlooked is that the equations inherently depend on *a priori* knowledge of dry-rock bulk modulus and shear rigidity, two parameters that are neither readily available nor derivable from well-log data. Inaccurate estimates of these parameters can lead to unrealistic fluid effects on predicted compressional and shear-wave velocities.

Hamilton (1971) proposed an implicit relation for estimating the dry-bulk modulus. Thomsen (1985) introduced an iterative method based on his Biot-consistent model theory that models the elasticity of rocks at low (seismic) frequency, while Zhu and McMechan (1990) described an explicit, generalized formulation for estimating the bulk modulus directly from Biot's theory.

Wang (2000a) performed experiments comparing the Gassmann predicted results to laboratory data. He observed that predicted Gassmann effects of fluid displacement on seismic velocities only agreed well with laboratory measurements when the rock's skeleton properties used as input to Gassmann's equation were measured at irreducible water saturation. Han and Batzle (2004) pointed out that the matrix modulus k_{matrix} can vary widely depending on mineral composition, distribution of the mineral grains in the matrix, and in-situ conditions. They reported that, in shaly sandstones, the matrix modulus decreases by about 1.7 GPa per 10% increase of clay content. Dvorkin et al. (2007) proposed a method of making Gassmann's equations applicable to shaly sandstone by treating the porous wet shale as part of the solid grain material and then excluding the porosity within the shale from total porosity, whereby the porosity used in fluid substitution was effective porosity. Engelmark (2002) examined the error propagation in Gassmann's modeling and reported that the bulk modulus of the saturated rock, k_{sat}, is most sensitive to errors in k_{dry}, less sensitive to porosity, and least sensitive to errors in the matrix modulus, k_{matrix}, and fluid bulk modulus, k_{fl}, thus highlighting the importance of accurate and reliable estimates of dry-rock elastic moduli for further seismic amplitude interpretation studies.

The method introduced in this chapter aims at providing reliable estimates of dry-rock elastic moduli in-situ based on the simulation of both mud filtrate invasion and sonic waveforms. Spatial fluid distributions obtained from the simulation of mud-filtrate invasion are transformed to compressional-wave (P-wave) and shear-wave (S-wave) velocities based on Biot-Gassmann's fluid substitution equations. These velocity distributions along with the spatial distribution of density define the earth model for the simulation of sonic waveforms. The earth model we arrive at honors both resistivity and borehole sonic measurements. Specifically, the resistivity match validates the in-situ fluid saturation distribution, while the borehole sonic match serves to validate the estimated rock elastic properties.

We apply this method to a synthetic formation model and two field cases. The synthetic case considers a vertical well penetrating a relatively soft rock formation saturated with gas, oil, and water zones in capillary equilibrium. The first field case involves a vertical well penetrating over-pressured tight-gas sands pertaining to the East Texas Bossier formation subject to water-base mud-filtrate invasion, while the second field case considers a vertical well penetrating unconsolidated shaly sands in a deepwater turbidite system subject to oil-base mud-filtrate invasion.

Estimates of elastic properties obtained with the method introduced in this chapter and applied to field measurements are compared to available laboratory core measurements. Comparisons indicate a very good agreement between calculations and measurements.

7.2 METHOD

The method introduced in this chapter begins with the simulation of the process of mud-filtrate invasion into the rock formation in question. This simulation generates spatial distributions of fluid saturation and salt concentration within the invaded formation. Subsequently, we validate the simulated spatial distribution of fluid saturation by simulating the corresponding resistivity logs and comparing them to actual field measurements. Such a strategy ensures that the simulated spatial distribution of water saturation is a reliable description of in-situ fluid distributions. Thus, it is only after successfully reproducing the borehole resistivity logs that we proceed to simulate the corresponding sonic measurements. Matching the resistivity curves is done by varying the petrophysical properties that govern the process of mud-filtrate invasion, such as porosity, relative permeability, initial water saturation, capillary pressure, etc.

Final values of porosity are obtained from this resistivity match. The validated fluid saturation distribution is then transformed to spatial distributions of P-wave velocity, S-wave velocity, and density using Biot-Gassmann's fluid-substitution equations.

Velocities and bulk densities resulting from the fluid substitution procedure depend on the initial estimate of elastic dry-rock properties. These latter properties are then systematically adjusted until the simulated borehole sonic measurements, match the actual field log.

The relationship that describes how elastic moduli and density of the saturated rock relate to the corresponding P-wave velocity, S-wave velocity, and bulk density of a porous medium are given by

$$V_p = \sqrt{\frac{k_{sat} + \frac{4}{3}\mu_{sat}}{\rho_{sat}}}, \text{ and}$$
$$V_s = \sqrt{\frac{\mu_{sat}}{\rho_{sat}}}, \tag{7.2.1}$$

respectively. In the above equations, shear-wave velocity (V_s) depends only on the density (ρ_{sat}) of the saturated rock and the shear rigidity (μ_{sat}), while the compressional-wave velocity (V_p) depends on the bulk modulus (k_{sat}) of the saturated rock as well as on the shear rigidity and density of the saturated rock. Thus, we observe that V_p is dependent on two unknown dry-rock properties, while V_s depends only on one. With this property in mind, we first seek to estimate μ_{sat} and use that value as initial point for the estimation of k_{dry}.

A brief overview of the theory and limitations of Gassmann's fluid substitution procedure is given below.

7.3 GASSMANN'S EQUATION

Gassmann's equation calculates fluid-saturation effects on the bulk modulus of a porous medium using the known bulk moduli of (a) the solid matrix, (b) the frame, and (c) the pore fluid. One form of Gassmann's equation that clearly emphasizes the fluid saturation effects is given by

$$k_{sat} = k_{dry} + \frac{\left(1 - k_{dry}/k_{matrix}\right)^2}{\frac{\phi}{k_{fl}} + \frac{1-\phi}{k_{matrix}} - \frac{k_{dry}}{k_{matrix}^2}}, \tag{7.3.1}$$

where, k_{dry} is the dry-frame bulk modulus, k_{matrix} is the matrix (grain) bulk modulus, k_{fl} is the bulk modulus of the pore fluid, and ϕ is porosity. Because fluids do not support shearing stress, we have

$$\mu_{sat} = \mu_{dry}\,. \tag{7.3.2}$$

The density of the saturated rock is obtained by applying mass conservation principles on the elemental constituents of the rock matrix and pore fluids, namely,

$$\rho_{sat} = \phi\left[S_w\rho_{brine} + \left(1-S_w\right)\rho_{hyc}\right] + \left(1-\phi\right)\rho_{matrix}, \tag{7.3.3}$$

where S_w is water saturation, ρ_{brine} is density of formation water, ρ_{hyc} is density of the hydrocarbon fluid in the pore space, and ρ_{matrix} is density of the rock matrix.

The bulk modulus k_{fl} of a fluid mixture is calculated using Wood's relation (Wood, 1955; White, 1983):

$$k_{fl} = \left(\sum_{i=1}^{n} S_i k_{fi}^{-1}\right)^{-1}, \tag{7.3.4}$$

where n is the number of fluid-phase components, S_i is the volume fraction of the i-th component of fluid phase, and k_{fi} is the bulk modulus of the i-th fluid component.

There are several assumptions involved in the derivation of Gassmann's equations:

(1) The rock is macroscopically homogeneous, isotropic, elastic and mono-mineralic,
(2) Pore spaces are interconnected and in pressure equilibrium,
(3) Pores are filled with a frictionless fluid,
(4) The rock-fluid system under study is closed (undrained), and
(5) The pore fluid does not interact with the solid in a way that would soften or harden the rock frame.

7.4 NUMERICAL SIMULATION OF MUD-FILTRATE INVASION

This step of the interpretation workflow begins with the simulation of the process of mud-filtrate invasion into the formation. Mud-filtrate invasion occurs during drilling due to both overbalanced fluid pressure and mud circulation. The University of Texas's Formation Evaluation Toolbox (FET, Wu et al., 2005), which is a multiphase immiscible flow simulator, is used to calculate the flow rate of mud-filtrate invasion. This finite-difference simulator solves the

partial differential equations and boundary conditions of immiscible cylindrical flow coupled with mudcake growth. In the simulations, both dynamic growth of mudcake and dynamic decrease of mudcake permeability are coupled to formation properties, and this results in a dynamic monotonic decrease of fluid flow into the formation. Details about the numerical simulation of the process of mud-filtrate invasion can be found in Wu et al. (2005). Results from this simulation generate two-dimensional (2D, radial and vertical directions) spatial distributions of fluid saturation and salt concentration.

In the case of water-based mud-filtrate invasion, initial permeability estimates used in the simulation are progressively adjusted according to the method described by Salazar et al. (2005) until the simulated array-induction resistivity curves match the corresponding field measurements.

In the presence of oil-base muds (OBM), the invading mud filtrate is miscible with formation oil, and this mixing causes changes of both fluid density and viscosity, thereby altering the apparent oil-phase mobility in the near-wellbore region. To simulate OBM-filtrate invasion, we consider a simple two-component formulation for the oil phase (OBM and reservoir oil) wherein the components are first-contact miscible. Simulations also consider the presence of irreducible, capillary-bound, and movable water. Additional details about this algorithm can be found in Malik et al. (2007). All mud-filtrate simulations described in this chapter assume azimuthal symmetry in formation properties with respect to the axis of a vertical borehole.

The FET was used to calculate the flow rate of OBM-filtrate invasion based on mudcake, rock, and fluid properties (Wu et al., 2005). Multiple simulations were performed with varying mudcake and petrophysical properties such as relative permeability, wettability, movable water saturation, etc. to secure a good match between field and simulated resistivity measurements, as described by Malik et al. (2007).

Array-induction resistivity measurements are simulated from the spatial distribution of electrical resistivity, in turn calculated from the 2D spatial distributions of water saturation and salt concentration via Archie's (1942) equation.

7.5 2D SPATIAL DISTRIBUTIONS OF DENSITY, P- AND S-WAVE VELOCITIES

Once we calculate the 2D spatial distribution of fluid saturation, we perform a fluid substitution procedure using a modified Gregory-Pickett (1984) solution of Biot's equation. This

technique enables one to calculate an initial value of the dry-bulk modulus and to impose a fixed constraint on Poisson's ratio specific to the rock under consideration.

The philosophy behind Gregory-Pickett's (1984) solution of Biot's equations is as follows:

(1) With an initial velocity estimate at a given petrophysical state (porosity and saturation), Biot's (1956) equation can be inverted to yield both the bulk modulus and the shear rigidity of the dry rock,

(2) As long as porosity remains the same, these dry elastic parameters (the dry-bulk modulus and the shear rigidity) remain unchanged even if water saturation varies,

(3) However, if the porosity is changed then the dry rock exhibits new elastic parameters that are updated using a variation of Pickett's equation for estimating the dry-rock modulus (Wyman, 1982).

For the purposes of this chapter, we modify the above procedure slightly to begin with an estimate of the dry-bulk modulus, invert the compressional-wave velocity (V_p), and subsequently calculate the shear-wave velocity (V_s). This procedure is carried out radially for varying fluid saturations (porosity is assumed constant in the radial direction) to obtain spatial distributions of P- and S-wave velocities, and densities which are used as input for sonic waveform simulation. The Appendix E provides a step-by-step summary of the above procedure.

7.6 NUMERICAL SIMULATION OF BOREHOLE SONIC MEASUREMENTS

With the 2D spatial distributions of V_p, V_s, and ρ, sonic waveform simulations were carried out using the University of Texas at Austin's Borehole Sonic Modeling Toolbox. This toolbox simulates full-wave time-domain sonic measurements acquired in axial-symmetric media. It assumes that the vertical well penetrates horizontal layers that consist of multiple radial zones (including a borehole) similar to those of mud-filtrate invaded formations. Numerical simulation is performed with a finite-difference discretization scheme in space and time of the velocity-stress wave equation in cylindrical coordinates (Chi et al., 2006). We simulate Schlumberger's Dipole Shear Sonic Imager (DSI[2]) measurements, which consist of an array of eight receivers spaced 6 in. apart, and model waveforms excited by both monopole and lower-dipole transmitters. First, we simulate sonic waveforms assuming radial variations of V_p, V_s, and ρ. This procedure requires an average of saturation values vertically along the length of the

[2] Mark of Schlumberger

receiver array before calculating the radial profile of sonic velocities and densities via fluid substitution. The value assigned to each depth point is taken to be at the geometric center of the receiver array. Simulated sonic waveforms are processed with Slowness-Time Coherence (STC) and Dispersion analysis to extract the corresponding shear-wave slowness/velocity. Dispersion analysis in the frequency domain is used to ensure that the extracted S-wave velocity/slowness is at the asymptoting value of the flexural wave velocity/slowness which approximates the S-wave velocity/slowness for dipole excitation. If the extracted S-wave velocity/slowness does not match the field measurements, then the estimate of k_{dry} is adjusted, and once again we generate spatial distributions of V_p, V_s, and ρ from fluid substitution, and simulate new sonic waveforms. This process is repeated until we converge to a value of k_{dry} from which the simulated S-wave velocity/slowness reproduces the measured S-wave velocity/slowness. As we initially imposed a constraint on Poisson's ratio, we also obtain a corresponding estimate of μ_{dry}. This calculated value of shear rigidity (μ_{dry}) is fixed and taken to be the estimate for the formation at the logging depth under consideration.

The constraint on Poisson's ratio is then removed and we perform Gassmann's fluid substitution where the only unknown is now the dry-bulk modulus (k_{dry}). As indicated earlier, such a procedure generates spatial distributions of velocities and density for which we perform the simulation of sonic waveforms. At this point, the result of the simulation is processed to extract the P-wave velocity/slowness. If the extracted P-wave velocity/slowness does not match the field measurements, then the estimate of k_{dry} is adjusted, and, once again, we construct spatial distributions of V_p, V_s, and ρ, and simulate the corresponding sonic waveforms to extract a new P-wave velocity/slowness. The process is repeated until we converge to a final estimate of k_{dry} for which the simulated P-wave velocity/slowness reproduces the measured P-wave velocity/slowness.

The above procedure yields final estimates of dry-bulk modulus (k_{dry}), shear rigidity (μ_{dry}), and Poisson's ratio (ν) at every depth point of interest.

7.7 CASE STUDIES

We apply the above estimation method to three different cases. The first case considers a synthetic clastic rock formation, while the remaining two cases consider field data sets where core laboratory measurements are available.

CASE NO. 7.7.1: CLEAN SAND INTERVAL WITH GAS, OIL, AND WATER ZONES IN CAPILLARY EQUILIBRIUM, INVADED WITH WATER-BASE MUD.

We consider a clean sandstone interval that consists of four distinct petrophysical layers of equal thicknesses. The top-most layer (Layer 1) is a high porosity, gas saturated layer, while Layers 2 and 3 are saturated with oil, with Layer 3 being of higher porosity than Layer 2. A water-oil contact marks the beginning of the low-porosity bottom layer (Layer 4). This model was constructed using the University of Texas at Austin's Formation Evaluation Toolbox (FET). Table 7.1 summarizes the formation properties for this interval.

We carry out the estimation method on this synthetic formation to ascertain the accuracy and reliability of the estimation method with synthetic data sets devoid of noise, in a clean mono-mineralic interval, and with complete knowledge of formation properties. The objective is to quantify the accuracy of the method over regions of varying porosity and differing pore fluid saturation (gas, oil, and water), with no external interference on the quality of the borehole measurements.

Simulation of the process of water-base mud-filtrate invasion is carried out with an initial reservoir pressure of 5000 psi, with both water saturation and pressure in capillary equilibrium. Initial water saturation in each layer decreases away from the water-oil contact, and the layers are in hydraulic communication with one another thus permitting cross flow across them, while permeability is anisotropic. Table 7.2 summarizes the mudcake, fluid, and formation properties, as well as the numerical parameters used in the simulation of mud-filtrate invasion.

Figure 7.2 shows the 2D spatial distributions of water saturation, salt concentration, and electrical resistivity resulting from the simulation of mud-filtrate invasion into the synthetic 4-layer formation, 2 days after the onset of invasion. Figure 7.3 shows the corresponding spatial distributions of V_p, V_s, and ρ calculated from fluid substitution. Based on the spatial distributions shown in Figure 7.2, we proceed to simulate borehole AIT[3] resistivity measurements using the FET. To demonstrate the reliability of the method, we attempt to reproduce these resistivity logs by assuming no knowledge of layer properties and matching the resistivity logs by estimating the underlying layer petrophysical properties and simulating the process of mud-filtrate invasion. Figure 7.4 displays the final match between simulations and measurements.

[3] Mark of Schlumberger

This good match of measured resistivity curves validates the spatial distribution of water saturation. We proceed to carry out fluid substitution to generate synthetic field borehole acoustic logs based on the original water saturation distribution used in the simulation of synthetic resistivity curves. Fluid substitution is performed using the given dry-bulk and shear moduli of each layer (Table 7.1), whereby we generate spatial distributions of V_p, V_s, and ρ. We then simulate the corresponding borehole sonic waveforms at the center of each layer, to arrive at synthetic borehole sonic measurements (Figure 7.5). Sonic simulations are performed assuming the Schlumberger Dipole Shear Imager (DSI) tool. The subsurface model for this example was designed with layers thick enough to ensure that the length of the sensor array is shorter than the thickness of the bed. In so doing, we ensure that both the source and the receiver array are in the same bed when we simulate the log reading at the center of the bed, thereby eliminating the need to consider the influence of shoulder beds.

We now proceed to match synthetic logs with the simulated borehole acoustic measurements generated using estimates of dry-bulk elastic modulus. To that end, we first seek to converge to the value of S-wave velocity/slowness.

Using the modified Gregory-Pickett solution of Biot's equation, with an initial estimate of k_{dry} = 6 GPa, and averaging the saturation profile vertically over the length of the receiver array, we obtain radial distributions of V_p, V_s, and ρ at every logging point of interest. Figure 7.6 shows these radial distributions at a depth of 3972.5 ft, while Figure 7.7 shows the simulated sonic waveforms with an improved estimate of k_{dry}= 10.25 GPa. From the Slowness-Time coherence results, a slowness value of 151 μs/ft is extracted as the S-wave slowness (Figure 7.8). This value of slowness matches the synthetic field logs, whereupon we fix the corresponding shear rigidity value (μ_{dry} = 10.43 GPa), remove the constraint on Poisson's ratio and perform Gassmann's fluid substitution again, except that this time the only unknown property is k_{dry}. After multiple iterations, we finally converge to an improved value of k_{dry} = 9.5 GPa that matches the field P-wave slowness of 91 μs/ft. Table 7.3 summarizes the final dry-rock properties together with the field and simulated slownesses.

CASE NO. 7.7.2: UNCONSOLIDATED SHALY SAND INVADED WITH OIL-BASE MUD.

We consider a well located in the deepwater Gulf of Mexico, whose sedimentary structure has rippled stratification, clay laminations, and large sand intervals with moderate to good grain sorting (Malik et al., 2007). Porosity values range between 20% and 35%, and permeability between 10 md and 2500 md. Various clay minerals present in the rock matrix include illite/smectite, illite/mica, and kaolinite and chlorite in minute amounts.

For Case No. 7.7.2, we utilize the estimation method on actual data sets obtained in shaly sands. Here, the quality of acoustic log measurements is not very good and borehole conditions vary significantly over the interval. These conditions present an adverse real-world situation in which to test the reliability of our estimation method.

Our analysis here will be on a section that is partially oil-saturated with moveable water. Full petrophysical assessment of this interval can be found in Malik et al. (2007).

Simulation of oil-base mud-filtrate invasion was carried out with a compositional simulator to calculate the spatial distribution of water saturation due to invasion. A simple binary formulation to describe both mud-filtrate and formation oil was used where the components of OBM-filtrate and formation oil were lumped into two pseudo-components. Figure 7.9 shows the spatial distributions of water saturation and electrical resistivity calculated 3 days after the onset of invasion. Due to the shaliness of the sands, Waxman-Smits' (1968) formulation is used to convert the spatial distribution of water saturation to electrical resistivity. Figure 7.10 shows the corresponding spatial distribution of V_p, V_s, and ρ calculated from fluid substitution with an initial estimate of k_{dry} = 4 GPa, while Figure 7.11 shows the radial distributions obtained by averaging the water saturation and shale concentration values vertically over the length of the receiver array. Borehole AIT resistivity measurements were simulated based on the water saturation distribution obtained from the simulation of mud-filtrate invasion using the FET. Matching field and simulated resistivity logs was achieved by modifying the dominant petrophysical and fluid properties on the simulation of mud-filtrate invasion. Details of this procedure can be found in the paper by Malik et al. (2007). Figure 7.12 compares field and simulated array-induction resistivity curves, indicating a good-quality match.

Due to presence of shale laminae in this depth interval, the fluid substitution procedure is modified by adopting the method outlined by Dvorkin et al. (2007). Volumetric concentration of

shale is computed across the depth interval, together with assessment of shale porosity. Subsequently, we exclude the porosity within the shale so that the porosity used in Gassmann's equations is effective porosity. As fluids can only be substituted in the effective pore space, we also calculate effective water and hydrocarbon saturation, respectively. It is also necessary to calculate an effective fluid bulk modulus since the mixing of formation water and hydrocarbon is confined to the effective pore space. The dry-frame modulus of the rock matrix is modified to account for the new composite matrix of quartz and wet clay, which is achieved by taking the arithmetic average of Voight and Reuss' (1952) bounds. These changes allow us to arrive at an initial estimate of dry-effective bulk modulus, which is subsequently used in the fluid substitution procedure.

Figure 7.13 shows the resulting sonic waveforms after dipole simulation at a depth of XX252 ft with an initial estimate of k_{dry}= 4 GPa. This latter estimate was subsequently adjusted to a final value of k_{dry} = 3.3 GPa, and μ_{dry} = 3.36 GPa that led to a S-wave slowness that matched the log value of 252.02 μs/ft, following STC and dispersion analysis. Table 7.10 describes the parameters assumed in the simulation of sonic waveforms for all three cases.

After fixing the value of μ_{dry} and removing the constraint on Poisson's ratio, we perform fluid substitution to obtain an improved estimate of k_{dry} = 4.30 GPa that entails a good match between field and simulated P-wave slownesses. Figure 7.14 shows the STC plot used to extract this simulated P-wave slowness. The above procedure is applied at several logging depths throughout the interval. Table 7.5 summarizes the final dry-rock properties.

CASE NO. 7.7.3: OVER-PRESSURED TIGHT-GAS SAND FORMATION INVADED WITH WATER-BASE MUD.

This North Louisiana tight-gas sand formation consists of very fine- to fine-grained sandstone, shale, and some sandy, fossiliferous oolitic limestone (Finley, 1984). Rock units present in this formation are texturally mature quartz arenites and sub-arkose sands (McGowen and Harris, 1984).

Geological cross-sections throughout the formation evidence a thick, sand-dominated wedge of sediments mainly consisting of braided stream deposits. This formation provides a different petrophysical environment to quantify. Specifically, the nature of the formation leads to

shallow radial lengths of invasion. In addition, presence of in-situ gas warrants another fluid substitution variable for which to test the method.

Petrophysical analysis of the well-log data was documented by Salazar et al. (2006). Figure 7.15 shows the 2D spatial distributions of water saturation, salt concentration, and resistivity after 2 days of invasion across the zone of interest, while Figure 7.16 shows the corresponding spatial distributions of V_p, V_s, and ρ calculated from fluid substitution with an initial estimate of k_{dry} = 21.5 GPa. Figure 7.18 compares simulated Schlumberger resistivity logs (AIT) to measured Halliburton High-Resolution Induction (HRI[4]) resistivity logs. At present, we do not have the capability to simulate HRI logs: Hence, we do not expect an accurate match of resistivity logs. However, for the purposes of this chapter we believe that simulations agree well with measurements and hence satisfactorily reproduce the invaded and virgin radial zones. Figure 7.17 shows the radial distributions of V_p, V_s, and ρ obtained by averaging the saturation values vertically over the length of the receiver array. These plots indicate a radial length of invasion of approximately 1.5 ft. Figure 7.19 shows the simulated sonic waveforms for dipole excitation at this depth with an initial guess of k_{dry} = 21.5 GPa. This initial estimate was subsequently refined to a value of k_{dry} = 29 GPa, and μ_{dry} = 29.5179 GPa to obtain a S-wave slowness that matches the log value of 93.15 μs/ft. Figure 7.20 shows the corresponding slowness-time coherence plot for these estimates. Dispersion analysis was performed to ensure that the flexural wave velocity/slowness measured at the logging frequency of 4 kHz was close enough to its low-frequency asymptotic value (Figure 7.21). Table 7.10 specifies the properties of the sonic tool assumed in the simulations. Due to the hardness of this formation, dipole simulations were used to extract the shear-wave velocity/slowness, while monopole simulations were used to extract the compressional-wave velocity/slowness.

Next, by removing the constraint on Poisson's ratio and fixing the value of μ_{dry}, we perform fluid substitution with the only unknown being k_{dry}. After multiple iterations, we converge at an improved estimate of k_{dry} = 26 GPa that leads to a simulated P-wave slowness of 62.52 μs/ft, that in turn matches the simulated P-wave slownesses with the log value. Figure 7.22 compares the final estimated dry-bulk modulus to laboratory measurements performed on core samples. At depths close to those of the cored samples, we observe that that the estimated

[4] Mark of Halliburton

moduli, are close to laboratory measurements. The k_{dry} estimates lie between laboratory measurements performed at 1000 psi, and 3000 psi of confining pressure.

7.8 DISCUSSION AND CONCLUSIONS

We introduced and successfully implemented a new method to estimate the dry-bulk modulus and shear rigidity of reservoir rocks in-situ. The method consists of simulating the process of mud-filtrate invasion and the corresponding effect on borehole acoustic and resistivity measurements. From the results of Case No. 7.7.1, we observe that the percent error of the estimates ranges from 0.12 - 6.25%. The gas-saturated zone accounted for the largest error in the estimates of both k_{dry} and μ_{dry}, while the lowest error was obtained in the high-porosity oil-saturated zone where the resistivity match was good.

In Case No. 7.7.2, the estimation method was applied to an unconsolidated sand interval with shale laminae in the presence of OBM-filtrate invasion. Table 7.5 lists the final estimates obtained in this interval, while Table 7.6 describes the results from multi-stage compressional tests performed on core samples. By comparing the values of Poisson's ratio, we observe that, at depths where the measurements are completely contained in the sand interval, the estimated Poisson's ratio compares well to laboratory results obtained from a similar clean sand interval at low values of confining pressure. It is important to note that even though we accounted for presence of shale in Biot-Gassmann's fluid substitution, dry-rock moduli extracted in pure shale zones are not guaranteed to be indicative of lithology. This behavior is probably due to the fact that the reliability of our estimates depends on the integrity of borehole acoustic measurements. Borehole conditions in the shale intervals were not good, whereupon the logs measured in those zones remain questionable. In general, the reliability of estimates of elastic moduli is highly dependent on the accuracy and reliability of the measured acoustic logs.

In Case No. 7.7.3, we considered a clean tight-gas sand formation invaded with water-base mud. Table 7.8 describes the final dry-rock elastic properties estimated in this well, while Table 7.9 summarizes the corresponding laboratory measurements at similar depths where rock core samples were retrieved. The value of k_b reported in Table 7.8 is calculated from the reported values of Young's modulus (E) and Poisson's ratio (ν) obtained from core compressional tests. At approximately XX024 ft, the estimate of k_{dry} is in good agreement with the corresponding laboratory measurement (k_b) performed at a confining pressure of 3000 psi, but Poisson's ratio

does not indicate a good agreement. Because we do not know under what state of fluid saturation the tri-axial test was carried out, in addition to estimating the dry-rock bulk modulus, we computed the bulk modulus at 100% water saturation, and compared both values to available core measurements (Figure 7.22). By comparing the estimates of elastic moduli to core measurements, we observe that the estimates of k_{dry} are closer to laboratory measurements than the estimates of μ_{dry}.

Based on estimation results from the three cases discussed here, we conclude that our iterative method of estimating dry-bulk elastic moduli yields reliable results in field cases as suggested by the comparison to core measurements. We observe better accuracy in the estimates of k_{dry}, than in the estimates of μ_{dry}. The accuracy of the method used to estimate μ_{dry} seems to decrease in the presence of gas. This anomalous behavior requires further investigation and quantification.

Nomenclature

k_{dry} = Dry-frame bulk modulus *[GPa]*

k_{matrix} = Matrix (grain) bulk modulus *[GPa]*

k_{fl} = Fluid bulk modulus *[GPa]*

k_{sat} = Bulk modulus of fluid-saturated rock *[GPa]*

k_{fi} = Bulk modulus of *i*-th fluid component *[GPa]*

V_p = Compressional (P-wave) velocity *[ft/sec]*

V_s = Shear (S-wave) velocity *[ft/sec]*

S_w = Water saturation *[fraction]*

S_i = Volume fraction of *i*-th component *[fraction]*

r_w = Wellbore radius *[ft]*

r_e = External reservoir radius *[ft]*

nr = Number of radial nodes

nz = Number of vertical nodes

Greek Symbols

μ_{dry} = Shear rigidity of dry rock *[GPa]*

μ_{sat} = Shear rigidity of fluid saturated rock *[GPa]*

ρ_{sat} = Bulk density of fluid-saturated rock *[g/cc]*

ρ_{brine} = Density of formation water *[g/cc]*

ρ_{hyc} = Density of hydrocarbon fluids *[g/cc]*

ρ_{matrix} = Density of rock matrix *[g/cc]*

v = Poisson's ratio *[-]*

ϕ = Porosity *[fraction]*

Δt_p = P-wave slowness *[μs/ft]*

Δt_s = S-wave slowness *[μs/ft]*

Acronyms

FET = Formation Evaluation Toolbox

STC = Slowness-Time Coherence

OBM = Oil-Base Mud

AIT = Array-Induction Tool

HRI = High-Resolution Induction Tool

Table 7.1: Summary of layer petrophysical and elastic properties assumed in the synthetic model (Case No. 1). *(K_r: radial permeability; K_v: vertical permeability; K_{dry}: dry-bulk modulus; μ_{dry}: shear rigidity)*

Layer No.	Porosity (ϕ)	K_r (md)	K_v (md)	k_{dry} (GPa)	μ_{dry} (GPa)	Thickness (ft)
1	0.365	200	200	8.00	7.50	15
2	0.12	60	20	9.68	10.18	15
3	0.29	350	300	6.40	7.32	15
4	0.18	180	100	7.25	7.14	15

Table 7.2: Summary of formation, fluid, mudcake, and numerical parameters assumed in the simulation of mud-filtrate invasion for the synthetic model (Case No. 7.7.1).

Formation and Fluid Properties		
Variable	**Units**	**Value**
Oil density	g/cc	0.850
Water density	g/cc	1.00
Gas density	g/cc	0.156
Water viscosity	cp	1
Oil viscosity	cp	3
Bulk modulus of water	GPa	2.41
Bulk modulus of oil	GPa	0.482
Bulk modulus of gas	GPa	0.0383
Initial reservoir formation pressure	psi	5000
Maximum invasion time	days	2
Mudcake Parameters		
Variable	**Units**	**Value**
Mudcake reference permeability	md	2.071
Mudcake reference porosity	fraction	0.932
Mudcake thickness	inches	0.392
Mud overbalance pressure	psi	500
Grid Parameters		
Variable	**Units**	**Value**
Wellbore radius (r_w)	ft	0.354
External radius (r_e)	ft	2000
Number of radial nodes *(nr)*	-	61
Number of vertical nodes *(nz)*	-	30

Table 7.3: Summary of calculated sonic-wave slownesses and final dry-rock elastic moduli for the synthetic model (Case No. 7.7.1.) *(Δt_p: P-wave slowness; Δt_s: S-wave slowness; K_{dry}: dry-bulk modulus; μ_{dry}: shear rigidity)*

Sonic wave slownesses				
Layer No.	**Δt_p** *(μs/ft)*	**Δt_s** *(μs/ft)*	**Δt_p** *(μs/ft)*	**Δt_s** *(μs/ft)*
	Field data		***Simulated data***	
1	98	154	98.6	154.59
2	91	151	90.76	150.79
3	104	168	104.23	167.9
4	101	178	101.8	179.1
Calculated dry-rock elastic properties				
Layer No.	**k_{dry}** *(GPa)*	**μ_{dry}** *(GPa)*	**k_{dry}** *(% error)*	**μ_{dry}** *(% error)*
1	8.5	7.73	6.25	3.14
2	9.5	10.43	1.85	2.48
3	6.35	7.32	0.78	0.12
4	7.25	6.92	0	3.06

Table 7.4: Summary of fluid, formation, and rock properties assumed in both Biot-Gassmann's fluid substitution and the simulation of oil-base mud-filtrate invasion (Case No. 7.7.2).

Formation and Fluid Properties		
Variable	**Units**	**Value**
Water density	g/cc	0.999
Bulk modulus of water	GPa	2.41
Oil density	g/cc	0.753
OBM-filtrate density	g/cc	0.770
OBM–filtrate viscosity	cp	1.50
Bulk modulus of oil	GPa	0.482
Quartz density	g/cc	2.65
Bulk modulus of quartz matrix	GPa	36
Bulk modulus of shale matrix	GPa	25
Shale density	g/cc	2.37
Shale porosity	fraction	0.15
Residual water saturation	fraction	0.07
Residual oil saturation	fraction	0.10
Initial reservoir formation pressure	psi	7,750
Maximum invasion flow rate	$ft^3/d/ft$	0.027
Maximum invasion time	days	3
Mudcake Parameters		
Variable	**Units**	**Value**
Mudcake thickness	inches	0.400
Mud hydrostatic pressure	psi	8,000
Grid parameters		
Variable	**Units**	**Value**
Wellbore radius *(r_w)*	ft	0.49
External radius *(r_e)*	ft	1,000
Reservoir thickness	ft	30
Number of radial nodes *(nr)*	-	50
Number of vertical nodes *(nz)*	-	60

Table 7.5: Summary of final estimates of dry-rock elastic properties for Case No. 7.7.2**.** *(k_{dry}: dry-bulk modulus; μ_{dry}: shear rigidity)*

Depth	Lithology	k_{dry} *(GPa)*	μ_{dry} *(GPa)*	ν
XX252	*Shale*	*4.30*	*3.36*	*0.19*
XX256	Sandstone	3.74	2.37	0.24
XX258	Sandstone	4.10	2.91	0.21
XX260	Sandstone	3.90	2.97	0.20
XX262	Sandstone	4.05	2.57	0.24
XX265	Sandstone	3.90	2.55	0.23
XX270	*Shale*	*4.00*	*2.69*	*0.22*
XX272	*Shale*	*3.55*	*2.93*	*0.18*
XX274	Sandstone	3.30	2.44	0.20
XX276	Sandstone	3.60	2.22	0.24
XX278	*Shale*	*4.55*	*2.50*	*0.27*
XX280	*Shale*	*3.00*	*3.00*	*0.12*
XX285	Sandstone	3.46	2.46	0.21
XX290	Sandstone	4.52	2.11	0.30
XX292	Sandstone	6.80	1.89	0.37

Table 7.6: Summary of tri-axial compressional laboratory measurements performed on available core samples for Case No. 7.7.2. *(E: Young's modulus; v: Poisson's ratio)*

Sample Number (confining pressure)	Depth (ft)	E ($x10^3$ psi)	ν
S1-4 (50 psi)	11927.25	26.3	0.28
S1-6 (686 psi)	11927.25	68.1	0.08
S1-3 (1372 psi)	11927.25	209	0.18
S2-12 (50 psi)	11934.9	23.4	0.20
S2-7 (686 psi)	11934.9	115	0.21
S2-4 (1372 psi)	11934.9	174	0.37
S3-4 (50 psi)	11962.7	12.2	0.28
S3-3 (686 psi)	11962.7	112	0.21
S3-5 (1372 psi)	11962.7	141	0.15

Table 7.7: Summary of formation, fluid, mudcake, and numerical parameters assumed in the simulation of water-base mud-filtrate invasion (Case No. 7.7.3).

Formation and Fluid Properties		
Variable	**Units**	**Value**
Water density	g/cc	0.999
Bulk modulus of water	GPa	2.41
Oil density	g/cc	0.753
Bulk modulus of oil	GPa	0.482
Gas density	g/cc	0.001
Quartz density	g/cc	2.65
Bulk modulus of gas	GPa	0.0383
Bulk modulus of quartz matrix	GPa	36
Irreducible water saturation	fraction	0.06
Initial reservoir formation pressure	psi	6465
Mudcake Parameters		
Variable	**Units**	**Value**
Mudcake reference permeability	md	0.031
Mudcake reference porosity	fraction	0.932
Mudcake thickness	inches	0.392
Mud overbalance pressure	psi	2935
Grid parameters		
Variable	**Units**	**Value**
Wellbore radius *(r_w)*	ft	0.254
External radius *(r_e)*	ft	2000
Number of radial nodes *(nr)*	-	61
Number of vertical nodes *(nz)*	-	129

Table 7.8: Summary of final estimates of dry-rock elastic properties for the formation under consideration for Case No. 7.7.3. *(K_{dry}: dry-bulk modulus; μ_{dry}: shear rigidity; v: Poisson's ratio)*

Depth	**k_{dry}** *(GPa)*	**μ_{dry}** *(GPa)*	**v**
XX007	26.00	22.08	0.17
XX009	24.20	18.12	0.20
XX012	29.00	33.59	0.08
XX016	24.00	26.16	0.10
XX024	20.00	22.40	0.10
XX027	29.20	28.19	0.13
XX030	24.50	21.88	0.16
XX032	21.00	23.41	0.09
XX037	26.00	29.52	0.09
XX056	25.50	29.82	0.08

Table 7.9: Summary of multi-stage tri-axial compressional laboratory measurements performed on available core samples for Case No. 7.7.3. *(σ_c: confining stress; σ_f: failure stress; E: Young's modulus; K_{dry}: dry-bulk modulus; v: Poisson's ratio)*

Sample No.	σ_c (psi)	σ_f (kpsi)	E (Mpsi)	v	k_b (GPa)
XX025.35	1000	15.84	4.961	0.171	17.328
	2000	22.00	5.954	0.183	21.551
	3000	27.80	5.937	0.173	20.863
XX041.35	1000	16.303	8.408	0.111	24.838
	2000	21.55	9.485	0.212	37.845
	3000	27	10.062	0.224	41.893
XX055.4	1000	24.4	6.834	0.123	20.831
	2000	32.05	7.57	0.179	27.099
	3000	38.34	7.605	0.192	28.374

Table 7.10: Summary of 1D sonic tool properties assumed in the simulation of borehole sonic waveforms for all case studies considered in this chapter.

Property	Monopole	Dipole
Center Frequency (kHz)	11	4
Bandwidth (kHz)	22	8
Maximum Amplitude	1	1
Pulse Length (ms)	0.5	0.35
Wavelet	Ricker	Ricker

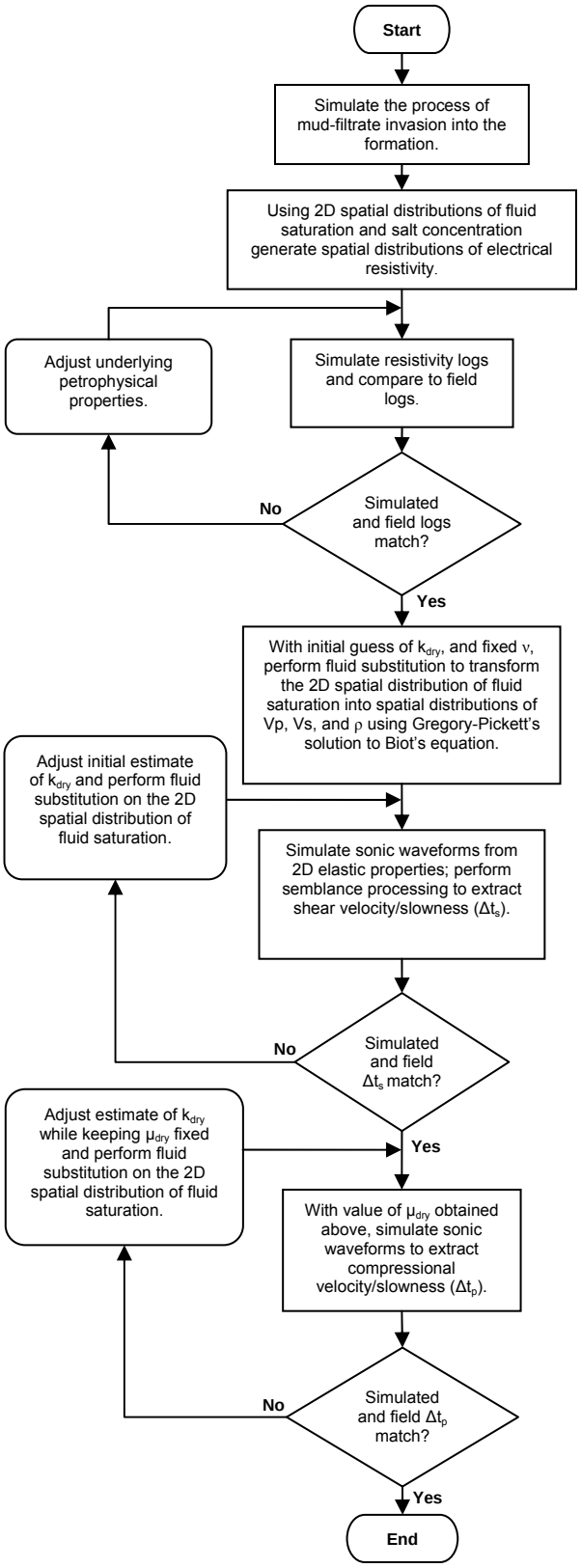

Figure 7.1: Flow chart describing the procedure used in this chapter to estimate the in-situ dry-bulk elastic moduli of rock formations. *(Definitions of variables are provided in the Nomenclature section)*

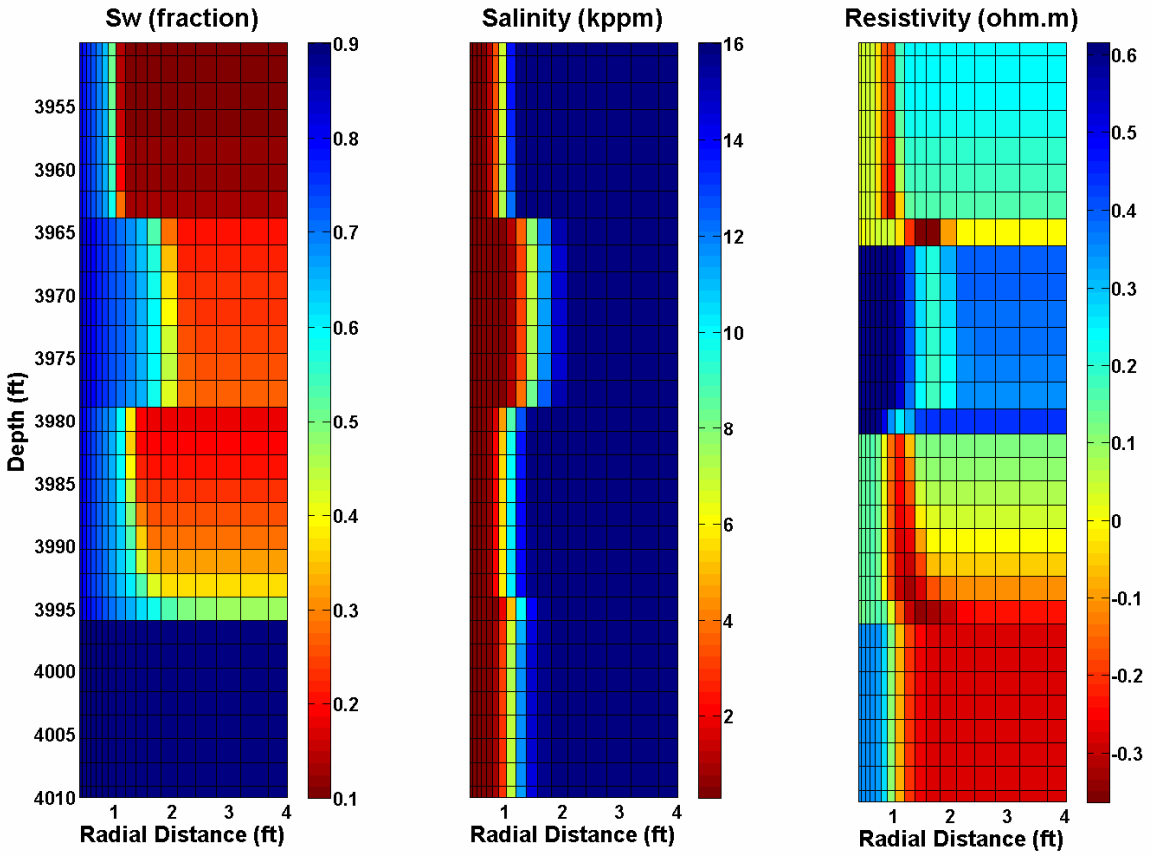

Figure 7.2: Spatial distributions (radial and vertical directions) of water saturation (left panel), salt concentration (center panel), and electrical resistivity (right panel) across the zone of interest in the synthetic unconsolidated sand of Case No. 7.7.1.

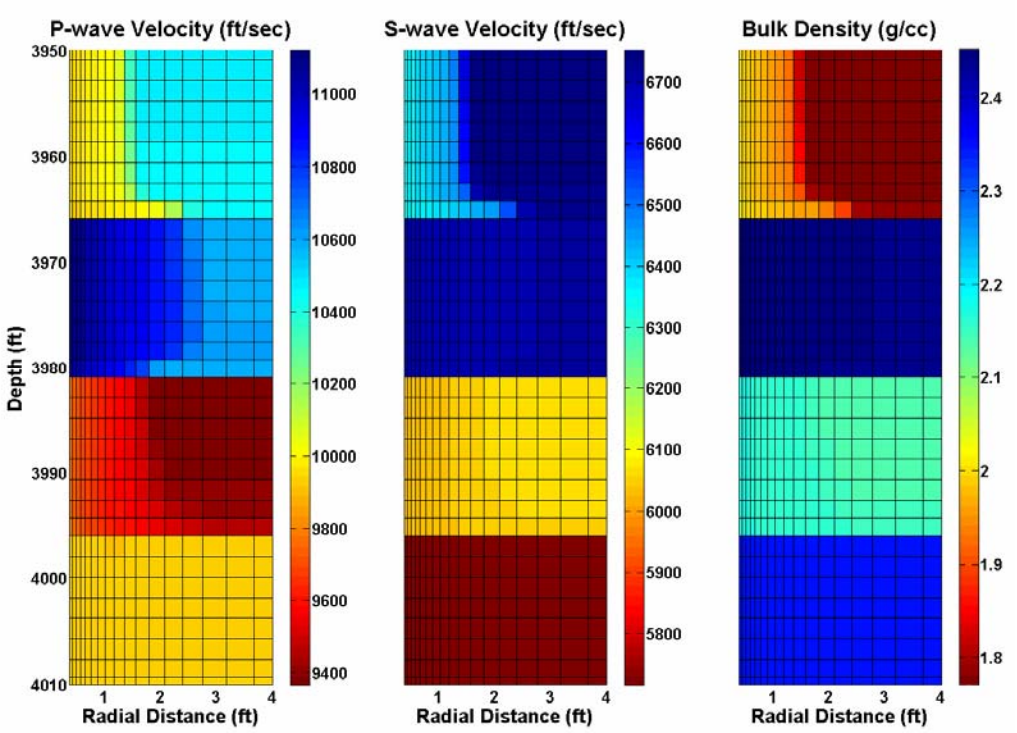

Figure 7.3: Spatial distributions (radial and vertical direction) of P-wave velocity (left panel), S-wave velocity (center panel), and bulk density (right panel) obtained from Biot-Gassmann's fluid substitution applied to the distribution of fluid saturation (Figure 7.2) for the synthetic unconsolidated sand of Case No. 7.7.1 (the corresponding layer bulk moduli are given in Table 7.1)

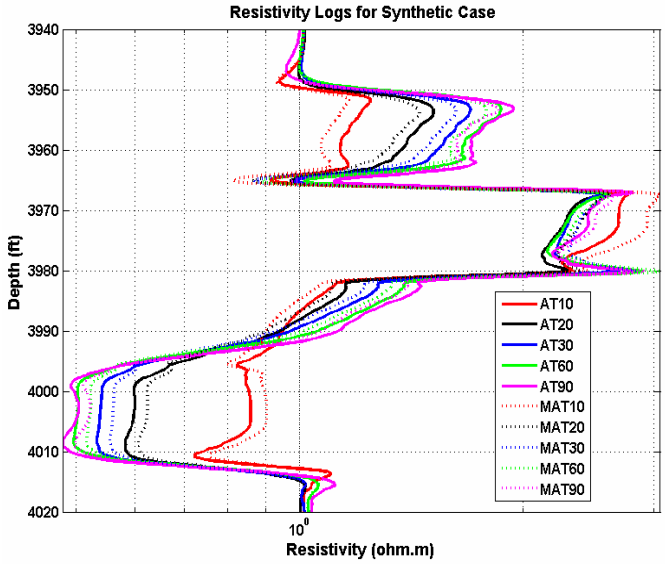

Figure 7.4: Measured and simulated array-induction resistivity curves two days after the onset of water-base mud-filtrate invasion for Case No. 7.7.1. Solid lines describe the synthetic field curves, while dotted lines describe the simulated matched curves.

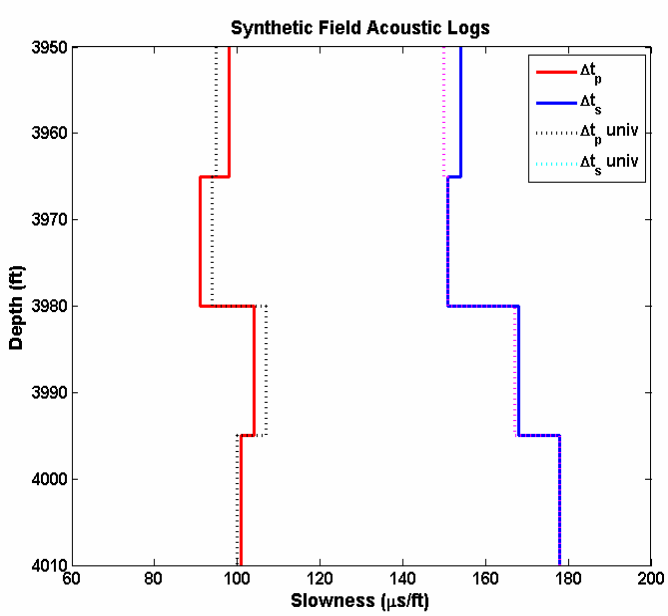

Figure 7.5: Synthetic field logs generated from borehole sonic waveform simulation performed on the spatial distributions of P-and S-wave velocities, and bulk density shown in Figure 7.3. Solid lines identify curves for the invaded case, while dotted lines identify curves corresponding to borehole sonic logs corrected for invasion effects.

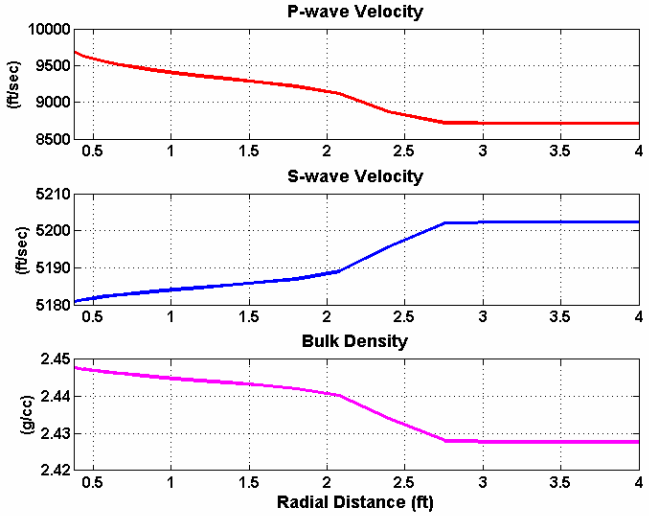

Figure 7.6: Plots of P- and S-wave velocities and bulk density as a function of radial distance away from the wellbore at a logging depth of 3972.5 ft with an estimate of k_{dry} = 6 GPa, for the synthetic formation model (Case No. 7.7.1).

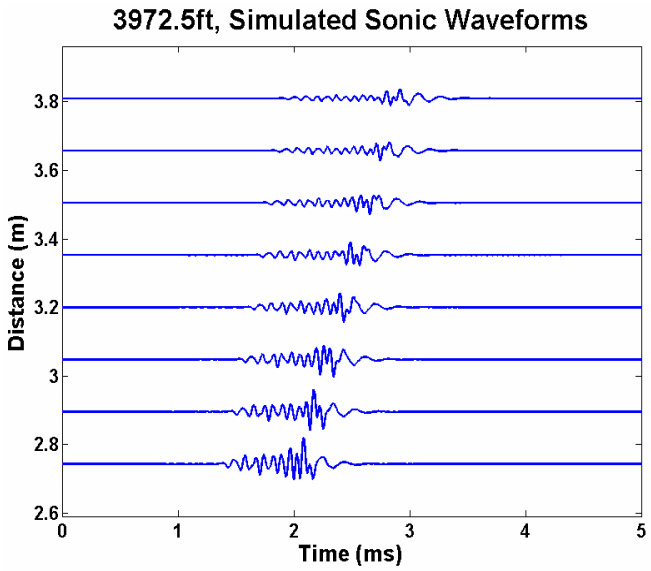

Figure 7.7: Simulated sonic waveforms at a logging depth of 3972 ft with an initial guess of k_{dry} = 10.25 GPa in the synthetic formation model (Case No. 7.7.1).

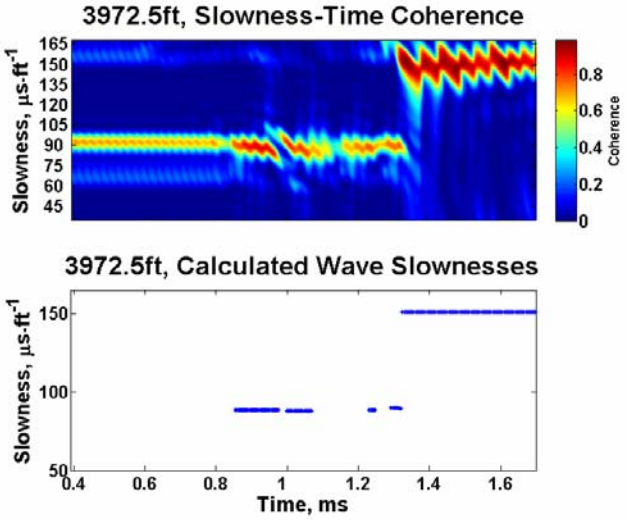

Figure 7.8: Slowness-Time Coherence (STC) results at a logging depth of 3972 ft with an estimate of k_{dry} = 10.25 GPa and μ_{dry} = 10.433 GPa for the synthetic formation model (Case No. 7.7.1).

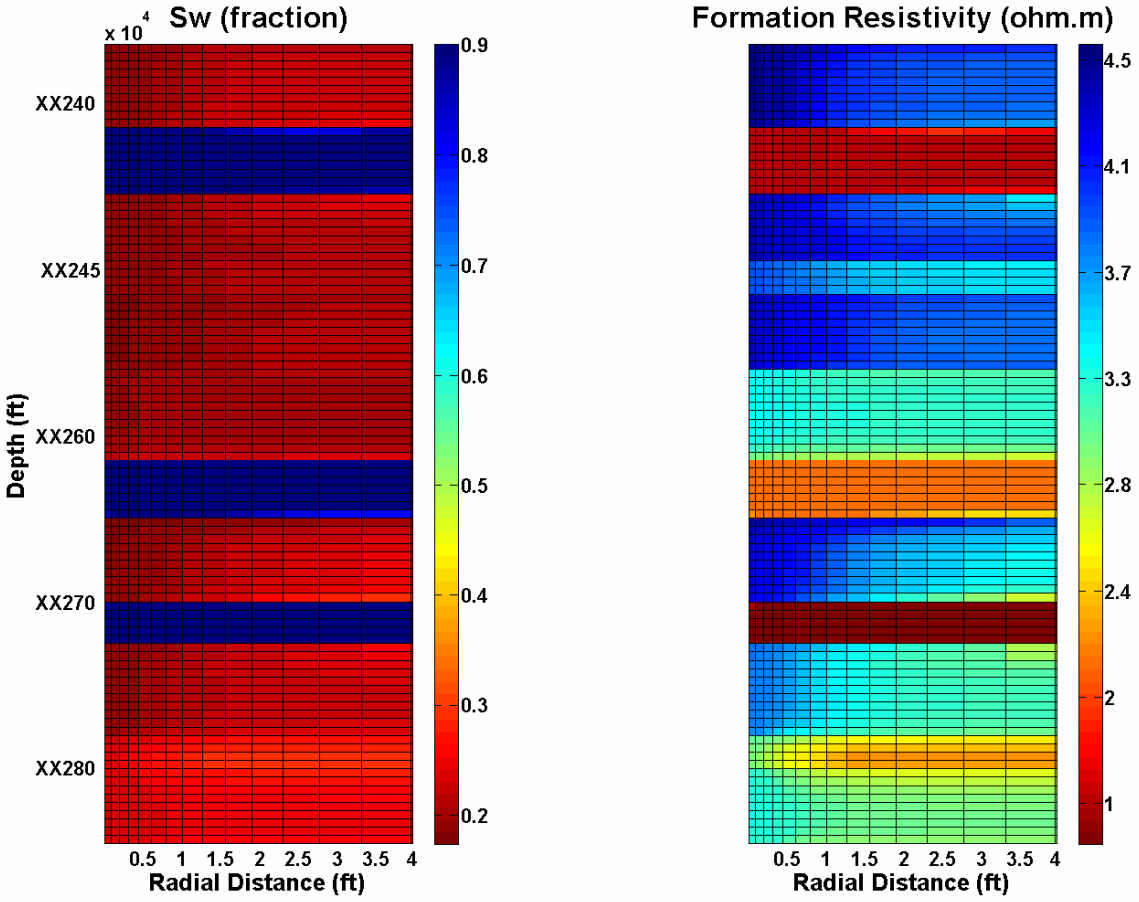

Figure 7.9: Spatial distributions (radial and vertical directions) of water saturation (left panel) and electrical resistivity (right panel) calculated after 3 days of oil-base mud-filtrate invasion into a partially-saturated oil interval in the unconsolidated shaly sand of Case No. 7.7.2.

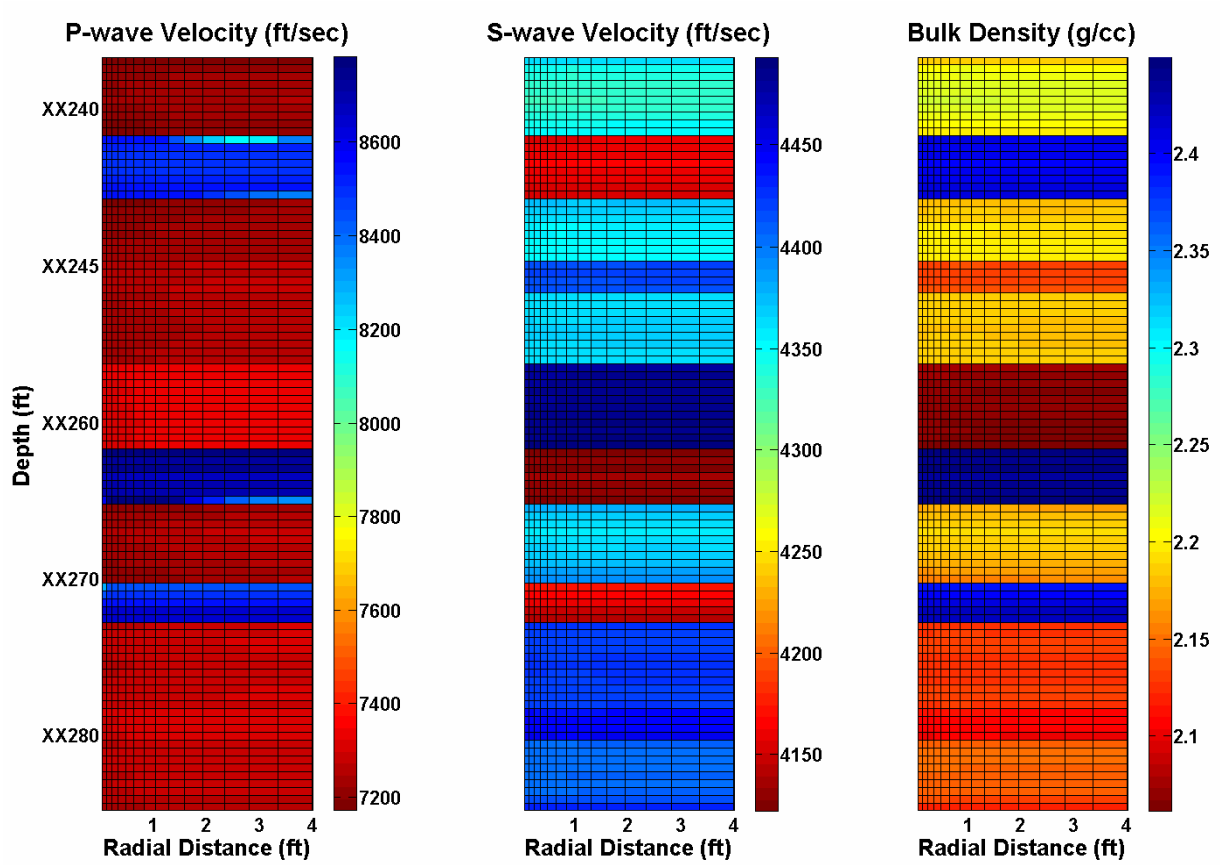

Figure 7.10: Spatial distributions (radial and vertical directions) of P-wave velocity (left panel), S-wave velocity (center panel), and bulk density (right panel) obtained from Biot-Gassmann's fluid substitution applied to the distribution of fluid saturation (Figure 7.9) for the unconsolidated shaly sand formation of Case No. 7.7.1, using an estimate of k_{dry} = 4 GPa.

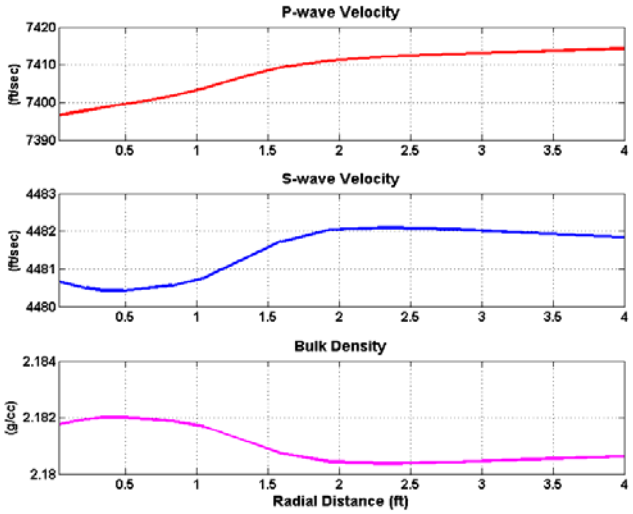

Figure 7.11: Plots of P- and S-wave velocities and bulk density as a function of radial distance away from the wellbore at a logging depth of XX260 ft, for the unconsolidated shaly sand formation (Case No. 7.7.2), using an estimate of k_{dry} = 4 GPa.

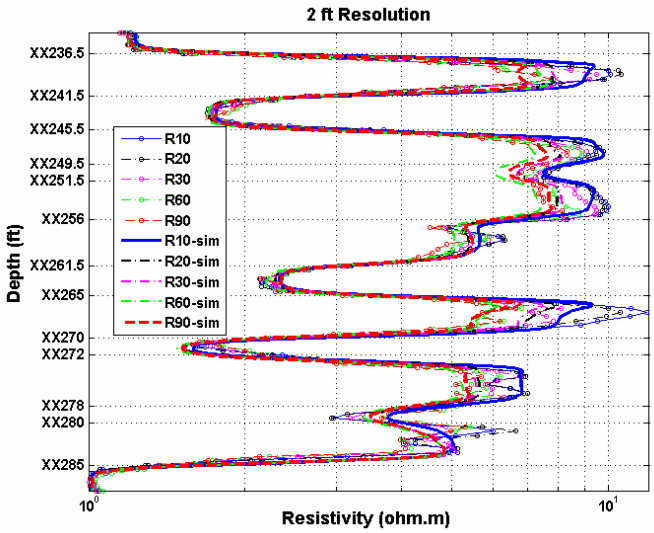

Figure 7.12: Measured and simulated array-induction resistivity curves three days after the onset of oil-base mud-filtrate invasion for Case No. 7.7.2. Continuous lines identify simulated results while dotted lines identify field curves.

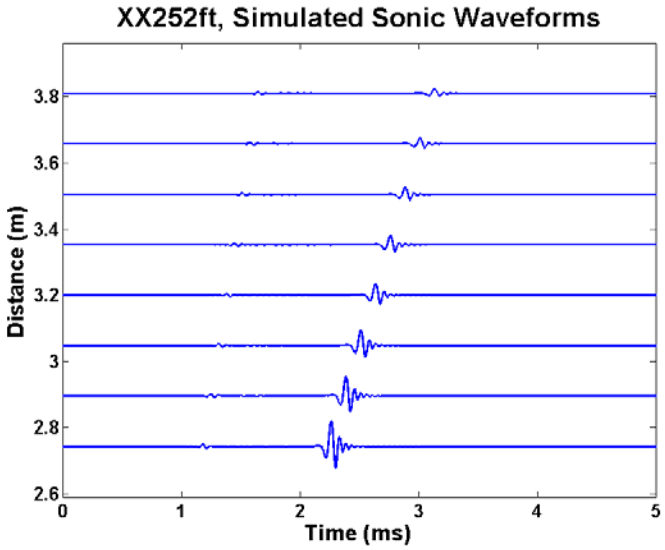

Figure 7.13: Simulated sonic waveforms at a logging depth of XX252 ft, with an initial guess of k_{dry} = 4 GPa in the unconsolidated shaly sand formation of Case No. 7.7.2.

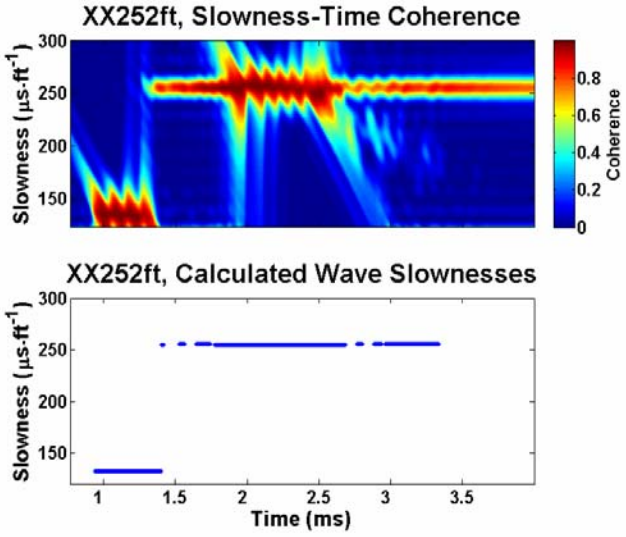

Figure 7.14: Slowness-Time Coherence (STC) results at a logging depth of XX252 ft, with final estimates of k_{dry} = 4.30 GPa and μ_{dry} = 3.3589 GPa in the unconsolidated shaly sand formation of Case No. 7.6. 2.

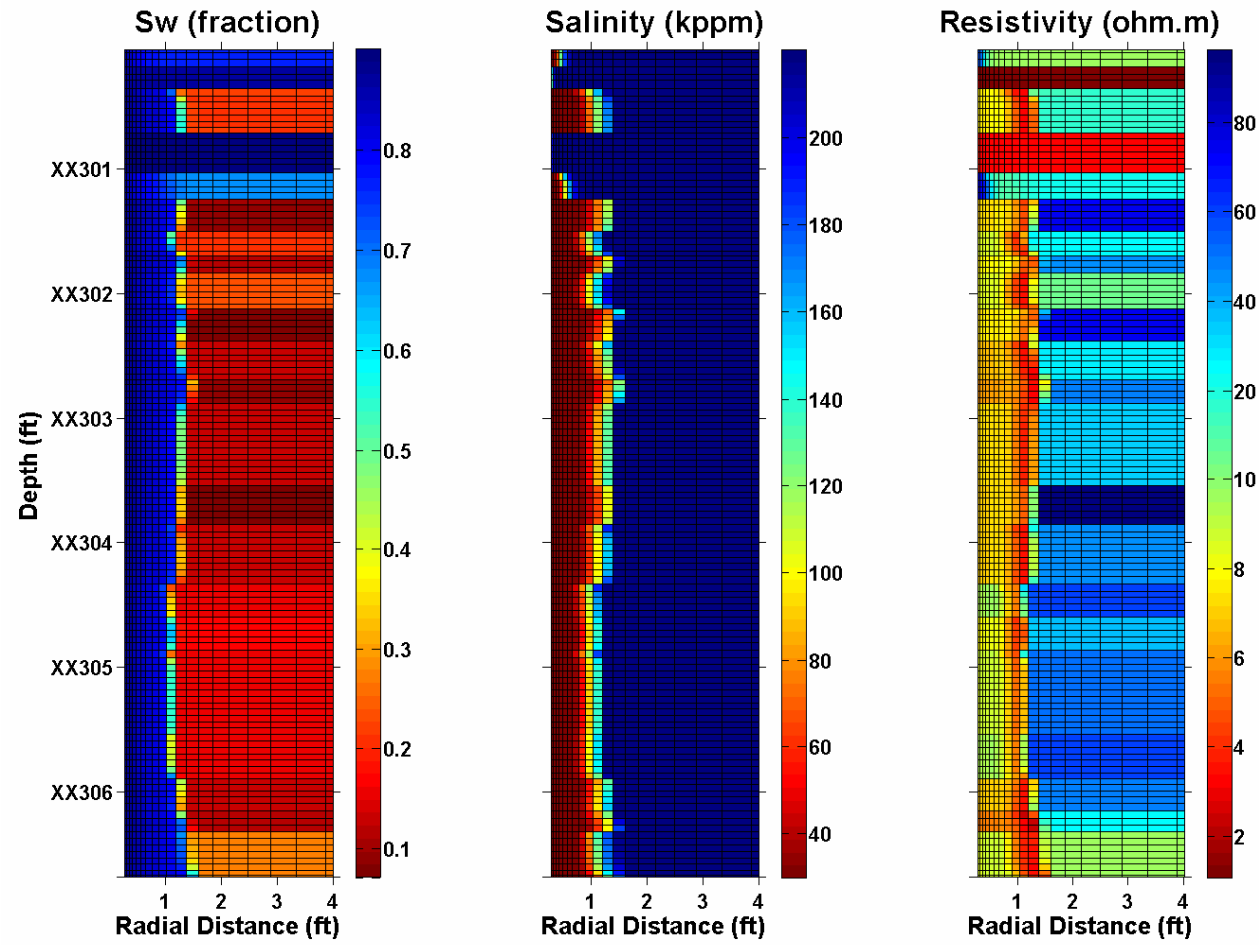

Figure 7.15: Spatial distributions (radial and vertical directions) of water saturation (left panel), salt concentration (center panel), and electrical resistivity (right panel) across the zone of interest in the tight-gas sand of Case No. 7.7.3.

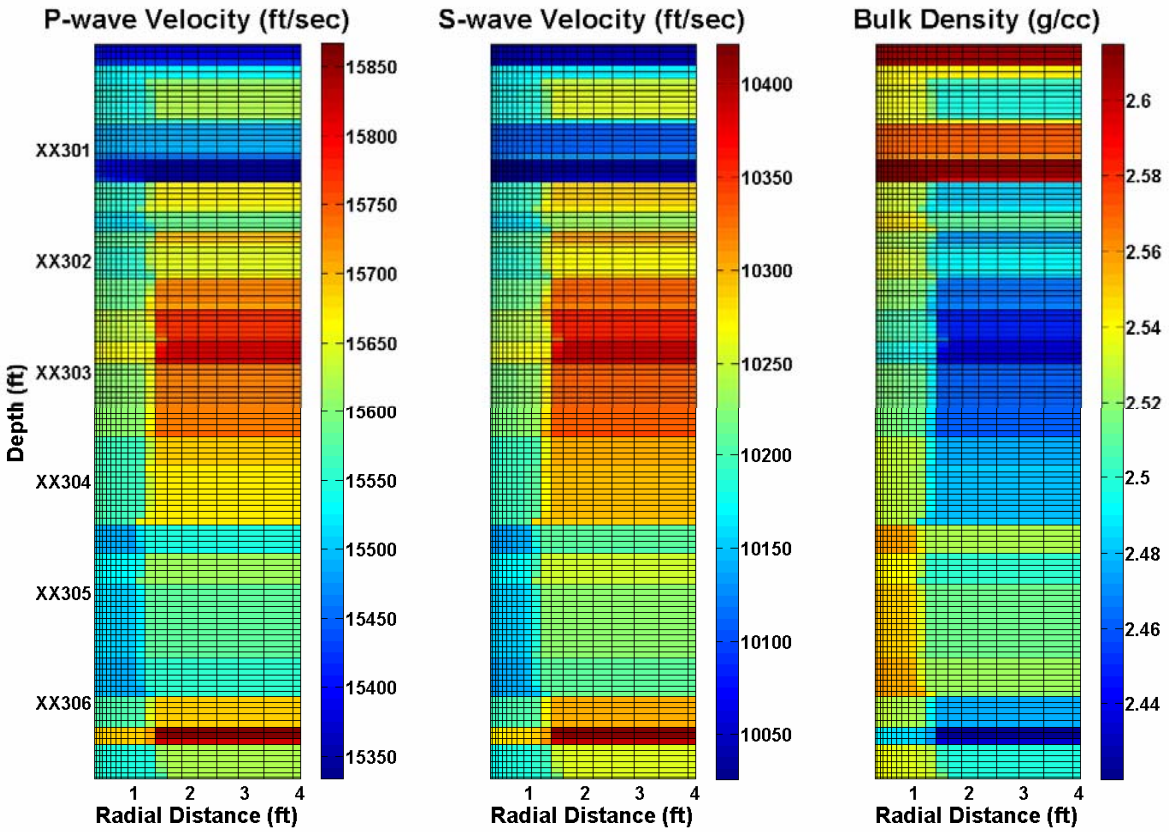

Figure 7.16: Spatial distributions (radial and vertical directions) of P-wave velocity (left panel), S-wave velocity (center panel), and bulk density (right panel) obtained from Biot-Gassmann's fluid substitution applied to the distribution of fluid saturation (Figure 7.15) for the tight-gas sand formation of Case No. 7.7.3, using an estimate of k_{dry} = 21.5 GPa.

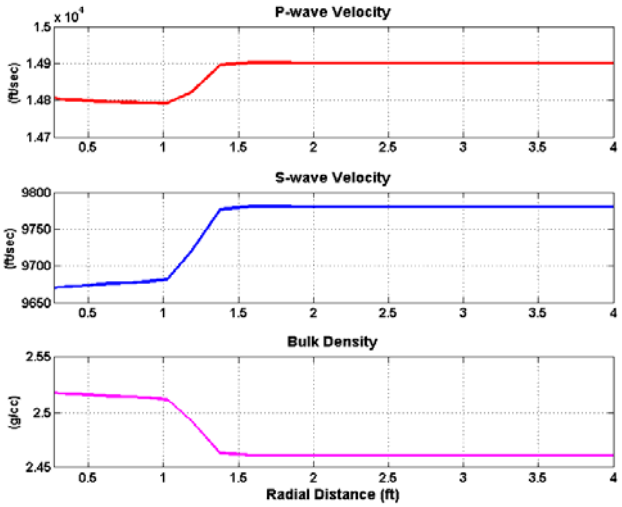

Figure 7.17: Plots of P- and S-wave velocities and bulk density as a function of radial distance away from the wellbore at a logging depth of XX303 ft, for the tight-gas sand formation (Case No. 7.7.3), using an estimate of k_{dry} = 21.5 GPa.

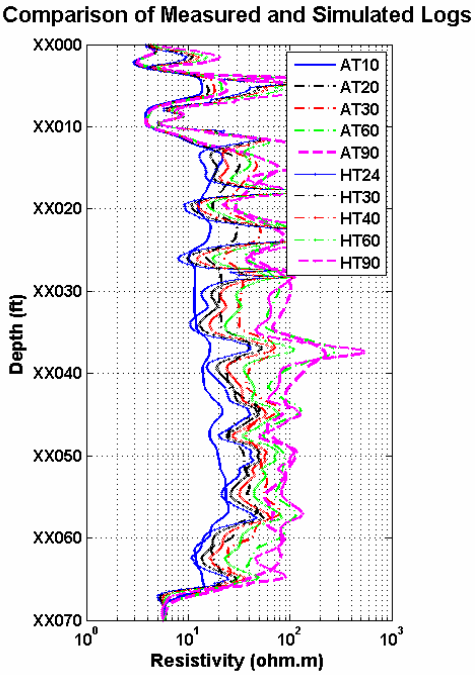

Figure 7.18: Measured high-resolution array-induction resistivity curves and simulated array-induction resistivity curves two days after the onset of water-base mud-filtrate invasion for Case No. 7.7.3. In the legend, AT identifies simulated array-induction measurements, while HT identifies high-resolution induction measurements.

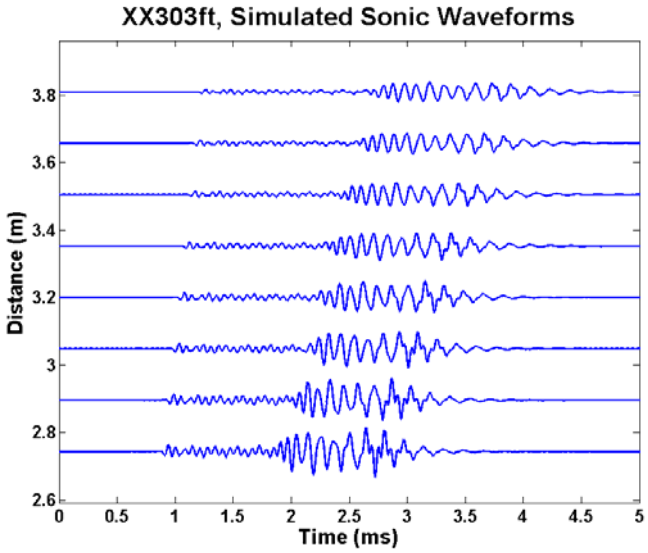

Figure 7.19: Simulated sonic waveforms at a logging depth of XX303 ft, with an initial guess of k_{dry} = 21.5 GPa and μ_{dry} = 21.8839 GPa in the tight-gas sand formation of Case No. 7.7.3.

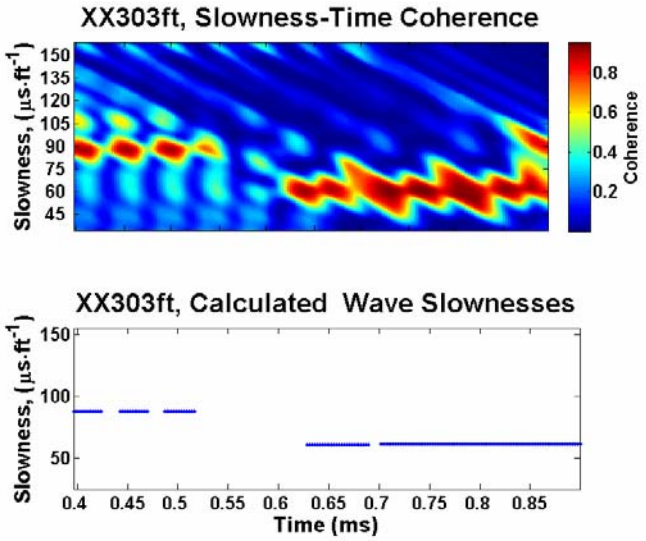

Figure 7.20: Slowness-Time Coherence (STC) results at a logging depth of XX303 ft, with estimates of k_{dry} = 29 GPa and μ_{dry} = 29.5179 GPa in the tight-gas sand formation of Case No. 7.7.3.

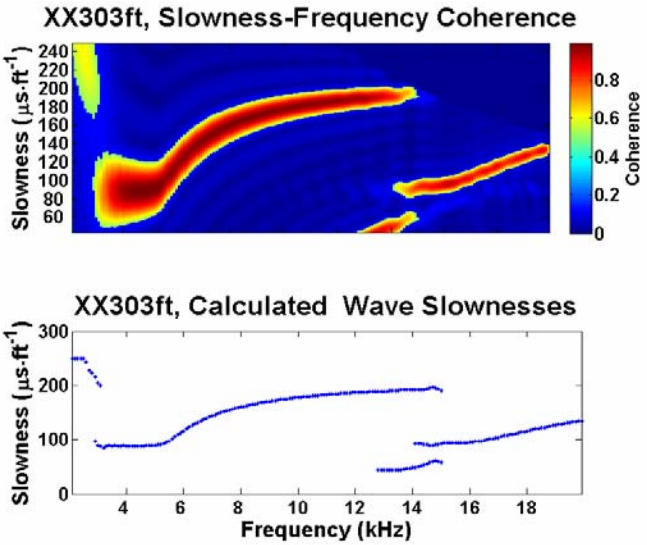

Figure 7.21: Results of dispersion analysis at a logging depth of XX303 ft with estimates of k_{dry} = 29 GPa and μ_{dry} = 29.5179 GPa in the tight-gas sand formation of Case No. 7.7.3.

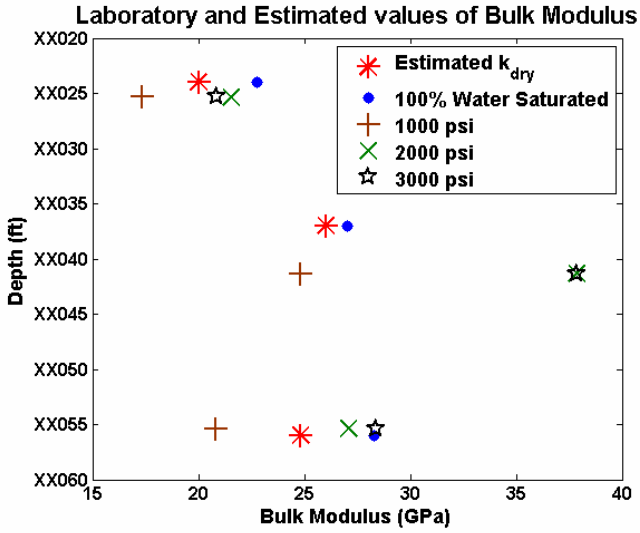

Figure 7.22: Comparison of estimated dry-bulk modulus and laboratory measurements obtained from multi-stage tri-axial compressional tests performed on core samples retrieved from the tight-gas sand formation of Case No. 7.7.3.

CHAPTER 8

FORWARD AND INVERSE MODELING OF FULL WAVEFORM SINGLE-WELL SEISMIC DATA

We develop a finite difference numerical method to investigate the sensitivity of acoustic waveform data to the rock-physics parameters and the spatial distribution of rock types near a single borehole, and develop a Bayesian model to invert the recorded seismic full waveform data for the rock-physics parameters using Markov chain Monte Carlo sampling (MCMC) methods. The results of the forward studies show that the sensitivity of the recorded acoustic full waveform data (i.e., particle velocities and stresses along the horizontal and vertical directions) to rock-physics properties is a function of the distance away from the borehole, most sensitive at the location directly adjacent to the borehole, less sensitive at the location a few meters away from the borehole, and insensitive at the location far away from the borehole. The results of the inverse modeling show that if given the spatial distribution of rock types, the full waveforms data collected from the borehole could provide very good information about the rock-physics parameters. Even using those data with 10-percent relative Gaussian random noise, we can still get very good estimates of rock-physics parameters. Both forward and inverse studies also show that, to obtain good estimates of the spatial distribution of rock types and rock-physics parameters in a large domain, we need incorporate various other sources of information, for example, data from cross-well seismic surveys and from a vertical seismic profile (VSP), and data from electromagnetic surveys

8.1 INTRODUCTION

Single-well based seismic methods, such as sonic logging (also known as the continuous velocity or acoustic logging) is one of the most widely used geophysical methods in borehole environments (Chen et al., 1998). A sonic tool normally contains several receivers about 30 cm apart and one or more transmitters about 90-150 cm from the nearest receivers. A slotted sleeve is typically used to hold the sources and receivers in addition to other supporting components. The receivers generally measure P-wave and S-wave velocity, and the advanced methods can also be used to measure the pressure in different directions.

The studies regarding single-well seismic methods have primarily been on the forward modeling of acoustic waves in borehole environments. These include the real axis and the

branch-cut integration methods for concentrically layered formations (Biot, 1952; Tsang and Radar, 1979; Cheng and Toksoz, 1981; Liu and Chang, 1994), the numerical mode matching techniques, and 2D finite difference methods (FD). For non-axisymmetrical media, the finite difference method is used predominantly because of the large number of unknown involved in a 3D elastic waveform modeling problem. Two types of FD methods have been developed for modeling acoustic full waveforms: codes developed in the Cartesian coordinates and in a cylindrical coordinates. A full 3D cylindrical FD algorithm is more important in designing and analyzing the sonic logging tools and in understanding the elastic wave propagation in the presence of the tool (Chen et al., 1998).

However, sensitivity analysis of recorded full waveform data to the changes in rock-physics parameters and in the spatial distribution of rock types at the location surrounding the borehole have not been well understood. In addition, inverse modeling of full waveform single-well seismic data have not been received much attention because of the complex of environments and conditions in the borehole involved.

In this study, we conduct research on both forward and inverse modeling of full waveform seismic data based on synthetic cases that have two types of rock at the location surrounding the borehole. The forward model is a finite difference numerical model based on the acoustic and elastic wave equations in the cylindrical coordinates system. The focus of the forward study is on the sensitivity analysis of the borehole seismic data to the changes in rock-physics parameters and in the spatial distribution of rock types. The focus of the inverse modeling is on the feasibility of using our developed stochastic method to estimate rock-physics parameters.

The remainder of the chapter is arranged as follows. Sections 8.2 and 8.3 introduce the methods for the forward and inverse modeling of single-well seismic data. Section 8.4 briefly describes the Markov chain Monte Carlo sampling methods. Section 8.5 is a synthetic study on sensitivity using the forward model developed in Section 8.2. Section 8.6 is the sampling based Bayesian model for inverting synthetic full waveform data. The discussion and conclusion is given in Section 8.7.

8.2 NUMERICAL FORWARD MODELING

8.2.1 Elastic wave equations

The forward model used in this study is the two-dimensional (2D) finite difference codes developed according to the acoustic and elastic wave propagation equations in a cylindrical coordinate system given by Chen et al. (1998). Let ρ, λ, and μ represent density, Lame constant, and shear modulus, respectively. Let v_r and v_z represent particle velocity along the radial and vertical directions. Let τ_{rr}, τ_{zz}, and τ_{rz} represent stresses in a cylindrical system. By ignoring all the force and stress sources, we obtain the following elastic wave equations:

$$\rho \frac{\partial v_r}{\partial t} = \frac{1}{r}\frac{\partial (r\tau_{rr})}{\partial r} + \frac{\partial \tau_{rz}}{\partial z}, \tag{8.1}$$

$$\rho \frac{\partial v_z}{\partial t} = \frac{1}{r}\frac{\partial (r\tau_{rz})}{\partial r} + \frac{\partial \tau_{zz}}{\partial z}, \tag{8.2}$$

$$\frac{\partial \tau_{rr}}{\partial t} = \lambda\left(\frac{1}{r}\frac{\partial (rv_r)}{\partial r} + \frac{\partial v_z}{\partial z}\right) + 2\mu\frac{\partial v_r}{\partial r}, \tag{8.3}$$

$$\frac{\partial \tau_{zz}}{\partial t} = \lambda\left(\frac{1}{r}\frac{\partial (rv_r)}{\partial r} + \frac{\partial v_z}{\partial z}\right) + 2\mu\frac{\partial v_z}{\partial z}, \tag{8.4}$$

$$\frac{\partial \tau_{rz}}{\partial t} = \mu\left(\frac{\partial v_r}{\partial z} + \frac{\partial v_z}{\partial r}\right). \tag{8.5}$$

8.2.2 Discretization

We use the central differencing schemes with staggered grids given by Levander (1988) to calculate spatial derivatives in Equations 8.1-8.5. Let $r = m\Delta r$ and $z = n\Delta z$. Therefore, the finite difference of the normal stress τ_{rr} is given by

$$\begin{aligned} D_r\tau_{rr}(m+1/2,n) = {} & c_1(\tau_{rr}(m+1/2,n) - \tau_{rr}(m-1/2,n)) \\ & - c_2(\tau_{rr}(m+3/2,n) - \tau_{rr}(m-3/2,n)), \end{aligned} \tag{8.6}$$

where c_1 and c_2 are the inner and outer difference coefficients for the fourth-order approximation to the first derivative and they take values of 9/8 and 1/24, respectively. As shown by Levander (1988), such discretization schemes give a second-order accuracy in time and a

fourth-order accuracy in space. Similarly, we can calculate the finite differences of other variables as follows:

$$D_z\tau_{zz}(m,n+1/2) = c_1(\tau_{zz}(m,n+1/2) - \tau_{zz}(m,n-1/2)) - c_2(\tau_{zz}(m,n+3/2) - \tau_{zz}(m,n-3/2)), \tag{8.7}$$

$$D_r\tau_{rz}(m+1/2,n) = c_1(\tau_{rz}(m+1/2,n) - \tau_{rz}(m-1/2,n)) - c_2(\tau_{rz}(m+3/2,n) - \tau_{rz}(m-3/2,n)), \tag{8.8}$$

$$D_z\tau_{rz}(m,n+1/2) = c_1(\tau_{rz}(m,n+1/2) - \tau_{rz}(m,n-1/2)) - c_2(\tau_{rz}(m,n+3/2) - \tau_{rz}(m,n-3/2)), \tag{8.9}$$

$$D_r v_r(m+1/2,n) = c_1(v_r(m+1/2,n) - v_r(m-1/2,n)) - c_2(v_r(m+3/2,n) - v_r(m-3/2,n)), \tag{8.10}$$

$$D_z v_z(m,n+1/2) = c_1(v_z(m,n+1/2) - v_z(m,n-1/2)) - c_2(v_z(m,n+3/2) - v_z(m,n-3/2)), \tag{8.11}$$

$$D_r v_z(m+1/2,n) = c_1(v_z(m+1/2,n) - v_z(m-1/2,n)) - c_2(v_z(m+3/2,n) - v_z(m-3/2,n)), \tag{8.12}$$

$$D_z v_r(m,n+1/2) = c_1(v_r(m,n+1/2) - v_r(m,n-1/2)) - c_2(v_r(m,n+3/2) - v_r(m,n-3/2)). \tag{8.13}$$

8.2.3 Boundary conditions

We use a nonreflecting boundary condition for the proceeding discrete acoustic and elastic wave equations, as done by Cerjan et al. (1985). It is based on gradual reduction of the amplitudes in a strip of nodes along the boundary of the mesh. This method appears simple but very robust, and can be applied to a wide variety of time-dependent problems. As demonstrated by the chapter, the effectiveness of this method does not decrease for shallow angles of incidence.

In the procedure for computing numerical values of velocity and stress, the nonreflecting condition reduces the amplitudes of those quantities slightly after each time step in a strip of nodes surrounding the numerical mesh. The reduction in each strip is gradually tapered from a zero value in the interior boundary by the following factor:

$$G = \exp\left(-(\alpha(n-i))^2\right), \tag{8.14}$$

where α is a damping coefficient and given by 0.015 by Cerjan et al. (1985).

8.2.4 Requirements for spatial and temporal discretization size

To ensure the spatial resolution and temporal stability, we have to choose suitable grid size in time and in space for the discretization. The grid size along both horizontal and vertical reactions should be less than one-eighth of the slowest S-wavelength, that is,

$$\max(\Delta r, \Delta z) < \frac{1}{8}\frac{\min(v_s)}{f_c}, \tag{8.15}$$

where v_s represents S-wave velocity and f_c represents the dominant frequency. The time step size should satisfy the following condition:

$$\Delta t < \frac{\min(\Delta r, \Delta z)}{\sqrt{2c_p(c_1 + c_2)}}, \tag{8.16}$$

where c_p is the maximum P-wave velocity in the media.

8.3 STOCHASTIC INVERSE MODELING

In this section, we describe a stochastic model for inverting acoustic data collected from a borehole, which include full waveforms of particle velocities and stresses. The unknown parameters are the spatial distributions of rock types and their associated elastic properties, such as bulk and shear moduli and density.

8.3.1 Bayesian framework

We develop a Bayesian model based on the numerical forward modeling of the acoustic wave equations given in Section 8.2. We may have multiple sources and receivers. At each receiver, we may collect pressure and velocity waveform data. We divide the spatial domain as given in Figure 8.8.1(a) into many cells, n_r grids along the horizontal direction, and n_z grids along the vertical direction. To account for absorbing boundaries conditions, we add n_{rb} grids along the horizontal direction and n_{zb} grids above and below the regular domain. For ease of description, we let m be the total number of grids along the vertical direction, where

$m = n_z + 2n_{zb}$, and let n be the total number of grids along the horizontal direction, that is, $n = n_r + n_{rb}$. Since we have to satisfy the requirements for the grid size in time and space given by Equations 8.8 and 8.9, the numbers of the grids along the horizontal and vertical direction could be quite large.

Although our ultimate goal is to estimate reservoir parameters, we estimate rock-physics parameters at the current study, and this can be linked to reservoir parameters through rock-physical models in the late study. To reduce the number of unknowns in the inversion, we invert the spatial distribution of categorical values of rock types and their associated rock-physics parameters.

Suppose we have M different types of rock surrounding a borehole. Consider a categorical variable $L(r,z)$ at location (r,z) that takes a value of j, where $j \in \{1,2,\cdots,M\}$. For rock type j, we estimate bulk modulus K_j, shear modulus μ_j, and density ρ_j. Let vector $\mathbf{K} = (K_1, K_2, \cdots, K_m)^T$, where T represent the transpose of a vector. Similarly, we let $\boldsymbol{\mu} = (\mu_1, \mu_2, \cdots, \mu_m)^T$, and let $\boldsymbol{\rho} = (\rho_1, \rho_2, \cdots, \rho_m)^T$. Let $\mathbf{L}$ be unknown rock types at all the location. For given seismic sources, we may collect particle waveform data, which include both particle velocities and stresses along two different direction. Let matrices $\mathbf{v_r}$ and $\mathbf{v_z}$ denote particle velocities along vertical and horizontal directions for a given time window. Let $\boldsymbol{\tau}_{\mathbf{rr}}$ and $\boldsymbol{\tau}_{\mathbf{zz}}$ denote particle stresses along vertical and horizontal directions for the same time window. The Bayesian models for estimating those unknown parameters are given as follows:

$$f(\mathbf{K},\ \boldsymbol{\mu},\ \boldsymbol{\rho},\ \mathbf{L} \mid \mathbf{v_r},\ \mathbf{v_z},\ \boldsymbol{\tau}_{\mathbf{rr}},\ \boldsymbol{\tau}_{\mathbf{zz}}) \propto f(\mathbf{v_r},\ \mathbf{v_z},\ \boldsymbol{\tau}_{\mathbf{rr}},\ \boldsymbol{\tau}_{\mathbf{zz}} \mid \mathbf{K},\ \boldsymbol{\mu},\ \boldsymbol{\rho},\ \mathbf{L}) f(\mathbf{K},\ \boldsymbol{\mu},\ \boldsymbol{\rho},\ \mathbf{L}) \tag{8.17}$$

The first term on the right of Equation 8.17 is referred to as the likelihood function, which is the link between data and unknown parameters. The second term on the right of the equation is referred to as the prior distribution, which summarizes the information that is not included in the current data. Notice that both particle velocity and stress are functions of time. For the inversion, we pick pre-determined time windows for the problems.

8.3.2 Likelihood Models

We assume that seismic velocity and stress along the two different directions are independent of each other, and thus we can write the likelihood function as the product of several terms as given below:

$$\begin{aligned} & f(\mathbf{K},\ \boldsymbol{\mu},\ \boldsymbol{\rho},\ \mathbf{L} \mid \mathbf{v_r},\ \mathbf{v_z},\ \boldsymbol{\tau}_{\mathbf{rr}},\ \boldsymbol{\tau}_{\mathbf{zz}}) \\ & \quad \propto f(\mathbf{v_r} \mid \mathbf{K},\ \boldsymbol{\mu},\ \boldsymbol{\rho},\ \mathbf{L}) f(\mathbf{v_z} \mid \mathbf{K},\ \boldsymbol{\mu},\ \boldsymbol{\rho},\ \mathbf{L}) \\ & \quad\quad f(\boldsymbol{\tau}_{\mathbf{rr}} \mid \mathbf{K},\ \boldsymbol{\mu},\ \boldsymbol{\rho},\ \mathbf{L}) f(\boldsymbol{\tau}_{\mathbf{zz}} \mid \mathbf{K},\ \boldsymbol{\mu},\ \boldsymbol{\rho},\ \mathbf{L}). \end{aligned} \tag{8.18}$$

We first describe the likelihood function of acoustic velocity along the horizontal direction. Let vector $\mathbf{v_r} = \{v_r(i,j)\}$, where $i = 1, 2, \cdots, m_a$, and m_a is the number of receivers, and $j = 1, 2, \cdots, m_d$, and m_d is the number of time samples in a given time window. Thus,

$$v_r(i,j) = M_{ij}(\mathbf{K},\ \boldsymbol{\mu},\ \boldsymbol{\rho},\ \mathbf{L}) + \varepsilon_{ij}, \tag{8.19}$$

where M_{ij} is the $ij-th$ component of the seismic forward model and ε_{ij} represents its corresponding measurement error. We follow here the common assumption that the measurement errors have a Gaussian distribution with zero mean and are uncorrelated to each other (Malinverno, 2002; Buland and Omre, 2003), and thus we obtain the likelihood function of seismic data as follows:

$$f(\mathbf{v_r} \mid \mathbf{K},\ \boldsymbol{\mu},\ \boldsymbol{\rho},\ \mathbf{L}) = \prod_{\mathrm{i=1}}^{\mathrm{m_a}} \prod_{\mathrm{j=1}}^{\mathrm{m_d}} \frac{1}{\sqrt{2\pi}} \tau_i^{1/2} \exp\left(-\frac{\tau_i}{2} (v_r(i,j) - M_{ij}(\mathbf{K},\ \boldsymbol{\mu},\ \boldsymbol{\rho},\ \mathbf{L}))^2 \right), \tag{8.20}$$

where τ_i is the inverse variance of measurement errors at the $i-th$ receiver. Similarly, we can obtain other likelihood functions as follows:

$$f(\mathbf{v}_z \mid \mathbf{K},\ \boldsymbol{\mu},\ \boldsymbol{\rho},\ \mathbf{L}) = \prod_{\mathrm{i=1}}^{\mathrm{m_a}} \prod_{\mathrm{j=1}}^{\mathrm{m_d}} \frac{1}{\sqrt{2\pi}} \tau_i^{1/2} \exp\left(-\frac{\tau_i}{2} (v_r(i,j) - M_{ij}(\mathbf{K},\ \boldsymbol{\mu},\ \boldsymbol{\rho},\ \mathbf{L}))^2 \right), \tag{8.21}$$

$$f(\boldsymbol{\tau}_{rr} \mid \mathbf{K},\ \boldsymbol{\mu},\ \boldsymbol{\rho},\ \mathbf{L}) = \prod_{\mathrm{i=1}}^{\mathrm{m_a}} \prod_{\mathrm{j=1}}^{\mathrm{m_d}} \frac{1}{\sqrt{2\pi}} \tau_i^{1/2} \exp\left(-\frac{\tau_i}{2} (\tau_{rr}(i,j) - M_{ij}(\mathbf{K},\ \boldsymbol{\mu},\ \boldsymbol{\rho},\ \mathbf{L}))^2 \right), \tag{8.22}$$

$$f(\boldsymbol{\tau}_{zz} \mid \mathbf{K},\ \boldsymbol{\mu},\ \boldsymbol{\rho},\ \mathbf{L}) = \prod_{\mathrm{i=1}}^{\mathrm{m_a}} \prod_{\mathrm{j=1}}^{\mathrm{m_d}} \frac{1}{\sqrt{2\pi}} \tau_i^{1/2} \exp\left(-\frac{\tau_i}{2} (\tau_{zz}(i,j) - M_{ij}(\mathbf{K},\ \boldsymbol{\mu},\ \boldsymbol{\rho},\ \mathbf{L}))^2 \right). \tag{8.23}$$

8.3.3 Prior Model

The prior distribution is determined using prior knowledge and other information about the unknown parameters. We assume all the unknown parameters are independent of each other. As a result, we can write the joint prior distribution as the product of each individual prior distribution as given below:

$$f(\mathbf{K}, \boldsymbol{\mu}, \boldsymbol{\rho}, \mathbf{L}) = f(\mathbf{K}) f(\boldsymbol{\mu}) f(\boldsymbol{\rho}) f(\mathbf{L}) \tag{8.24}$$

For rock physics parameters, we assume that they are uniformly distributed within given ranges. For rock type $\mathbf{L}$, we assume it spatially distributed with a given spatial correlation.

8.4 SAMPLING METHODS

We use Markov chain Monte Carlo (MCMC) sampling methods to obtain estimates of unknown parameters from the Bayesian model defined in Equation 8.17. Unlike optimization-based methods seeking single optimal solutions of unknown parameters, MCMC sampling-based methods draw many samples from the joint posterior distribution. Using those samples, we can make inferences about the marginal distributions of each parameter, such as its mean, variance, and predictive intervals.

MCMC sampling methods have been found recently to be useful for inverting complex geophysical data set by numbers of authors, such as Bosch (1999), Malinverno (2002), and Buland et al. (2003). The main steps for using MCMC methods entail: (1) deriving conditional probability functions given all the data and other unknown variables, which are referred to as full conditional distribution functions; (2) generating samples using suitable algorithms; (3) making inferences about each unknown. In the following, we first show the full conditional distribution functions of unknown vectors given in Equation 8.1 and then describe the sampling algorithms used in this study, which include the Metropolis-Hasting methods (Metropolis et al., 1953; Hasting, 1970; Besag, 2001) and the slice sampling methods (Neal, 2003). We use different sampling strategies to draw samples of spatial distribution of rock types and the unknown rock-physics properties.

8.4.1 Sampling bulk and shear moduli and density for each rock type

We first derive the conditional probability distribution function for each type of rock-physics parameter, given all the data and all the other variables. In this step, we assume that the spatial distribution of rock types $\mathbf{L}$ is given. Since MCMC sampling methods only concern

those terms in the joint posterior probability distribution function that relate to elastic bulk and shear moduli and density, we can obtain each joint conditionals by dropping those terms in Equation 8.17 that are not related to the rock-physics parameters. Consequently, we obtain

$$f(\mathbf{K}\,|\,\cdot) \propto f(\mathbf{K}) f(\mathbf{v}_r, \mathbf{v}_z, \boldsymbol{\tau}_{rr}, \boldsymbol{\tau}_{zz}\,|\,\mathbf{K}, \boldsymbol{\mu}, \boldsymbol{\rho}, \mathbf{L}). \tag{8.25}$$

Similarly, we can obtain the conditionals of shear modulus and density given all data and other variables as follows:

$$f(\boldsymbol{\mu}\,|\,\cdot\,) \propto f(\mathbf{K}) f(\mathbf{v}_r, \mathbf{v}_z, \boldsymbol{\tau}_{rr}, \boldsymbol{\tau}_{zz}\,|\,\mathbf{K},\ \boldsymbol{\mu},\ \boldsymbol{\rho},\ \mathbf{L}), \tag{8.26}$$

$$f(\boldsymbol{\rho}\,|\,\cdot) \propto f(\boldsymbol{\rho}) f(\mathbf{v}_r, \mathbf{v}_z, \boldsymbol{\tau}_{rr}, \boldsymbol{\tau}_{zz}\,|\,\mathbf{K},\ \boldsymbol{\mu},\ \boldsymbol{\rho},\ \mathbf{L}). \tag{8.27}$$

We use slice sampling methods that are described in details by Neil (2003). Slice sampling methods have been shown very effective and require less information about the tuning parameters that control the speed of convergence to the target probability distribution function for geophysical inverse problems (Chen et al., 2007).

8.4.2 Sampling the spatial distribution of rock types

Sampling the spatial distribution of rock types is more challenging than sampling continuous rock-physics parameters because we have to account for the spatial correlation of those categorical variables. In this study, we use the Swenden-Wang model (Swenden and Wang, 1987), and this model has been widely used in the field of computer graphs and imaging to solve slow convergence problems caused by spatial correlation. One main challenging for the solving the problem is to draw many samples of the spatial distribution of rock-types.

8.4.3 Monitoring convergence of Markov chains

We can obtain many samples of unknown rock-physics parameters and the rock types $\left\{\mathbf{L}^{(t)},\ \mathbf{K}^{(t)},\ \boldsymbol{\mu}^{(t)},\ \boldsymbol{\rho}^{(t)},\ t = 1, 2, \cdots, T\right\}$ by drawing samples from the proceeding conditional pdfs. Theoretically, after a sufficiently long run (e.g., t_0 iterations, referred to as burn-in by Gilks et al., 1996), the drawn samples are approximately the samples drawn from the true joint pdf given in Equation 8.4. Many methods can be used to find the burn-in number and to monitor the convergence of the obtained Markov chains, such as the methods developed by Gelman and Rubin (1992), Geweke et al. (1992), and Raftery, 1992; we employ the Gelman and Rubin (1992) method in this study.

To perform the sampling, we first run three different chains by starting from different sets of initial values for the total number of T iterations. Secondly, we throw the first $0.5T$ number of samples for each chain and consider them as the burn-in. Finally, we calculate a criterion, referred to as the scale reduction score based on the three Markov chains If the scale reduction score is less than 1.2, the Markov chain is considered to be converged; otherwise, more runs are needed.

8.5 SYNTHETIC STUDY ON FORWARD MODELING

In this section, we conduct studies on the forward modeling of acoustic full waveforms using synthetic examples. The goal of the forward modeling is to show how acoustic waveforms change in response to the changes of the spatial distribution of the rock types and the changes of rock-physics properties. This information will provide guidelines for the subsequent inverse modeling and survey designs.

8.5.1 Discretization and rock-types of synthetic models

We consider a two-dimensional problem in the cylindrical coordinate systems (i.e., along the radial and vertical directions). The 2D cross-section surrounding the single borehole is divided into 100 x 100 grids with grid size of 0.1m x 0.1m. Above and below the domain are 20 grids, which are considered as upper and lower absorbing boundaries. At the edge of the domain is also 20 grids of absorbing boundaries. Therefore, the total size of domain of interest is 140 grids along the vertical (or z) direction and 120 grids along the horizontal (or r) direction. Suppose two types of rock present in the surrounding domain, and their elastic properties are listed in Table 8.1. Different spatial distributions construct different synthetic models.

We assume that there is one source at the vertical location 2.0m down from the upper absorbing boundary and 12 receivers with the offsets linearly increasing from 1.7m to 7.2m. Each receiver will measure both particle velocity and stresses along the radial and vertical direction (i.e., v_r, v_z, τ_{rr}, and τ_{zz}).

8.5.2 Sensitivity of acoustic waveforms to the spatial distributions of rock-types

We compare the acoustic waveforms collected from all the receivers for three different spatial distributions of rock-types. The first one (see Figure 8.8.1(a), referred to as Model-A) is a basic case, where the rock-type 2 is embedded within the rock-type 1 at the spatial domain across the depths between 8.0m and 10.5m and radial distances from 0.0 m to 5.5 m. The second one (see Figure 8.8.1(b), referred to as Model-B) is a variation of the Model-A, in which we increase the radial distance from the borehole by 0.5 m. As a result, Model-B is located at the spatial domain across the depths between 8.0 m and 10.5 m and radial distances between 0.5 m and 6.0 m. If we move the cross-section of rock-type 2 further away 0.5 m from the borehole, we get the last model (Figure 8.8.1(c), referred to as Model-C). For comparison, we also add a homogenous case, referred to as Model-0, where the entire domain is occupied by rock-type 1.

We first calculate the acoustic waveforms for the above three spatial distributions of rock-types and then compare them with those obtained from Model-0. Figure 8.8.2 shows the comparison of Model-A against the homogenous case. In the figure, the first one is the waveforms calculated from Model-A, the second one is the waveforms calculated from Model-0, and the third one is the difference. Each trace is normalized by the its maximum absolute amplitude, but we use the same scale across the three sub-figures in order to compare them. From the comparison, we find that all the traces are response differently for Model-A and Model-0. Among them, the particle velocity along the radial direction (Figure 8.8.4) is most sensitive and the particle stress along the vertical direction (Figure 8.8.7) is least sensitive to the presence of rock-type 2. We also notice that only those receivers after the depths of 8.0 m show different responses, the receivers within the rock-type 2 and below the rock-type 2.

Similarly, we compare the acoustic responses of Model-B against Model-0 (Figure 8.8.3). We can still observe the differences in the waveforms for particle velocities (v_r and v_z) and particle stress along the radial direction (τ_{rr}). But for the particle stress along the vertical direction, the difference is very small. Overall, the differences in the waveforms are smaller than those obtained from Model-A versus Model-0. We also show the comparison of responses for Model-C versus Model-0 (Figure 8.8.4). The differences for all the types of measurements are very small.

The above studies show that the acoustic waveforms recorded along the borehole is quite sensitive to the radial distances of the rock-type 2. If the borehole passes through the rock-type 2

(Model-A), we can get the best measurements. If the distances increase, the ability to detect the presence of rock-type 2 decreases (Model-B). If the distance is 1.0 m or more away from the borehole, we cannot find out whether the rock-type 2 presents or not (Model-C).

8.5.3 Sensitivity of acoustic waveforms to the location of rock-type 2

In the following, we consider Model-A as the main model and move the cross-section of Model-A 0.5 m towards the upper, down, and right directions. We compare the waveforms of each of those cases with the basic case (Model-A). Figure 8.8.5 shows the comparison when we move the cross-section upper 0.5 m, and Figure 8.8.6 shows the comparison when we move the cross-section down 0.5 m. The differences in all the waveforms are very small. Figure 8.8.7 shows comparison in the responses when we move the cross-section 0.5 m away from the borehole. We do observe the differences in the waveforms. It seems that the vertical particle velocity and radial stress distinguish the two cases better than the other recorded quantities. From the above comparisons, we realize that we face difficulties if we try to estimate the vertical locations of rock-type 2 using only the waveform data and therefore other types of information are needed to provide information regarding the vertical location of the presence of rock-type 2.

8.5.4 Sensitivity of acoustic waveforms to the changes of rock-physics properties

We use Model-A in this study to investigate how the recorded acoustic waveforms change when we change the rock-physics parameters of rock-type 2 by decreasing or increasing 20% in their values, while keeping the values of parameters in rock-type 1 same. Figure 8.8.8 compares the waveforms of particle velocities (v_r and v_z) and stresses (τ_{rr} and τ_{zz}) along the radial and vertical directions for the reduced values by 20%. We can observe the notable differences between the responses from Model-A and from the reduced values of the parameters. Similarly, Figure 8.8.9 shows the comparison of waveforms when the rock-physics parameters in type-2 increase by 20%. We also found that among the four types of recorded data, the particle velocity along the radial direction is most sensitive to the change of rock-physics parameters and the particle stress along the vertical direction is the least sensitivity to the change relative to other types of measurements. The results of the sensitivity analysis implies that we can use the observed waveform data to estimate rock-physics parameters accurately when suitable models are used.

8.6 SYNTHETIC STUDY ON INVERSE MODELING

In this section, we conduct the inverse modeling of acoustic waveform data based on the insight gained from the proceeding section. The goal of the inverse modeling is to demonstrate the use of our stochastic model for identifying possible rock-physics parameters.

8.6.1 Synthetic models and data

From the forward studies presented in the proceeding section, we realize that the recorded acoustic waveform data are most sensitive to the spatial pattern of rock-types that intersects with the borehole (Model-A), less sensitive to the pattern near the borehole (Model-B), and insensitive to the pattern that are far away from the borehole (Model-C). We also realize that when the spatial pattern moves slightly towards upper, lower, or right directions, the recorded waveforms only change slightly, but for a given spatial pattern, the changes in rock-physics parameters cause significant changes in the recorded data. Considering the above reasons, for the current inverse modeling, we only consider the spatial pattern given by Model-A, where we only invert for rock-physics parameters but not the spatial patterns.

We generated synthetic acoustic waveforms, which include particle velocities and stresses along both horizontal and vertical directions, using rock-physics parameters given in Table 8.1. We added 5% and 10% relative Gaussian random noises to each of those data sets. Figures 8.10 and 8.11 show the waveforms of noised data collected from the twelve receivers shown in Figure 8.8.1(a). From the top to the bottom of the figures, there are particle horizontal velocity, vertical velocity, horizontal stress, and vertical stress, respectively. In each row, the first column is noised data, the second column is the data without noises, and the third column is the difference. All of the data are plotted at the same scale.

8.6.2 Stochastic inversion of the synthetic waveform data

We formulated the inverse problem using the stochastic model presented in Section 8.3 and solved the inverse problem using the Markov chain Monte Carlo sampling methods. The prior ranges of unknown parameters are given in Table 8.2. We started from the initial values that are randomly generated from their corresponding prior uniform distributions. Figure 8.12 shows the traces for the six unknown parameters (black curves) and the medians of those samples (red lines). Each Markov chain is converged to its corresponding target probability

distribution. From the figure, we can see that seismic P-wave and S-wave velocity for both rock types seem to be better sampled than density because they show smaller correlation between consequent samples.

8.6.3 Marginal posterior estimates of rock-physics parameters

We can obtain extensive information on each unknown parameter from the samples drawn using MCMC sampling methods, for example, the marginal posterior mean, median, mode, and even probability density function of the unknown parameter. Figure 8.13 shows the estimated marginal posterior probability density function of each unknown rock-physics parameter using the synthetic waveform data with 5% (black curves) and 10% (red curves) relative random noise. The blue lines are the true values of each parameter. From the figure, we can see that the mode of each estimated marginal pdf is very close to the corresponding true value. The spreading of each pdf increases with the increasing of errors in the synthetic data. In addition, we can that see the modes of those pdfs do not correspond to the true values. This may be caused by the random noise added to the synthetic data sets.

Tables 8.3 and 8.4 show the detailed statistics of the estimated marginal pdfs obtained from inversion of the synthetic data with 5% and 10% relative random noise. From the tables, we can see that the mean, the median and the mode of each pdf are very close. This means each pdf is almost symmetric. We can also see that the uncertainty in the parameters of rock-type 1 generally is smaller than that of rock-type 2. Overall, the uncertainty in each estimated parameter is quite small. This is because we assume the spatial pattern is given.

8.6.4 Estimated posterior correlation among different pair of rock-physics parameters

Using the samples drawn from the joint posterior pdf, we can obtain not only information on each individual parameter but also information about correlation among different parameters. Figures 8.14 and 8.15 are the cross-plots of estimated posterior parameters when using the synthetic acoustic waveform data with 5% and 10% relative random noise, respectively. Recall that the prior distributions of those unknown variables are assumed to be independent of each other. From Figure 8.14, we can see that the posterior correlation among many pair of rock-physics parameters are still uncorrelated to each other. However, we can observe that there are strong correlations between seismic P-wave velocity, S-wave velocity, and density in the two

rock types. Their correlation coefficients are -0.6, -0.8, and 0.5, respectively. We can observe a similar result from Figure 8.15, but their correlation coefficients are slightly smaller, which are given by -0.5, -0.8, and 0.75, respectively. The posterior correlations between seismic P-wave and S-wave velocity and density in the two rock types are induced by conditioning on the synthetic waveform data. This implies that the inversion results are primarily caused by the difference in seismic P-wave and S-wave velocity and density in the two different types of rock, but not absolute values of those parameters.

8.6.5 Misfits of acoustic waveforms

We fit acoustic full waveform data of particle seismic velocity and stresses along the horizontal and vertical directions for all the twelve receivers (see Figure 8.1(a)). As we have shown in the forward studies, the recorded waveforms at the receivers before number 6 do not change with and without rock types. We can only observe the anomaly at the receivers after number 6, in which the anomaly is most at the receiver #9 and #10. As an example, Figure 8.16 shows the misfits of the synthetic noised waveforms (black curves) and the calculated waveforms using the medians of the estimated posterior pdfs. We can see that the inversion results fit the data quite well.

8.7 DISCUSSION AND CONCLUSIONS

We have conducted studies on forward and inverse modeling of full waveform seismic data collected from single borehole. The forward model used in this study is 2D finite difference codes developed according to the acoustic and elastic wave propagation equations in a cylindrical coordinate system. Although the synthetic studies presented in this chapter are simple, they still provide useful information for us to study single hole problem. Synthetic case studies based on the forwarding modeling show that when the distribution of rock types or the rock-physics properties of the rock-types change, the recorded seismic waveforms change. This provides evidence for conducting inverse modeling of seismic full waveforms data for rock-physics parameter estimation.

However, compared to the change in rock types or in rock-physics properties at the location near the borehole, the change at the location far away (several meters away) from the

borehole is difficult to be detected from boreholes. Additionally, the recorded seismic waveform data are less sensitivity to the changes in the spatial distribution of rock types than to the change in the rock-physics properties. This makes it difficult to estimate the spatial distribution of rock-types just from borehole seismic data. In this case, other types of data may be important, for example, cross-well, or surface to borehole seismic data, in order to uncertainty in the vertical direction.

The inverse model used in this study is a Bayesian model based on Markov chain Monte Carlo sampling methods. We applied the developed model to invert two sets of synthetic waveform data with Gaussian random noise. The synthetic case studies show that even the synthetic data have 10% relative random noise, the inversion results are pretty good when the spatial distribution of rock types are given. However, in practice, we typically do not have such information. Therefore, we need to incorporate more types of information, especially those data with large scale spatial information about the rock types because it seems borehole seismic data are limited in providing information to estimate the spatial pattern of rock types.

Table 8.1. Rock physics parameters of the two types of rock

	Seismic P-wave velocity (km/s)	Seismic S-wave Velocity (km/s)	Bulk Density (g/cc)
Rock-1	4.00	2.00	2.20
Rock-2	3.81	1.88	2.55

Table 8.2. Prior bounds of rock physics parameters for the two types of rock

	Seismic P-wave velocity (km/s)	Seismic S-wave Velocity (km/s)	Bulk Density (g/cc)
Rock-1	(3.00, 5.00)	(1.00, 3.00)	(2.00, 3.00)
Rock-2	(3.00, 5.00)	(1.00, 3.00)	(2.00, 3.00)

Table 8.3: Estimated rock-physics parameters and their associated uncertainty information using the synthetic data with 5% relative random noise.

Rock Type	Rock-physics Parameters	Mean	Standard Deviation	Median	Mode	95% HPD
Type-1	Vp1	4.0023	0.0010	4.0006	4.0006	(3.9986, 4.0022)
	Vs1	2.0000	3.0000e-4	2.0006	2.0006	(1.9993, 2.0005)
	ρ1	2.2035	0.0036	2.2034	2.2034	(2.1956, 2.2097)
Type-2	Vp2	3.8093	0.0025	3.8093	3.8093	(3.8041, 3.8138)
	Vs2	1.8799	6.0000e-4	1.8799	1.8798	(1.8787, 1.8810)
	ρ2	2.5553	0.0062	2.5549	2.5544	(2.5435, 2.5668)

Table 8.4: Estimated rock-physics parameters and their associated uncertainty information using the synthetic data with 10% relative random noise.

Rock Type	Rock-physics Parameters	Mean	Standard Deviation	Median	Mode	95% HPD
Type-1	Vp1	4.0014	0.0019	4.0014	4.0014	(3.9981, 4.0054)
	Vs1	1.9998	6.0000e-4	1.9998	1.9998	(1.9985, 2.0010)
	ρ1	2.2100	0.0101	2.2132	2.2148	(2.1877, 2.2226)
Type-2	Vp2	3.8076	0.0050	3.8074	3.8069	(3.7979, 3.8163)
	Vs2	1.8800	0.0013	1.8801	1.8801	(1.8778, 1.8824)
	ρ2	2.5649	0.0118	2.5657	2.5676	(2.5416, 2.5848)

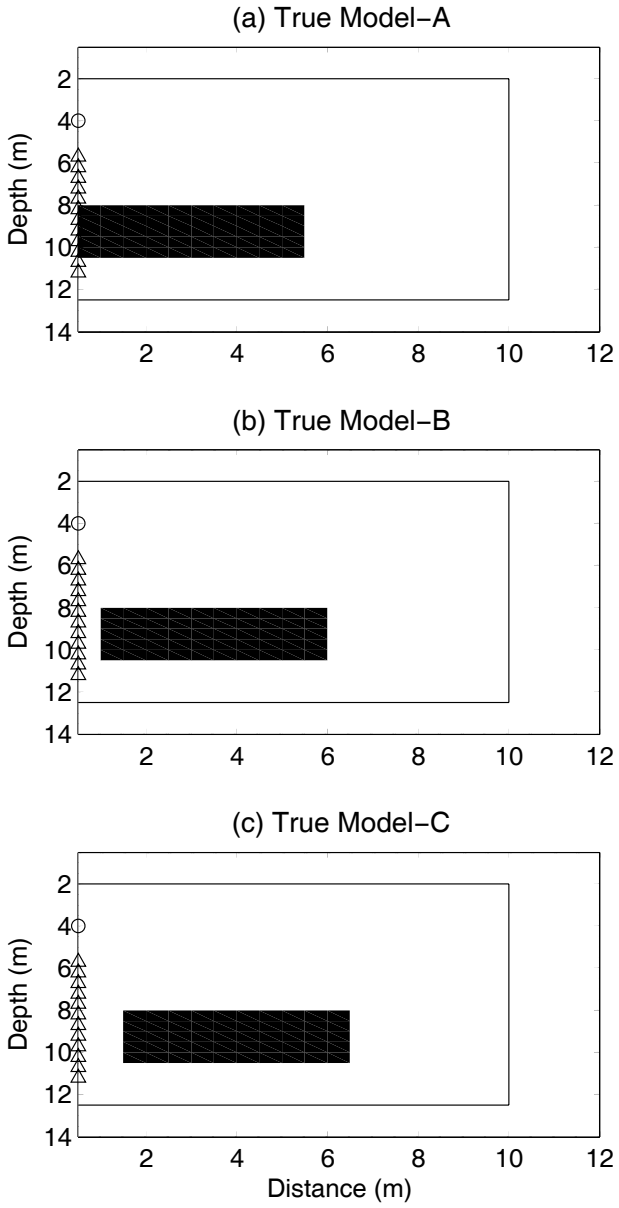

Figure 8.1: Synthetic models

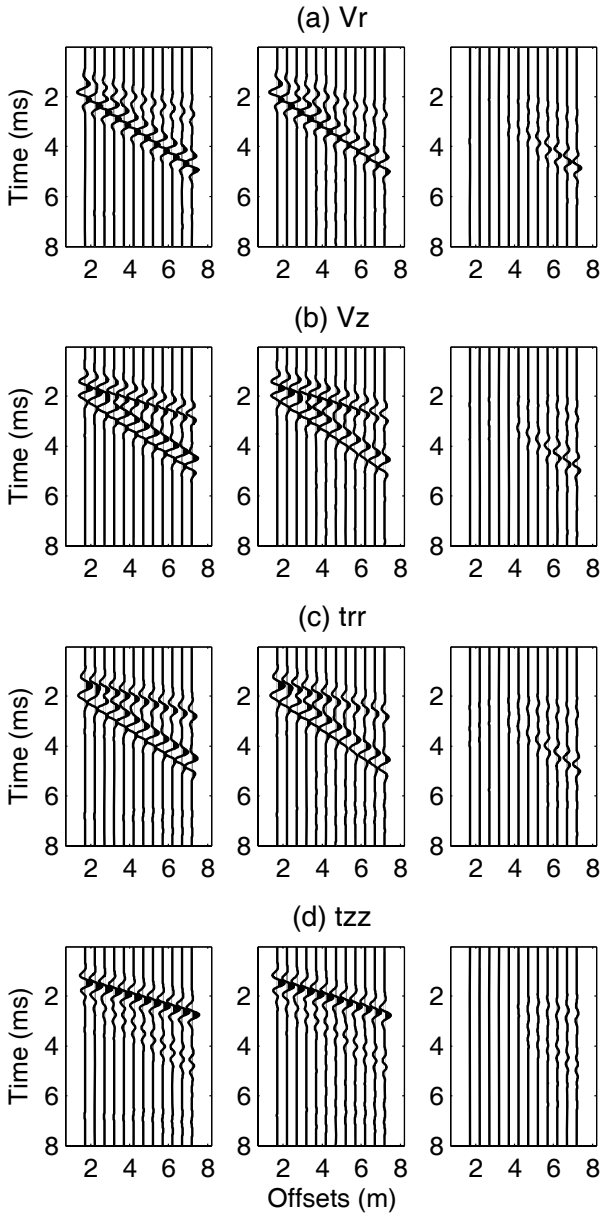

Figure 8.2: Model-A versus homogenous case.

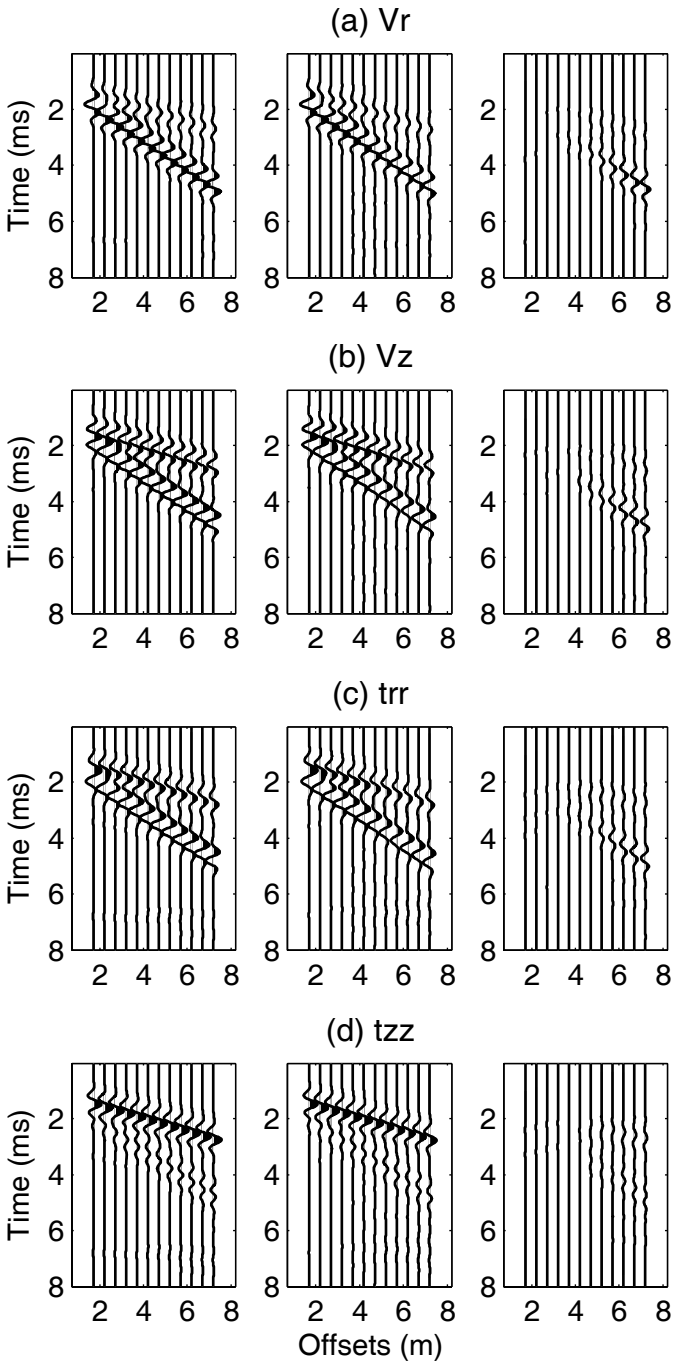

Figure 8.3: Model-B versus homogenous case

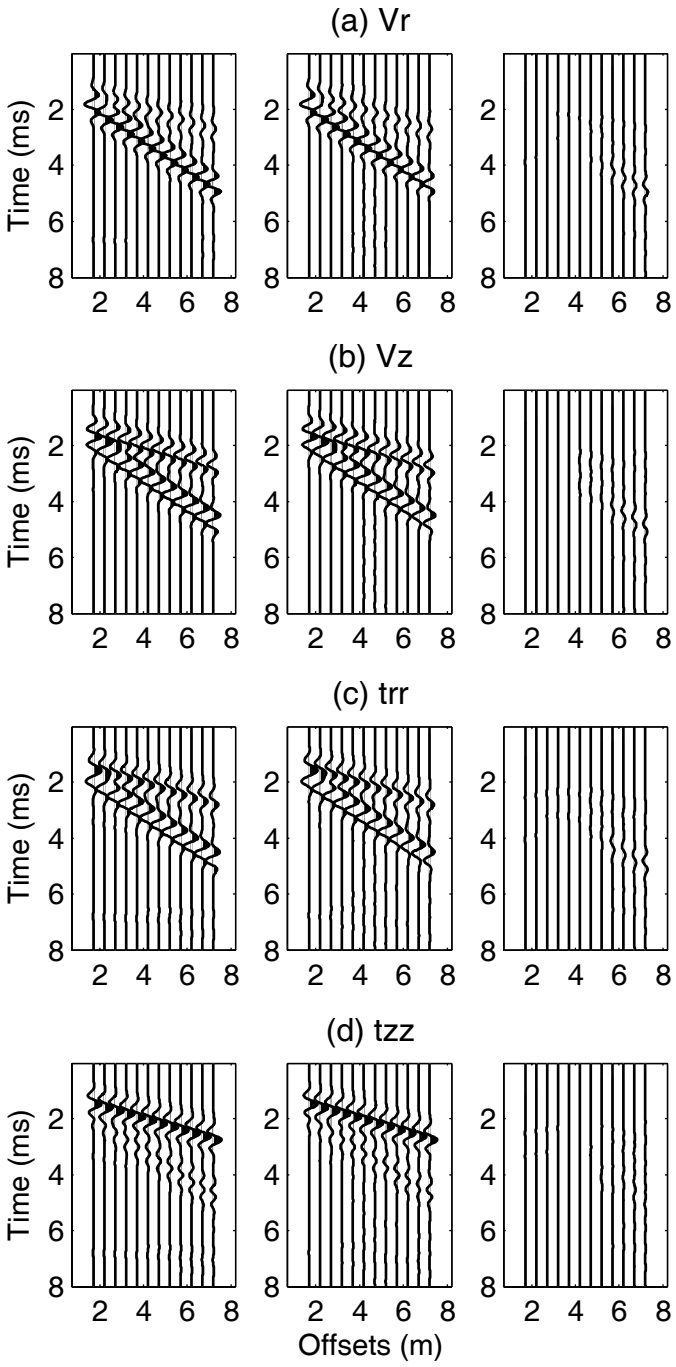

Figure 8.4: Model-C versus homogeneous case

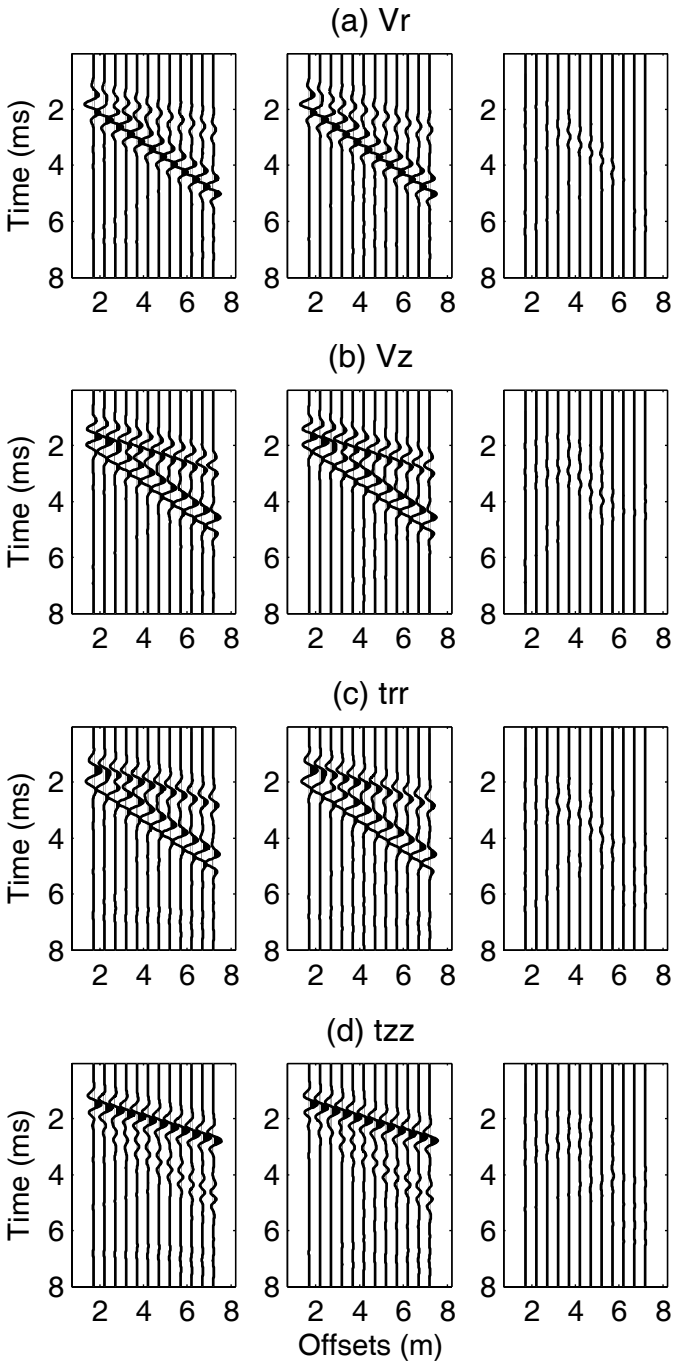

Figure 8.5: Shift up

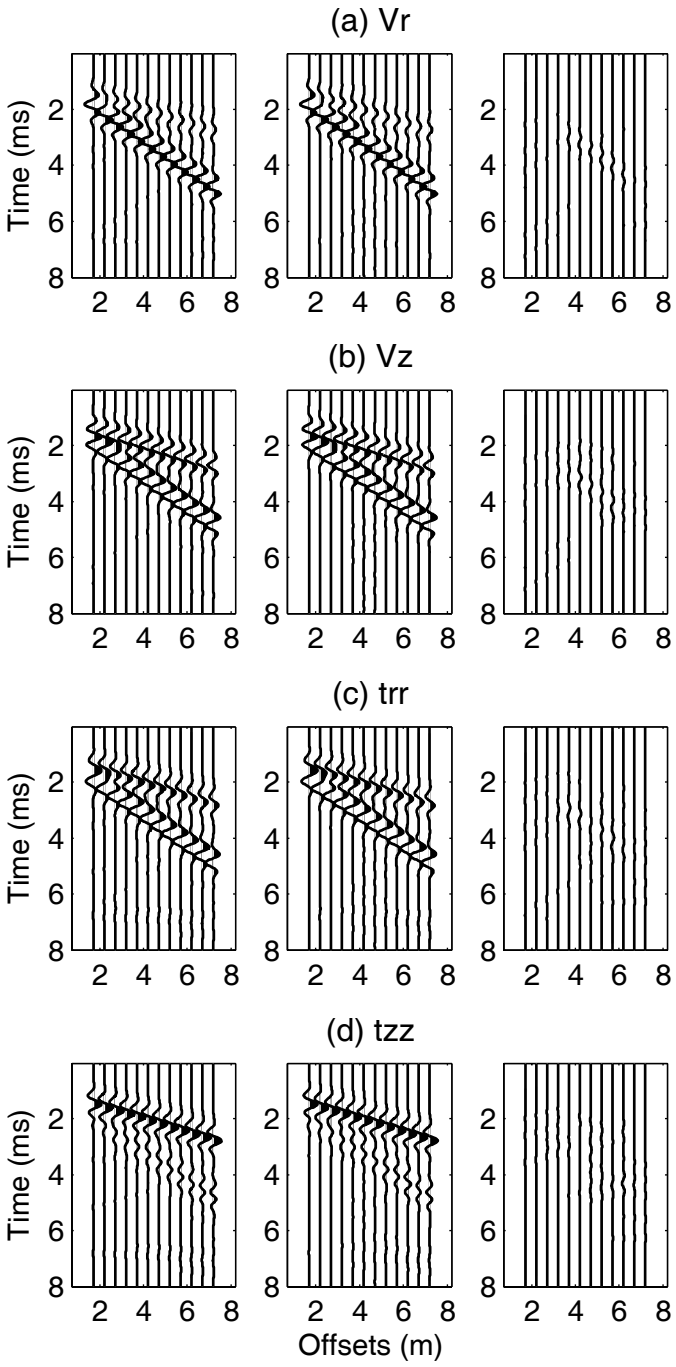

Figure 8.6: Shift down

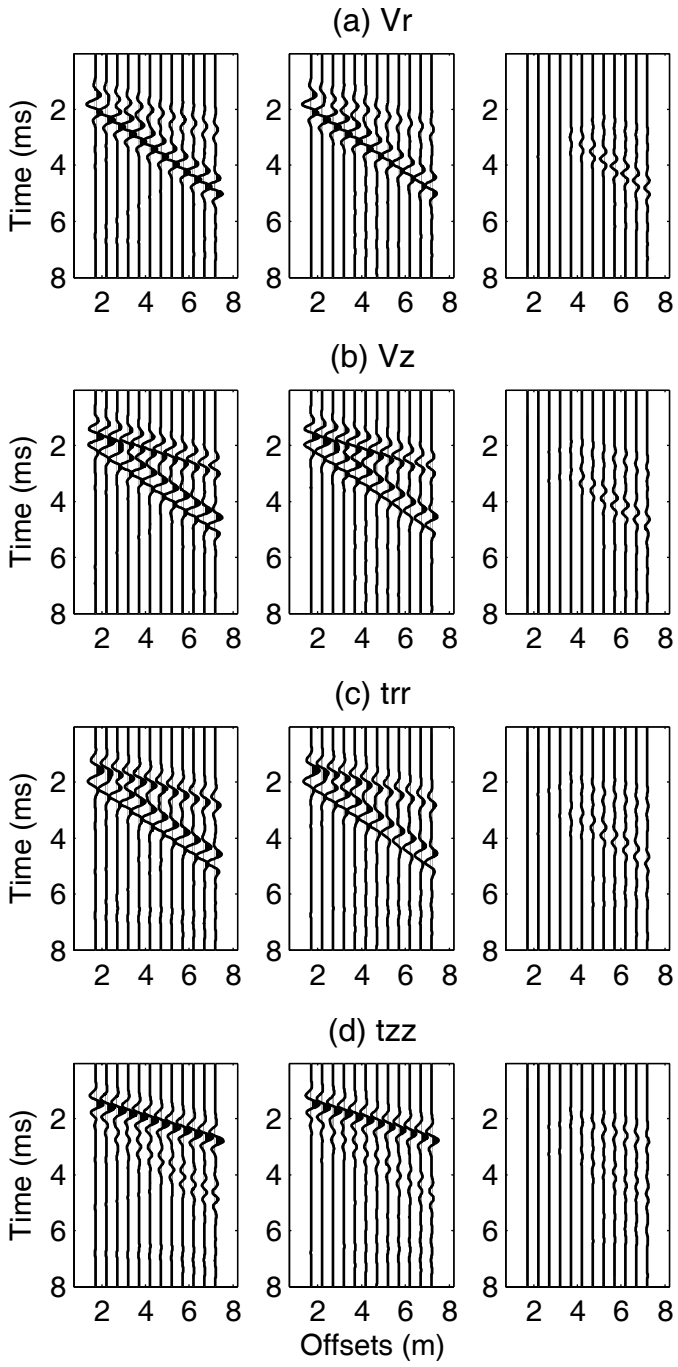

Figure 8.7: Shift right

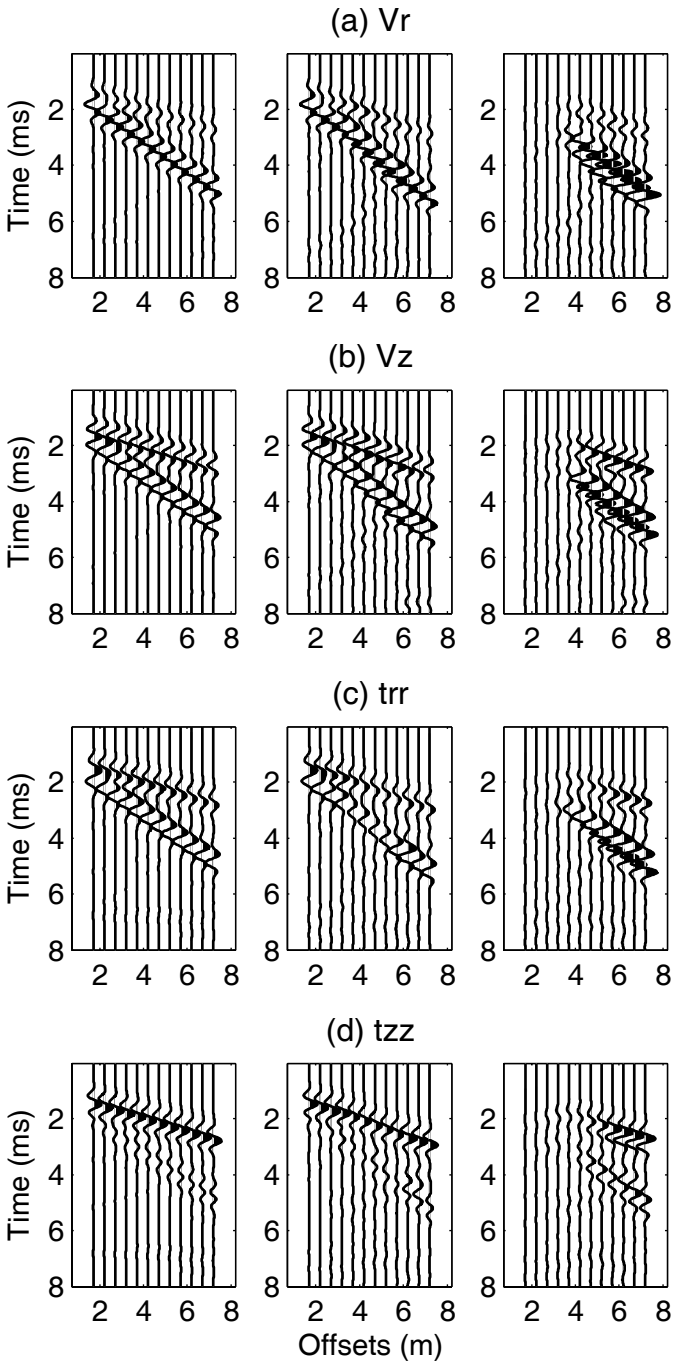

Figure 8.8: Decrease parameter values by 20%

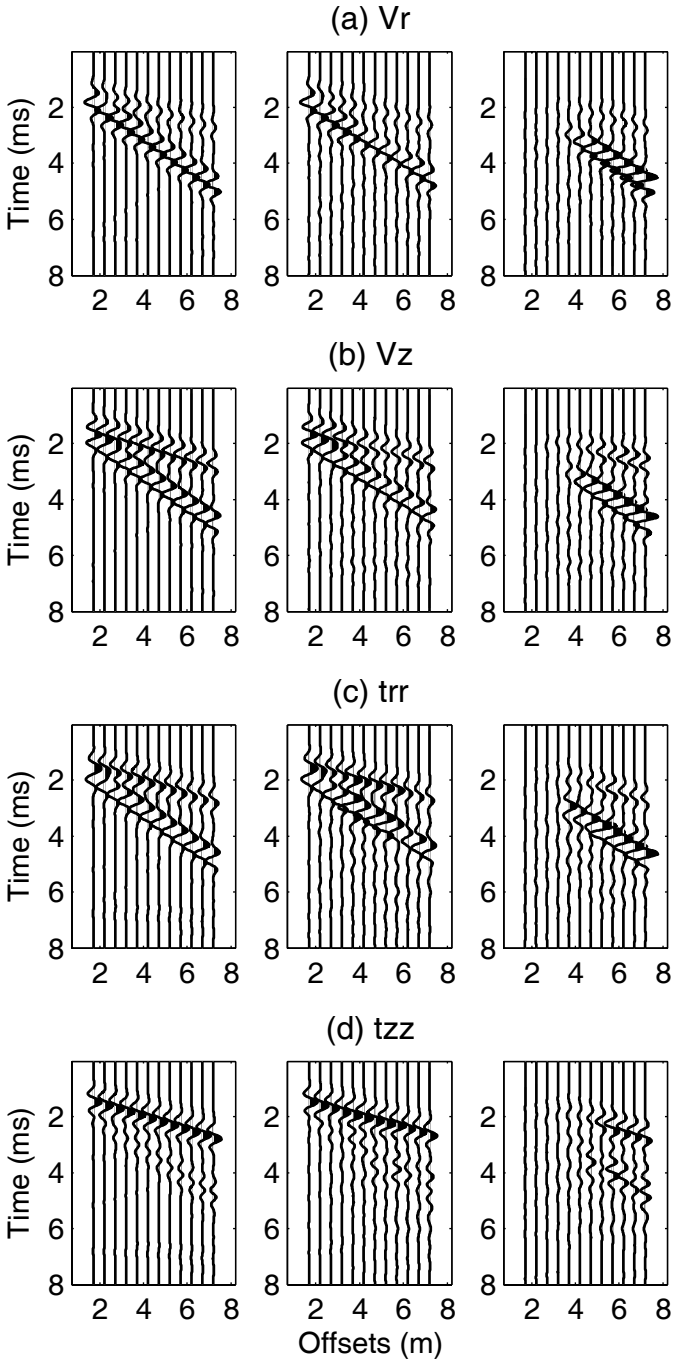

Figure 8.9: Increase parameter values by 20%

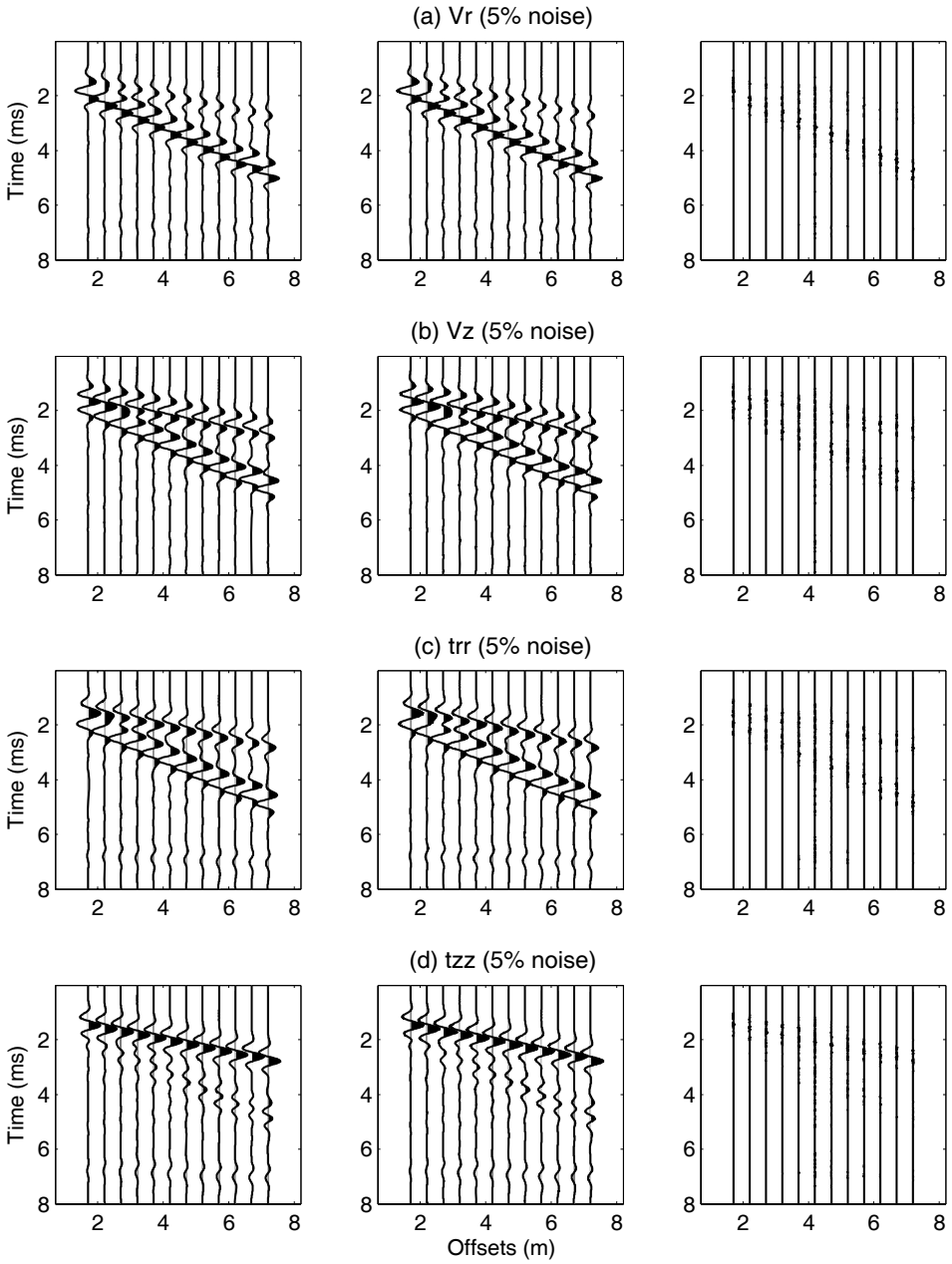

Figure 8.10: Synthetic waveform data with 5% relative random noise.

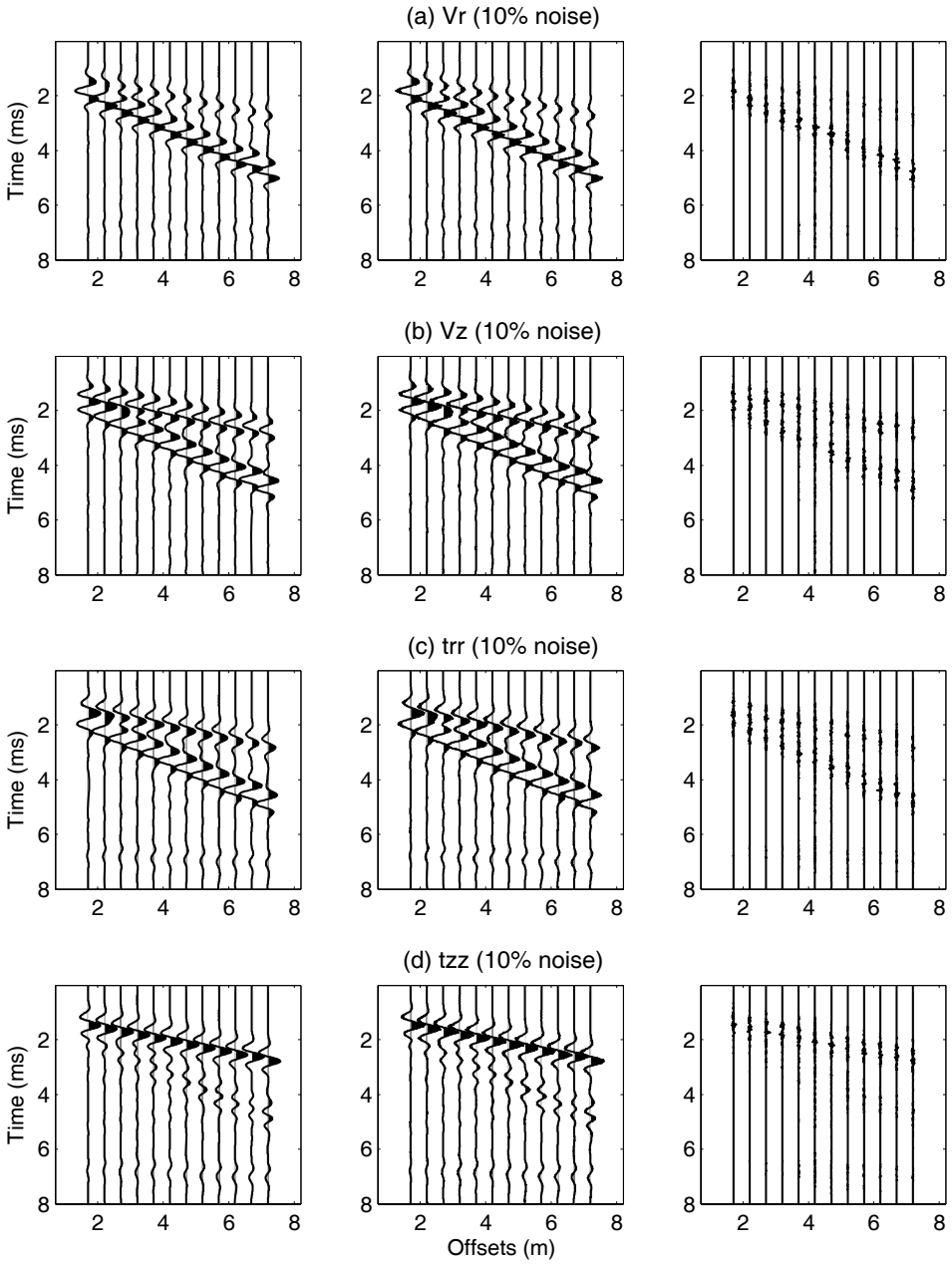

Figure 8.11: Synthetic waveform data with 10% relative random noise

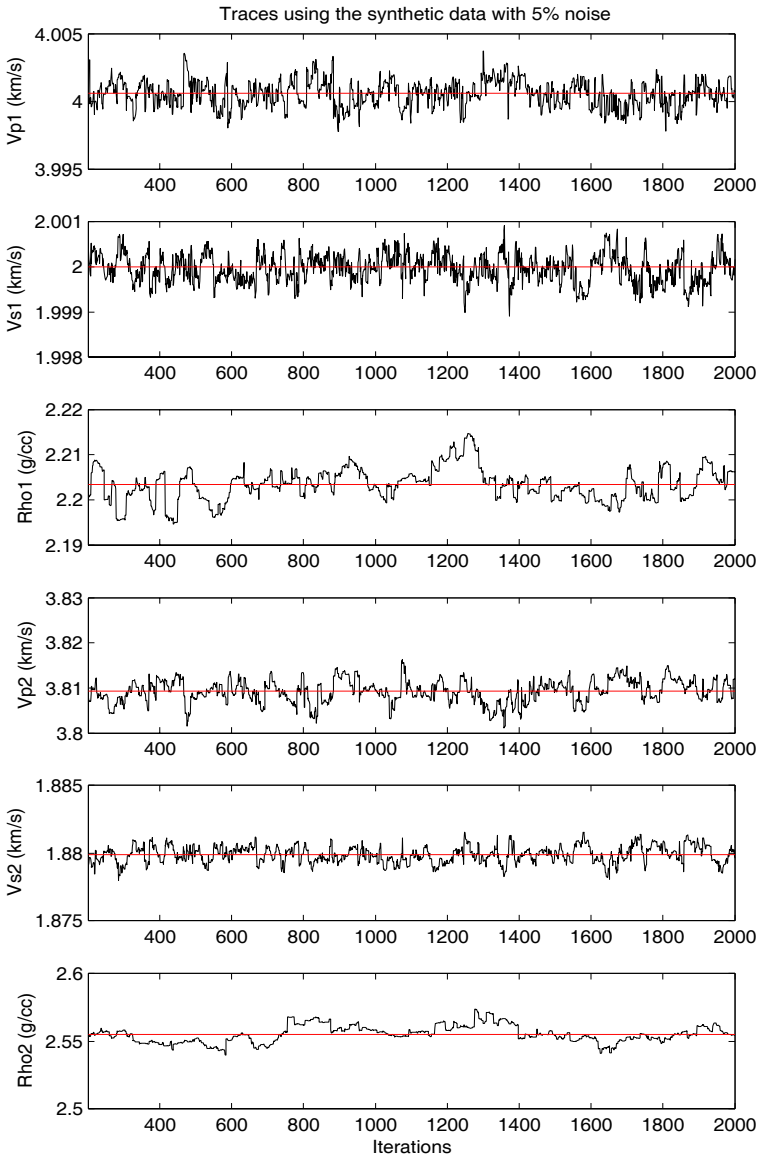

Figure 8.12: Traces of Markov chains using the synthetic data with 5% relative random noise.

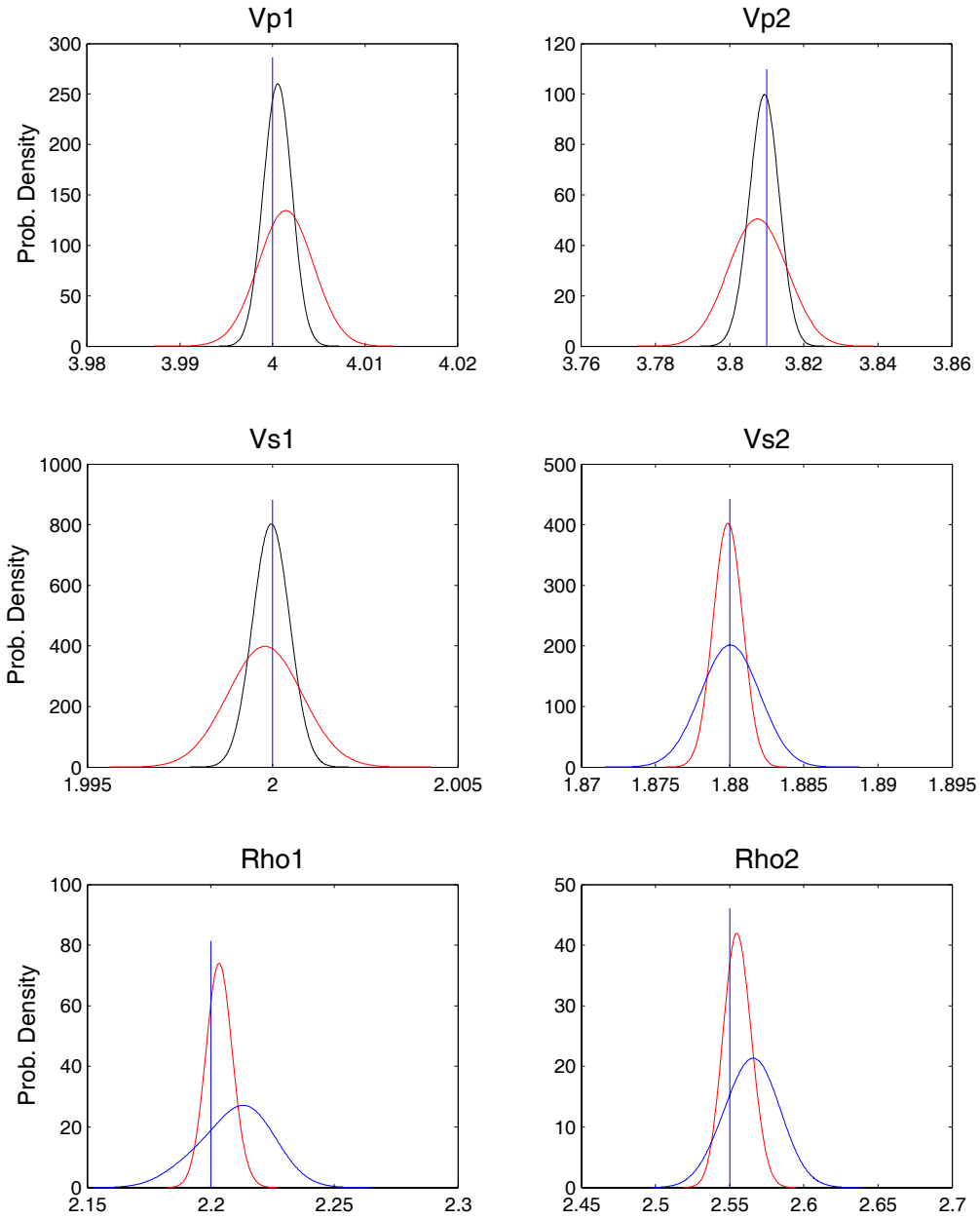

Figure 8.13: Estimated marginal posterior probability density functions or rock-physics parameters.

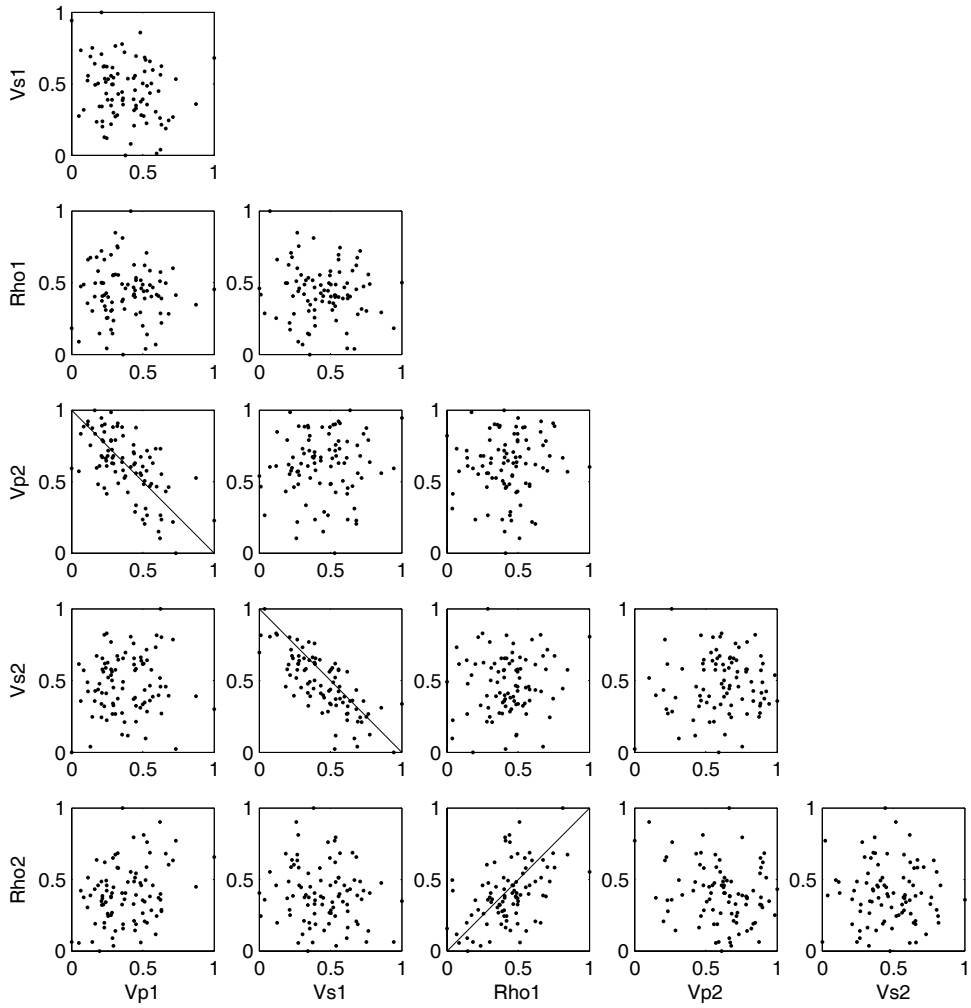

Figure 8.14: Estimated pairwise posterior correlation among rock-physics parameters when using the synthetic data with 5% relative random noise.

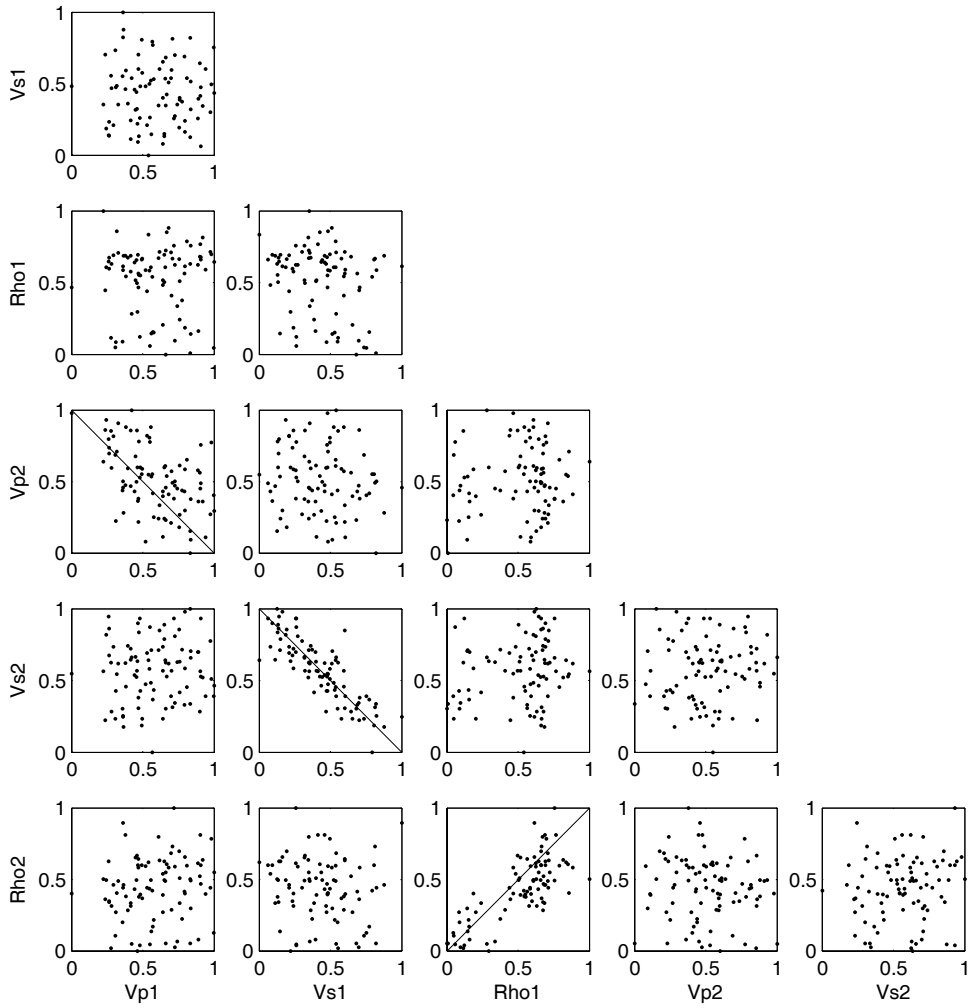

Figure 8.15: Estimated pairwise posterior correlation among rock-physics parameters when using the synthetic data with 10% relative random noise.

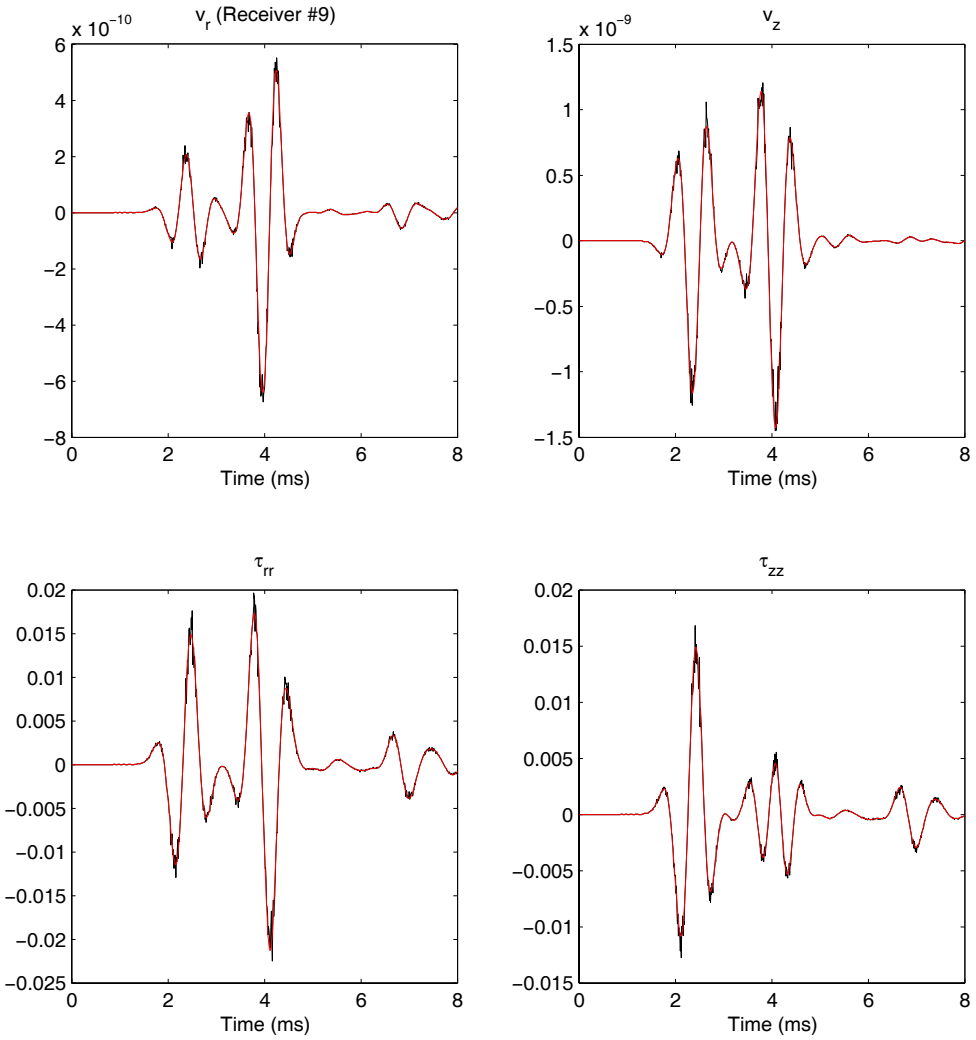

Figure 8.16: Misfits of waveforms collected at the tenth receiver using the synthetic data with 10% relative random noise.

CHAPTER 9

EXPERIMENTAL METHODS

There are no experimental components of the project to be included in this final report. Components of the project focus exclusively on the development of numerical algorithms and computer software for both forward modeling and inversion. In addition, the project includes analysis and interpretation of field and synthetic measurements. All of these developments are described in the Results and Discussions section of the report.

CHAPTER 10

CONCLUSION

Work performed during the three-year period of this project was focused to the development, testing, and appraisal of several methods for the estimation of elastic and petrophysical properties jointly from borehole sonic and EM measurements.

Interpretation of sonic and electromagnetic measurements is invariably performed separately even though the two sets of measurements usually probe the same volume of rock. The overall objective of the project was to demonstrate the compatibility of sonic and electromagnetic measurements for the joint estimation of in-situ elastic and petrophysical properties. We conclusively showed that estimation of elastic and petrophysical rock properties jointly from borehole sonic and electromagnetic measurements improves the resolution of the estimated properties and reduces their non-uniqueness (uncertainty) compared to estimations performed separately from the two sets of measurements. Moreover, we showed that the effective combination of the two sets of measurements permits the accurate and reliable estimation of porosity, fluid saturation, and hydraulic permeability of the probed rock formations. The recommended measurement and interpretation practice in boreholes is to include the physics of mud-filtrate invasion as the driving mechanism to assess dynamic space-time variations of fluid saturation. This approach enables the in-situ estimation of both hydraulic permeability and dry-rock elastic moduli of rock formations jointly from sonic and electromagnetic measurements.

Development of the joint inversion algorithms central to this project required an initial, preliminary phase of work to develop fast and efficient numerical algorithms for the numerical simulation of time-domain borehole sonic measurements. Accordingly, forward algorithms were developed and successfully tested for the specific cases of 1D, 2D, and 3D elastic media. The latter algorithms were combined with existing software for the simulation of borehole EM measurements to perform joint inversion of the two sets of measurements. Joint inversion algorithms and codes were developed based on deterministic and stochastic procedures.

Synthetic and field examples of application confirmed that the joint inversion of sonic and EM borehole measurements reduces non-uniqueness in the estimation of elastic and petrophysical properties, thereby improving the accuracy and reliability of the estimated

properties. By contrast, the estimation of the same properties separately from sonic and EM borehole measurements yields reliable and stable estimates of properties only when the estimation is sufficiently constrained by a-priori information. In either case, separate or joint inversion of borehole sonic and EM measurements, the success of the estimation depends on the availability of measurement sensitivity to perturbations of the unknown properties. Thus, it is recommended that the joint inversion be pursued only in those cases where perturbations of elastic and petrophysical properties are measurable within existing noise limitations of borehole acquisition systems. The most difficult cases of application are those of rocks with very low porosity, where variations of bulk elastic and electrical properties due to variations of fluid saturation are marginal, hence difficult to measure accurately.

It was also found that the joint inversion of borehole sonic and EM measurements could be performed by honoring the process of mud-filtrate invasion. Such a process is undergone by porous and permeable formations penetrated by an overbalanced well. Presence of invasion causes the fluid saturation to vary spatially in the vicinity of the wellbore: original saturating fluid (e.g. hydrocarbons) is radially displaced away from the wellbore by mud filtrate. Borehole EM measurements can take advantage of these near-wellbore fluid saturation variations as they are designed to exhibit selective sensitivity to the radial zone of response. Thus, use of EM borehole measurements in combination with sonic measurements is ideal as the former can resolve the spatial variations of fluid saturation and the latter can quantify the corresponding effects on elastic properties. At the same time, the simulation of the process of mud-filtration enables the estimation of permeability when this property has a leading effect on the spatial distribution of fluid saturation. We successfully tested the latter estimation procedure on synthetic and field data sets. In addition to yielding estimates of permeability, we obtained estimates of dry-rock moduli that were consistent with rock-core measurements. It was found that the simulation of the process of mud-filtrate invasion is the best way to simultaneously honor borehole EM and sonic measurements. The same approach enables a direct physical link between petrophysical properties and bulk values of electrical conductivity and elastic properties.

Optimal integration of borehole EM and sonic measurements to estimate elastic and petrophysical properties requires that both sets of measurements be designed to exhibit selective "deepening" of the zone of response into the probed rock formations. We strongly recommend that such types of measurement acquisition systems be developed for the reliable estimation of

rock properties. Additional feasibility studies should include the case of EM and sonic measurements acquired in highly-deviated wells with special consideration to electrical and elastic anisotropic conditions. Presence of in-situ non-hydrostatic stress (including borehole-induced stress) undergone by rock formations should be considered to quantify its influence on borehole sonic measurements relative to that of fluid-saturation variations near the wellbore.

CHAPTER 11

REFERENCES

CHAPTER 3

[1] Tubman, K. M., Cheng, C. H., and Toksöz, M. N., "Synthetic full waveform acoustic logs in cased boreholes", Geophysics, 49, 1051-1059., 1984.

[2] Chen, X., Quan, Y., and Harris, J. M., "Seismogram synthesis for radially layered media using the generalized reflection/ transmission coefficients method: Theory and applications to acoustic logging", Geophysics, 61, 1150-1159, 1996.

[3] Chi Sh. H. and Torres-Verdin C., "Synthesis of multipole acoustic logging measurements using the generalized reflection/transmission matrices method", SEG Technical Program Expanded Abstracts 23, 350-353, 2004.

[4] Wu X. Y. and Harris J. M., "Seismic Wave Modeling in Poroelastic Media Using the Generalized Reflection/Transmission(R/T) Coefficients Method", SEG Expanded Abstracts 17, 1799-1802, 1998.

[5] Biot, M. A., "Mechanics of Deformation and Acoustic Propagation in Porous media", J. Appl. Phys., 33, 1482-1498, 1962a.

[6] Gregory, A. R., "Aspects of rock physics from laboratory and log data that are important to seismic interpretations", AAPG Memoir, 26, 15-46, 1977.

[7] Biot, M. A., "Theory of Propagation of Elastic Waves in a Fluid-Saturated Porous Solid. II Higher Frequency Range", J. acoustic Soc. Am, 28, 179-190, 1956b.

[8] Auriault, J. L., Borne L and Chambon R., "Dynamics of porous saturated media, checking the generalized law of Darcy", J. Acoust. Soc. Am, 77, 1641-1650, 1985.

[9] Hu H. Sh. and Wang K. X., "Dynamic permeability in poroelastic medium acoustics", Acta Geophysics Sinica (in Chinese), 44, 135-141, 2001.

[10] Schmitt, D. P., "Effects of radial layering when logging in saturated porous formations", J. Acoustic Soc. Am, 84, 2200-2214, 1988.

CHAPTER 4

[1]. Biot, M.A., "Theory of Deformation of a Porous Viscoelastic Anisotropic Solid", J. Appl. Phys., 27, 459-467, 1956.

[2]. Biot, M.A., "Generalized Theory of Acoustic Propagation in Porous Dissipative Media", J. Acoust. Soc. Am, 34, 1254-1264, 1962a.

[3]. Biot, M.A., "Mechanics of Deformation and Acoustic propagation in Porous Media", J. Appl. Phys., 33, 1482-1498, 1962b.

[4]. Carcione, J.M., "Wave propagation in anisotropic, saturated porous media: plane-wave theory and numerical simulation", J. Acoust. Soc. Am, 99, 2655-2666, 1996.

[5]. Kurkjian, A.L. and Chang, S.K., "Acoustic multipole sources in fluid-filled borehole", Geophysics, 51, 148-163, 1986.

[6]. Kurkjian, A.L., "Numerical computation of individual far-field arrivals excited by an acoustic source in a borehole", Geophysics, 50, 852-866, 1985.

[7]. Mittet R. and Renlie L., "High-order, finite-difference modeling of multipole logging in formations with anisotropic attenuation and elasticity", Geophysics, 61, 21-33, 1996.
[8]. Randall, C. J., Scheibner, D. J., and Wu, P. T., "Multipole borehole acoustic waveforms: Synthetic logs with beds and borehole washouts", Geophysics, 56, 1757–1769, 1991.
[9]. Payton, R. G., "Elastic wave propagation in transversely isotropic media", Martinus Nijhoff Publ., 1983.
[10]. Schmitt, P.D., Zhu, Y., and Cheng, C.H., "Shear wave logging in semi-infinite saturated porous formations", J. Acoust. Soc. Am., 84, 2230-2244, 1996.
[11]. Schmitt, P.D., "Acoustic multipole logging in transversely isotropic poroelastic formations", J. Acoust. Soc. Am., 86, 2397-2421, 1989.
[12]. Takeuchi, H. and Saito, M., "Seismic surface waves" In B.A. Bolt (editor), Method of computational physics, V.11: New York, Academic Press, 217-295, 1972.
[13]. Thomsen, L., "Weak elastic anisotropy", Geophysics, 51, 1954–1966, 1986.
[14]. Virieux, J., "P-SV wave propagation in heterogeneous media: Velocity-stress finite-difference method", Geophysics, 51, 889–901, 1986.
[15]. Xu, Y., Xia J., and Miller, R., "Finite-difference modeling of high-frequency Rayleigh-wave propagation for near-surface applications", submit to Geophysics (under review), 2005.
[16]. Zhang, J., "Quadrangle-grid velocity-stress finite difference method for poroelastic wave equations", Geophys.J.Int., 139, 171-182, 1999.

CHAPTER 5

[1] Asvadurov, S. et al., "Application of the difference Gaussian rules to solution of hyperbolic problems", J. Computat. Phys., 158, 116-135, 2000.
[2] Chen, N. et al., "Borehole wave propagation in three dimensions", J. Acoust. Soc. Am., 103 (2), 702-712, 1995.
[3] Chen, Y. H. et al., "A three-dimensional finite-difference code for the modeling of sonic logging tools", J. Acoust. Soc. Am., 103 (2), 702-712, 1998.
[4] Chew, W. C. et al., "Perfectly matched layers for elastodynamics: A new absorbing boundary condition", J. Computat. Acoustics, 4 (4), 341-359, 1996.
[5] Kurkjian, A. L. et al., "Acoustic multipole sources in fluid-filled boreholes", Geophysics, 51 (1), 148-163, 1986.
[6]]Leslie, H. D. et al., "Multipole sources in boreholes penetrating anisotropic formations: Numerical and experimental results", J. Acoust. Soc. Am., 91 (1), 12-27, 1992.
[7] Liao, Z. P. et al., "A transmitting boundary for transient wave analyses", Scientia Sinica (series A), 27, 1063-1076, 1984.
[8] Liu, Q. H. et al., "A three-dimensional finite difference simulation of sonic logging", J. Acoust. Soc. Am., 100 (1), 72-79, 1996.
[9] Randall, C. J et al., "Multipole acoustic waveforms in nonaxisymmetric borehole and formations" J. Acoust. Soc. Am., 90(3), 1620-1631, 1991.
[10] Schmitt, D. P., "Shear wave logging in elastic formations", J. Acoust. Soc. Am., 84 (6), 2215-2229, 1988.
[11] Stephen, R. A. et al., "Finite-difference synthetic acoustic logs", Geophysics, 50 (10), 1588-1609, 1985.
[12] Wang, T. et al., "Finite-difference modeling of elastic wave propagation, A nonsplitting

perfectly matched layer approach", Geophysics, 68(5), 1749-1755, 2003.
[13] Yoon, K. H. et al., "3-D finite-difference modeling of elastic waves in borehole environments", Geophysics, 57 (6), 793-804, 1992.

CHAPTER 6

[1] Chen, X., Y. Quan, and J. M. Harris, "Seismogram synthesis for radially layered media using the generalized reflection/transmission coefficients method: theory and applications to acoustic logging", Geophysics, 61, 1150-1159, 1996.
[2] Chew, W. C., S. Barone, B. Anderson, and C. Hennessy, "Diffraction of axisymmetric waves in a borehole by bed boundary discontinuities", Geophysics, 49, 1586-1595, 1984.
[3] Chew, W. C., and Liu Q. H., "Inversion of induction tool measurements using the distorted Born iterative method and CG-FFHT", IEEE Trans. Geosci. Remote Sensing, 32, 878–884, 1994.
[4] Chi, S., C. Torres-Verdín, J. Wu, and F. O. Alpak, "Assessment of mud-filtrate invasion effects on borehole acoustic logs and radial profiling of formation elastic properties", Society of Petroleum Engineers Annual Technical Conference and Exhibition**,** Extended Abstracts, Paper SPE 90159, 2004.
[5] Chi, S., and C. Torres-Verdín, "Synthesis of multipole acoustic logging measurements using the generalized reflection/transmission matrices method", Presented at the Society of Exploration Geophysicists 74th Annual International Meeting, Denver, CO, October 10-15, 2004.
[6] Habashy, T. M., and A. Abubakar, "A general framework for constraint minimization for the inversion of electromagnetic measurements", Progress in Electromagnetic Research, 46, 265-312, 2004.
[7] Hornby, B. E., "Tomographic reconstruction of near-borehole slowness using refracted borehole sonic arrivals", Geophysics, 58, 1726-1738, 1993.
[8] Kelly, C.T., "Iterative Methods for Optimization: Society for Industrial and Applied Mathematics", 1999.
[9] Mavko, G., T. Mukerji, and J. Dvorkin, "The Rock Physics Handbook, tools for seismic analysis in porous media", Cambridge University Press, 2003.
[10] Mora, P., "Nonlinear two-dimensional elastic inversion of multioffset seismic data", Geophysics, 52, 1211-1228, 1987.
[11] Sinha, B., B. Vissapragada, S. Kisra, S. Sunaga, H. Yamamoto, T. Endo, H. P. Valero, L. Renlie, and J. Bang, "Optimal well completions using radial profiling of formation shear slownesses", Society of Petroleum Engineers Annual Technical Conference and Exhibition, Extended Abstracts, Paper SPE 95837, 2005.
[12] Smith, T., M., C. H. Sondergeld, and C. S. Rai, "Gassmann fluid substitution, a tutorial", Geophysics, 68, 430-440, 2003.
[13] Tarantola, A. "Inversion of seismic reflection data in the acoustic approximation", Geophysics, 49, 1259-1266, 1984.
[14] Zhou, B., and S. A. Greenhalgh, "Crosshole seismic inversion with normalized full-waveform amplitude data", Geophysics, 68, 1320-1330, 2003.
[15] Zhang, G. J., G. L. Wang, and H. M. Wang, "Application of novel basis functions in a hybrid method simulation of the response of induction logging in axisymmetrical stratified media", Radio Science, 34, 19-26, 1999.

[16] Zhang, G. J, H. M. Wang, and G. L. Wang, "A. C. logging response in stratified media", Chinese Journal of Geophysics, 38, 583-593, 1995.

CHAPTER 7

[1] Hilterman, F. J., "Seismic Exploration Modeling Course Notes," Geophysical Development Corporation Houston, TX, 1984.
[2] Biot, M. A., "Theory of propagation of elastic waves in a fluid-saturated porous solid. 1. Low-frequency range," J. Acoust. Soc. Am., 28, 168-178, 1956.
[3] Gassmann, F., "Uber die elastizitat poroser medien," Verteljahrsschrift de Naturforschenden Gesellschaft in Zurich, 96, 1-23, 1951.
[4] Hamilton, E. L., "Elastic properties of marine sediments," Geophysics, 76, 579-604, 1971.
[5] Thomsen, L., "Biot-consistent elastic moduli of porous rocks: low frequency limit," Geophysics, 50, 2797-2807, 1985.
[6] Zhu, X., and Mcmechan, G. A., "Direct estimation of the bulk modulus of the frame in a fluid-saturated elastic medium by Biot Theory," 60th Ann. Internat. Mtg., SEG Expanded Abstracts, 9, 787, 1990.
[7] Wang, Z., "The Gassmann equation revisited: comparing laboratory data with Gassmann's predictions," SEG, 3, 8-23, 2000.
[8] Han, D., and Batzle, M. L., "Gassmann's equation and fluid-saturation effects on seismic velocities," Geophysics, 69, 398-405, 2004.
[9] Dvorkin, J., Mavko, G., and Gurevich, B., "Fluid substitution in shaley sediment using effective porosity," Geophysics, 72, 1-8, 2007.
[10] Engelmark, F., "Error propagation in Gassmann modeling for 4D feasibility studies," The Leading Edge, 21, 984-987, 2002.
[11] Wood, A. W., "A Textbook of Sound," The MacMillan Co., New York, 360-375, 1955.
[12] White, J. E., "Underground Sound: Application of Seismic Waves," Elsevier Science Publ. Co., Inc., New York, 1983.
[13] Wu, J., Torres-Verdín, C., Sepehrnoori, K., and Proett, M., "The influence of water-base mud properties and petrophysical parameters on mudcake growth, filtrate invasion, and formation pressure," Petrophysics, 46, 14-32, 2005.
[14] Archie, G. E., "The electrical resistivity log as an aid in determining some reservoir characteristics," Trans. Am. Inst. Mech. Eng., 146, 54-62, 1942.
[15] Salazar, J. M., Torres-Verdín C., and Sigal, R., "Assessment of permeability from well-logs based on core calibration and simulation of mud-filtrate invasion," Petrophysics 46, 434-451, 2005.
[16] Malik, M., Salazar, J.M., Torres-Verdín, C., Wang, L.M., Lee, J.H., and Sepehrnoori, K., "Influence of petrophysical and fluid properties on array-induction measurements acquired in the presence of oil-base mud-filtrate invasion," paper presented at the 2007 SPWLA Annual Logging Symposium, Austin, June 3-6, 2007.
[17] Waxman, M. H. and Smits, L. J. M.: "Electrical conductivities in oil-bearing shaly sands," Soc. Pet. Eng. J., 8, 107-122, 1968.
[18] Wyman, R.E., "The Interrelationships of Petrophysics, Geology and Geophysics," AAPG continuing education-Stratigraphic Interpretation of Seismic Data, Dec. 1982.

[19] Chi, S., Torres-Verdín, C., Wu, J., and Alpak, F.O., "Assessment of mud-filtrate invasion effects on borehole acoustic logs and radial profiling of formation elastic parameters," SPE Reservoir Eval. & Engr., 9, 553-564, 2006.
[20] Hill, R., "The elastic behavior of crystalline aggregate," Proc. Physical Soc., London A65, 349-354, 1952.
[21] Finley, R. J., "Geology and engineering characteristics of selected low-permeability sandstones: A national survey," University of Texas at Austin, Bureau of Economic Geology, Report of Investigation no. 138, 59, 1984.
[22] McGowen, M. K., and Harris, D. W., "Cotton Valley (upper cretaceous) and Hosston (lower cretaceous) depositional systems and their influence on salt tectonics in the East Texas Basin," University of Texas at Austin, Bureau of Economic Geology, Geological Circular, 84-5, 41, 1984.
[23] Salazar, J. M., Torres-Verdín, C., Alpak, O. F., Habashy, M. T., and Klein, D. J., "Estimation of permeability from borehole array induction measurements: application to the petrophysical appraisal of tight gas sands," Petrophysics, 47, 527-544, 2006.

CHAPTER 8

[1] Besag, J., 2001, Markov chain Monte Carlo for statistical inference: Center for Statistics and the Social Sciences, University of Washington, No. 9, 1-67.
[2] Biot, M. A., 1952, Propagation of elastic waves in a cylindrical bore containing a fluid, J. Appl. Phys., 23, 997-1005.
[3] Bosch, M., 1999, Lithologic tomography: from plural geophysical data to lithology estimation: Journal of Geophysical Research, 104, 749-766.
[4] Buland, A., and H. Omre, 2003, Bayesian wavelet estimation from seismic and well data, Geophysics, 68, 2000-2009.
[5] Cerjan, C., D. Kosloff, R. Kosloff, and M. Reshef, 1985, A nonreflecting boundary condition for discrete acoustic and elastic equations, Geophysics, 50, 705-708.
[6] Chen, J., M. Hoversten, D. Vasco, Y. Rubin and Z. Hou, 2007, A Bayesian model for gas saturation estimation using marine seismic AVA and CSEM data, Geophysics, 72, WA85-WA95.
[7] Chen, Y. H., C. C. Weng, and Q. H. Liu, 1998, A three-dimensional finite difference code for the modeling of sonic logging tools, J. Acoust. Soc. Am., 103, 702-712.
[8] Cheng, C. H., and M. N. Toksoz, 1981, Elastic wave propagation in a fluid-filled borehole and synthetic acoustic logs, Geophysics, 46, 1042-1053.
[9] Gelman, A., and D. B. Rubin, 1992, Inference from iterative simulation using multiple sequences, Statistical Science, 7, 457--472.
[10] Geweke, J., 1992, Evaluating the accuracy of sampling-based approaches to the calculation of posterior moments, in Bayesian Statistics 4, edited by J. M. Bernardo, J. O. Berger, A. P. David, and F. M. Smith, pp. 169--193, Oxford University Press.
[11] Gilks, W., S. Richardson, and D. Spiegelhalter, 1996, Markov Chain Monte Carlo in Practice: Chapman & Hall/CRC, New York.
[12] Graves, R. W., 1996, Simulating seismic wave propagation in 3D elastic media using staggered-grid finite differences, Bulletin of the Seismic Society of America (BSSA), 86, 1091-1106.

[13] Hastings, W. K., 1970, Monte Carlo sampling methods using Markov chains and their applications, Biometrika, 57, 97-109.

[14] Hoversten, G., F. Cassassuce, E. Gasperikova, G. Newman, J. Chen,, D. Vasco, Y. Rubin, and Z. Hou,, 2006, Direct reservoir parameter estimation using joint inversion of marine seismic AVA and CSEM data: Geophysics, 71, C1-C13.

[15] Levander, A. R., 1988, Fourth-order finite-difference P-SV seismograms, Geophysics, 53, 1425-1436.

[16] Liu, Q. H., and C. Chang, 1994, Compressional head waves in attenuative formations, Proc. 64th Annual Meeting of SEG, 12-15.

[17] Maliverno, A., 2002, Parsimonious Bayesian Markov chain Monte Carlo inversion in a nonlinear geophysical problem: Geophysical Journal International, 151, 675-688.

[18] Mavko, G., T. Mukerji, and J. Dvorkin, 1998, The rock physics handbook: Tools for seismic analysis in porous media, Cambridge University Press, New York, USA.

[19] Metropolis, N., A. W. Rosenbluth, M.N. Rosenbluth, A. H. Teller, and E. Teller, 1953, Equations of state calculations by fast computing machines, Journal of Chemical Physics, 21, 1087-1092.

[20] Neal, R. M., 2003, Slice sampling: The Annuals Statistics, 31, 705-767.

[21] Raftery, A. E., and S. Lewis, How many iterations in the Gibbs sampler?, in Bayesian Statistics 4, edited by J. M. Bernardo, J. O. Berger, A. P. David, and F. M. Smith, pp. 763--773, Oxford University Press.

[22] Swenden, R. H. and J. S. Wang, 1987, Non-universal critical dynamics in Monte Carlo simulation, Phys. Rev. Letters, 58, 86.

[23] Tsang, L. and Radar, D., 1979, Numerical evaluation of transient acoustic waveforms due to a point source in a fluid-filled borehole, Geophysics, 44, 1706-1720.

[24] Virieux, J., 1986, P-SV wave propagation in heterogeneous media: velocity-stress finite-difference method, Geophysics, 51, 889-901.

National Energy Technology Laboratory

626 Cochrans Mill Road
P.O. Box 10940
Pittsburgh, PA 15236-0940

3610 Collins Ferry Road
P.O. Box 880
Morgantown, WV 26507-0880

One West Third Street, Suite 1400
Tulsa, OK 74103-3519

1450 Queen Avenue SW
Albany, OR 97321-2198

539 Duckering Bldg./UAF Campus
P.O. Box 750172
Fairbanks, AK 99775-0172

Visit the NETL website at:
www.netl.doe.gov

Customer Service:
1-800-553-7681